AN EXPERIMENTAL INVESTIGATION OF THE FLOW AROUND IMPULSIVELY STARTED CYLINDERS

A Thesis Submitted to the College of Graduate Studies and Research

in Partial Fulfillment of the Requirements for the Degree of Master of Science

in the Department of Mechanical Engineering,

University of Saskatchewan,

Saskatoon,

Saskatchewan,

Canada.

By

Nelson Tonui

PERMISSION TO USE

The author grants permission to the Libraries of the University of Saskatchewan to make this thesis available for inspection. Permission for copying of this thesis in any manner, in whole or in part, for scholarly purposes should be granted by my supervisor, Prof. D. Sumner, the Head of the Department of Mechanical Engineering, or the Dean of the College of Graduate Studies and Research. It is understood that any copying or publication or use of this thesis or parts thereof for financial gain shall not be allowed without my written permission. It is also understood that due recognition shall be given to me and to the University of Saskatchewan in any scholarly use which may be made of any material in my thesis.

Requests for permission to copy or to make other use of material in this thesis, in whole or part, should be addressed to:

Head of the Department Mechanical Engineering,

University of Saskatchewan,

57 Campus Drive,

Saskatoon, Saskatchewan, S7N 5A9

Canada.

ACKNOWLEDGMENTS

I would like to express my sincere gratitude to my supervisor, Prof. D. Sumner, for giving me this research opportunity. I am also grateful for his guidance and patience during my research. I would also like to thank my advisory committee, Prof. J.D. Bugg and Prof. K.A. Mazurek, for the positive criticisms that helped improve my research. The technical support of Mr. Dave Deustcher is highly appreciated; it would have been hard to accomplish this research without it.

My gratitude also goes to the staff of Engineering Shops for the assistance in the manufacture of models and facilities used. Particularly, the assistance of Mr. Henry Berg is acknowledged.

Finally, I would like to appreciate the support and encouragement from my wife and my parents throughout my Master's program.

DEDICATION

To my wife, Vivian.

Thanks for being patient when I was writing this thesis.

ABSTRACT

A study of impulsively started flow over cylindrical objects is made using the particle image velocimetry (PIV) technique for Reynolds numbers of Re = 200, 500 and 1000 in an X-Y towing tank. The cylindrical objects studied were a circular cylinder of diameter, D = 25.4 mm, and square and diamond cylinders each with side length, D = 25.4 mm. The aspect ratio, AR (= L/D) of the cylinders was 28 and therefore they were considered infinite. The development of the recirculation zone up to a dimensionless time of t^* = 4 following the start of the motion was examined. The impulsive start was approximated using a dimensionless acceleration parameter, a^*, and in this research, the experiments were conducted for five acceleration parameters, a^* = 0.5, 1, 3, 5 and 10. The study showed that conditions similar to impulsively started motion were attained once $a^* \geq 3$.

A recirculation zone was formed immediately after the start of motion as a result of flow separation at the surface of the cylinder. It contained a pair of primary eddies, which in the initial stages (like in this case) were symmetrical and rotating in opposite directions. The recirculation zone was quantified by looking at the length of the zone, L_R, the vortex development, both in terms of the streamwise location and the cross-stream spacing of the vortex centers, a and b, respectively, as well as the circulation (strength) of the primary vortices, Γ.

For all types of cylinders examined, the length of the recirculation zone, the streamwise location of the primary eddies and the circulation of the primary eddies increase as time advances from the start of the impulsive motion. They also increase with an increase

in the acceleration parameter, a^*, until $a^* = 3$, beyond which there is no more change, since the conditions similar to impulsively started conditions have been achieved. The cross-stream spacing of the primary vortices is relatively independent of Re, a^* and t^* but was different for different cylinders.

Irrespective of the type of cylinder, the growth of the recirculation zone at Re = 500 and 1000 is smaller than at Re = 200. The recirculation zone of a diamond cylinder is much larger than for both square and circular cylinders. The square and diamond cylinders have sharp edges which act as fixed separation points. Therefore, the cross-stream spacing of the primary vortex centers are independent of Re, unlike the circular cylinder which shows some slight variation with changes in Reynolds number.

The growth of the recirculation is more dependent on the distance moved following the start of the impulsive motion; that is why for all types of cylinders, the L_R/D, a/D and Γ/UD profiles collapse onto common curves when plotted against the distance moved from the start of the motion.

.

TABLE OF CONTENTS

PERMISSION TO USE i

ACKNOWLEDGMENTS ii

DEDICATION iii

ABSTRACT iv

TABLE OF CONTENTS vi

NOMENCLATURE ix

CHAPTER ONE: INTRODUCTION 1

1.1 Circular Cylinder in Cross-flow 1

1.2 Research Objectives 3

1.3 Outline of the Thesis 3

CHAPTER TWO: LITERATURE REVIEW 5

2.1 Introduction 5

2.2 Impulsively Started Flow around a Circular cylinder 6

2.3 Effects of Reynolds number on an Impulsively Started Flow 10

2.4 Effects of Acceleration Parameter on an Impulsively Started Flow 12

2.5 Impulsively Started Square Cylinder 14

2.6 Impulsively Started Flow over Other Bodies 15

CHAPTER THREE: EXPERIMENTAL APPARATUS AND INSTRUMENTATION 17

3.1 Introduction 17

3.2 Experimental Set-up 18

3.3 Seeding Particles 21

3.4 Velocity Field Measurements 23

3.5 Image Recordings 26
3.6 Data Processing 27
3.7 Impulsively Started Flow 32
3.8 Measurement Uncertainty 33
CHAPTER FOUR: CIRCULAR CYLINDER RESULTS AND DISCUSSION 38
4.1 Introduction 38
4.2 Velocity Fields 38
4.3 Length of the Recirculation Zone 42
4.4 Streamwise Location of the Primary Eddies 44
4.5 Cross-stream Spacing of the Primary Eddies 46
4.6 Circulation of the Primary Vortices 48
4.7 Maximum Vorticity within the Primary Vortex 50
4.8 Velocities along the Wake Centerline 51
CHAPTER FIVE: SQUARE CYLINDER RESULTS AND DISCUSSION 54
5.1 Introduction 54
5.2 Velocity Fields 54
5.3 Length of the Recirculation Zone 58
5.4 Streamwise Location of the Primary Eddies 59
5.5 Cross-stream Spacing of the Primary Eddies 61
5.6 Strength (Circulation) of the Primary Vortices 64
5.7 Maximum Vorticity within the Primary Vortex 66
5.8 Velocities along the Wake Centerline 68
CHAPTER SIX: DIAMOND CYLINDER RESULTS AND DISCUSSION 72
6.1 Introduction 72

6.2 Velocity Fields 73
6.3 Length of the Recirculation Zone 77
6.4 Streamwise Location of the Primary Eddies 79
6.5 Cross-Stream Spacing of the Primary Eddies 81
6.6 Strength of the Primary Vortices 82
6.7 Maximum Vorticity within the Primary Vortex 84
6.8 Velocities along the Wake Centerline 86
CHAPTER SEVEN: COMPARISON OF THE RECIRCULATION ZONES 89
7.1 Introduction 89
7.2 The Recirculation Zone for Re = 200 90
7.3 The Recirculation Zone for Re = 500 93
7.4 The Recirculation Zone for Re = 1000 96
CHAPTER EIGHT: CONCLUSIONS AND RECOMMENDATIONS 100
8.1 Conclusions 100
8.2 Recommendations 101
REFERENCES 103

NOMENCLATURE

English Symbols

a	acceleration [mm/s^2], streamwise location of the centers of the primary eddies [mm]
a^*	dimensionless acceleration parameter
a^{**}	alternative dimensionless acceleration parameter
AR	cylinder aspect ratio
b	transverse spacing of the centers of the primary eddies [mm]
D	cylinder diameter, side of the square or diamond cylinder [mm]
d_p	the diameter of the seeding particles [μm]
E	the overall error in a result
Ex_i	uncertainty in variable x_i
g	gravitational acceleration [m/s^2]
L	length of the cylinder [mm]
L_R	length of the recirculation zone [mm]
Re	Reynolds number
S	distance traveled by the cylinder following the start of the motion [mm]
T	temperature [°C]
t	time [s]
t^*	dimensionless time
U	steady freestream or towing (cylinder) velocity [mm/s]
U_g	induced velocity due to gravitational force [mm/s]
U_p	velocity of the particles [mm/s]
u	streamwise velocity component [mm/s]

v transverse velocity component [mm/s]

W length of the diagonal of the diamond cylinder [mm]

X result (in uncertainty analysis)

x streamwise coordinate [mm]

x_i variable (in uncertainty analysis)

y transverse coordinate [mm]

z normal coordinate [mm]

Greek Symbols

Γ circulation or vortex strength [m^2/s]

Γ^* dimensionless circulation or vortex strength

υ kinematic viscosity [m^2/s]

θ separation angle, measured from the front stagnation point [°]

ρ water density [kg/m^3]

ρ_p seeding particle density [kg/m^3]

τ_s relaxation time [s]

ω vorticity [s^{-1}]

ω^* dimensionless vorticity

ω_{max} maximum vorticity [s^{-1}]

ω^*_{max} dimensionless maximum vorticity

Abbreviations

2D two-dimensional

CC Circular cylinder

CCW counter-clockwise direction

CFD computational fluid dynamics

CW clockwise direction

DC Diamond cylinder

EC Elliptic cylinder

FP Flat plate

HOSC Higher-order semi-compact scheme

HOUS Higher-order upwind scheme

LBM lattice Boltzman method

LIPA laser-induced photochemical anemometry

PIV particle image velocimetry

SC Square cylinder

TDMA Tri-diagonal matric algorithm

CHAPTER ONE

INTRODUCTION

1.1 Circular Cylinder in Cross-flow

Flows around cylindrical objects are of great importance, thanks to the many engineering applications in which they are encountered (e.g. in building designs, oil storage tanks, electrical transmission and telephone cables, heat exchangers and offshore structures). The study of the flow around a circular cylinder has been ongoing for many years (e.g. Coutanceau and Defaye (1991), Lin *et al*., (1995), Williamson (1996), Zdravkovich (1997), Sumer and Fredsoe (2006)). However, the complexity of this problem has always necessitated further research work in order to fully understand the fluid mechanics phenomena involved.

A cylinder, by definition, is a two-dimensional body with uniform cross-section and length, L. A circular cylinder is a cylinder with a circular cross-section characterized by the diameter, D (Figure 1.1). A cylinder with square cross-section is called a square cylinder (or prism) while one with a diamond shaped cross-section is called a diamond cylinder (or prism). Both square and diamond cylinders are characterized using the dimension of one side, D. The ratio of the cylinder length to its characteristic dimension, i.e. the aspect ratio, AR = L/D, is an important parameter in classification of cylinders. An "infinite" cylinder is one with a large AR while a finite cylinder is one with a low AR.

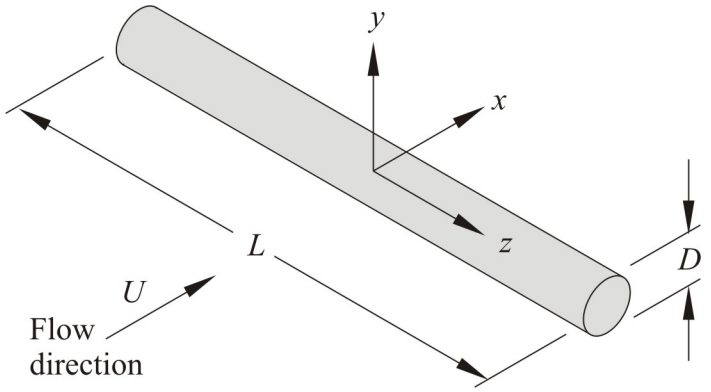

Figure 1.1: The nomenclature of a circular cylinder in cross-flow.

For a given Reynolds number, the flows around finite cylinders and infinite cylinders develop differently. The flow over a finite cylinder is a strongly three-dimensional flow while the flow around an infinite cylinder is basically two-dimensional (Williamson, 1996). Most real engineering applications involve finite cylinders, e.g. oil storage tanks, chimney stacks, lighthouses and television towers.

A cylinder can be immersed in a cross-flow that can be steady or unsteady. A steady flow is a flow whose velocity, U, does not change with time while an unsteady flow is a flow whose velocity changes with time, i.e. $U(t)$, where the cross-flow (freestream) may undergo some acceleration, deceleration or fluctuation in time, t. An impulsively started flow is a kind of unsteady fluid motion that results from a sudden change of the freestream flow velocity, from initially at rest to an instantaneous steady velocity.

In this research, the flow around impulsively started cylinders is studied experimentally using the particle image velocimetry (PIV) technique. PIV is an optical technique used to measure fluid velocity. It is an indirect way of measuring the velocity of a fluid since it measures the displacement of some tracer (seeding) particles that are added to the fluid. PIV uses no probes (which can introduce some disturbances to the flow); hence, it is a non-intrusive method of measurement. PIV is also a whole field technique since the

velocity of the entire flow field is obtained at once (Markus *et al*., 2007). The research looks at the initial stages of the flow following the impulsive start with particular emphasis on the wake development behind circular, square and diamond cylinders and the effects of the dimensionless acceleration parameter, a^*, and Reynolds number, Re.

1.2 Research Objectives

This research seeks to study the time development of flow over impulsively started circular, square and diamond cylinders at different acceleration parameters, a^* (= aD/U^2,where a is the acceleration) and Reynolds numbers, Re (= UD/υ, where υ is the kinematic viscosity). It also looks at the effect of Reynolds number and acceleration parameter on the growth and strength of the attached vortices and the length of the recirculation zone. The variation of the strength and location of the primary vortices with time are also examined. These experimental data for square and diamond cylinders are lacking in the literature yet they are needed to validate numerical simulations.

The experiments were conducted in an X-Y towing tank, using the tank's Y-axis motion stage. Use of the Y-motion stage imposed limits on the distance the cylinder could be towed, S, the dimensionless elapsed time, t^* (= tU/D), the final steady towing speed, U, and the acceleration, a^*. The experiments were therefore limited to $t^* < 5$ (where the wake remains mostly symmetric), Re = 200 to 1000 and a^* = 0.5 to 10.

1.3 Outline of the Thesis

In Chapter 2, a review of the background information and previous studies on impulsively started cylinders available in the literature is presented. Chapter 3 presents the instrumentation and methodology used in this research. The research facility together with

the methods and experimental procedures used in the research are described. In Chapters 4, 5, and 6, the results and discussion are presented. Each chapter is dedicated to the discussion of the results of one type of cylinder. Chapter 4 presents the results for the circular cylinder, Chapter 5 presents the results for the square cylinder, while Chapter 6 deals with the results for the diamond cylinder. In each chapter a detailed comparison of the recirculation zone at Re = 200, 500 and 1000 is made. Chapter 7 deals with the comparison of all the results for the three types of cylinders. Of importance is the way the recirculation zone develops for different cylinders at the same Reynolds number. Conclusions and recommendations are presented in Chapter 8.

CHAPTER TWO

LITERATURE REVIEW

2.1 Introduction

In this Chapter, a review of studies on the flow around impulsively started cylindrical objects is presented. The effect of the acceleration parameter and the Reynolds number on the impulsively started flow is examined from various past studies. Besides presenting the impulsively started flow around the circular and square cylinders, other studies on impulsively started flows around flat plates, elliptic cylinders, and non-rectangular prisms are also reviewed.

Two reference frames are normally employed in the study of impulsively started flows around cylinder: (i) the cylinder remains stationary and the flow of fluid is impulsively started, or (ii) the fluid is initially stationary (quiescent) and the cylinder is set into motion impulsively. Most numerical studies use the first approach (e.g., Koumoustakos and Leonard (1995), Lee *et al.* (1998), Li *et al*. (2004)) while most experimental work (including the present study) uses the second approach since it is more viable (this subject is discussed in further detail in Section 3.1).

An impulsively started flow is a flow that is set in motion within a very short duration (instantaneously). The flow is at rest in one moment and in the next moment it is in motion, with velocity U (graphically presented in Figure 2.1). The theoretical curve in Figure 2.1 represents an instantaneous jump to a constant velocity. The practical curves in the figure

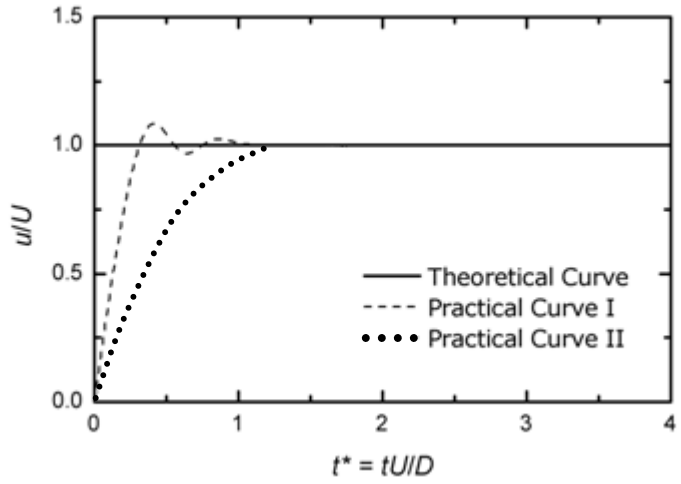

Figure 2.1: A graphical representation of an impulsively started flow: theoretical and practical curves, where *u* is the instantaneous velocity of the cylinder, *U* is the final steady velocity of the cylinder and *t is the dimensionless time.**

show what may really happen in actual applications: the flow has to accelerate from rest over some time, *t,* where its instantaneous velocity is *u*.

2.2 Flow around an Impulsively Started Circular Cylinder

Flow around an impulsively started "infinite" or two-dimensional circular cylinder is one of the classic problems in fluid mechanics. The flow is commonly used as a "benchmark" for the testing and validation of numerical simulations. The flow is geometrically simple but the phenomena behind it are complex. Many experimental and numerical studies have been done in an attempt to understand the physics behind the flow. Table 2.1 shows a summary of the recent works on impulsively started cylinders together with the method used and the range of Reynolds numbers examined by each study.

Honji and Taneda (1969) examined the flow phenomena around an impulsively started circular cylinder. They observed the flow development from the time the cylinder was set into motion and explained the mechanism of separation. Nagata *et al*. (1975, 1985a,b) performed elaborate studies of the unsteady flow over an impulsively started circular

Table 2.1: A summary of some selected recent research work on impulsively started cylinders, CC- circular cylinder, SC – square cylinder, DC – diamond cylinder, EC – elliptic cylinder, FP – flat plate.

(a) Experimental			
Author(s)	**Re**	**Method**	**Cylinder Type**
Jeon and Gharib (2004)	1000-2000	PIV	CC
Sumner *et al*. (1999)	1200-3800	PIV	Tandem CC
Sarpkaya (1991, 1992)	16200-33200	Force balance	CC
Chu and Liao (1992)	500-3000	LIPA	CC
Nagata *et al*. (1985a, b)	1200	Visualisation	CC
Bouard and Coutanceau (1980)	40-10^4	Visualisation	CC
Nagata *et al*. (1979)	250 – 1000	Visualisation	CC
Taneda (1977)	99-1200	Visualisation	CC
Honji and Taneda (1969)	31-1700	Visualisation	CC
(b) Numerical			
Author(s)	**Re**	**Method**	**Cylinder Type**
Dupuis et al. (2008)	200	LBM	CC
Sanyasiraju and Manjula (2005)	20-5000	HOSC	CC
Li *et al*. (2004)	40-550	LBM	CC
Koumoutsakos and Leonard (1995)	40-9500	Vortex method	CC
Lee *et al*. (1998)	25-1000	TDMA	Non-rectangular
Nair and Sengupta (1996)	10000	HOUS	CC and EC
Smith and Stansby (1988)	105-2500	Vortex-in-cell (VIC)	CC

cylinder. They studied the vorticity feeding mechanisms and the onset of turbulence, the pressure distribution on the surface of the cylinder as well as the velocity fields and circulation measurements. Nagata *et al.* (1989) used the hydrogen bubble technique to

estimate the boundary layer thickness of the impulsively started cylinder and to determine the circulation of the primary vortices.

Coutanceau and Bouard (1977a,b) did experimental investigations of a circular cylinder in both steady and unsteady flow at low Reynolds numbers. They identified the major flow features such as wake evolution. Perhaps as extensions of their earlier research work, Nagata *et al.* (1979) and Bouard and Coutanceau (1980) studied the initial features of flow past an impulsively started circular cylinder experimentally using flow visualization. Examining the flow at several instances of non-dimensional time t^* (where $t^* = tU/D$, for the time elapsed, t) at early stages of flow, they observed the formation of a symmetric recirculation zone in the wake of the cylinder. They also quantified the recirculation zone by measuring the length of the zone, L_R, the streamwise location, a, and the cross-stream spacing, b, of the primary vortex centers, as well the circulation, at various time intervals.

The recirculation zone contains stationary, steady twin (primary) vortices of equal strength and opposite rotation, as shown in Figure 2.2. This structure is observed for a wide range of Reynolds number. After some time the twin vortices start to elongate in the streamwise direction. The sizes of the attached vortices grow with time, until they become asymmetrical and eventually they are shed forming the familiar von Kármán vortex street.

The time at which the recirculation zone and the primary eddies become asymmetric varies from study to study and with the Re. For example, from flow visualization experiments, Finaish (1991) observed that for Re = 200, the recirculation zone begins to be asymmetric after $t^* = 6.1$ and alternate vortex shedding begins at $t^* = 11.4$. Koumoutsakos and Leonard (1995) and Li *et al.* (2004), on the other hand, using numerical methods, found that the asymmetry begins at $t^* = 3.5$ at Re = 550. Early experiments by Taneda (1977) at

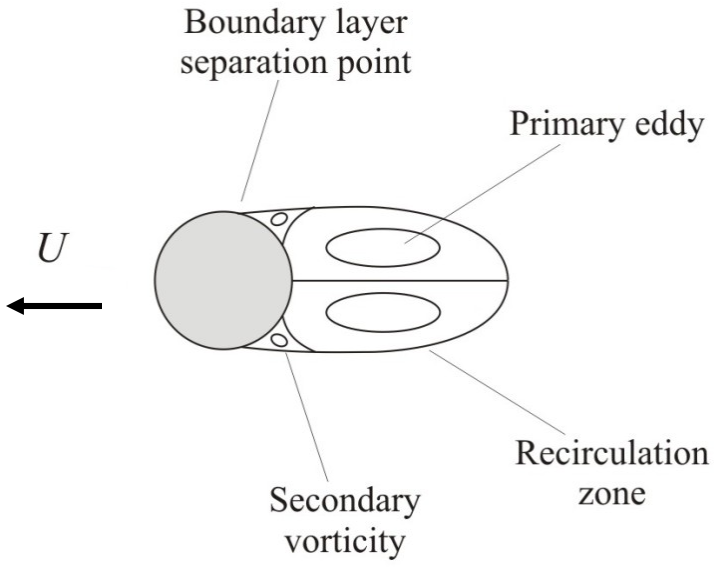

Figure 2.2: The main features of the flow around an impulsively started circular cylinder at Re = 550, t^* = 1.5.

very low Re noted the onset of asymmetry at t^* = 8.0 at Re = 17.7. Bouard and Coutanceau (1980), in their experiments from Re = 40 to 10,000, found the flow remained symmetric up to t^* = 3.5 (which was the upper limit in their experiments).

More recent experimental studies by Jeon and Gharib (2004) used PIV to study the vortex formation process and the wake patterns. In addition to looking at the time evolution of the primary vortices, they also quantified the recirculation zone by calculating the circulation.

The many numerical simulations for impulsively started circular cylinders carried out in the recent past (some are shown in Table 2.1(b)) is possibly due to the advancement of computer technology that has led to the creation of computers which are able to handle and process large amounts of data. For example, Chang and Chern (1991) used a numerical method to study the impulsively started flow around a circular cylinder. They showed the flow development with time and the variation of forces on the surface of the cylinder with time. Recent numerical studies by Dupuis *et al*. (2008) and Li *et al*. (2004) using the lattice

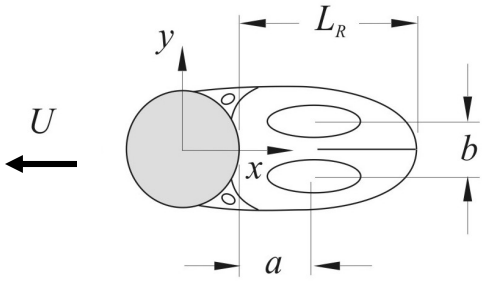

Figure 2.3: Geometric parameters of the closed wake for an impulsively started circular cylinder.

Boltzman method (LBM) also showed the growth of the recirculation with time and the variation of the drag force with time. Sanyasiraju and Manjula (2005) also used a numerical method (higher-order semi-compact scheme, HOSC) to simulate the flow past an impulsively started circular cylinder over a wider range of Re. Besides the flow development with time, their simulations also showed the variation of the vorticity on the cylinder surface at various Reynolds numbers.

2.3 Effects of Reynolds Number on Impulsively Started Motion

The Reynolds number, defined as Re = UD/υ, (where U is the steady velocity of the cylinder attained following the impulsive start and υ is the kinematic viscosity), influences the wake evolution of an impulsively started circular cylinder. Bouard and Coutanceau (1980) studied the wake development for an impulsively started circular cylinder for Re = 40 to 10,000. Their experimental study is still considered to be the most comprehensive, and is widely used for validating numerical simulations. Based on the Re, they categorized flow into three types, corresponding to low, moderate and high Reynolds number.

At low Reynolds numbers, $4.4 < \text{Re} < 60$, and for small time intervals, $t^* < 5$, the flow develops with no separation. However, after a short time interval the main (primary) eddies are formed in the recirculation zone. Li *et al*. (2004) noted that in this category, the

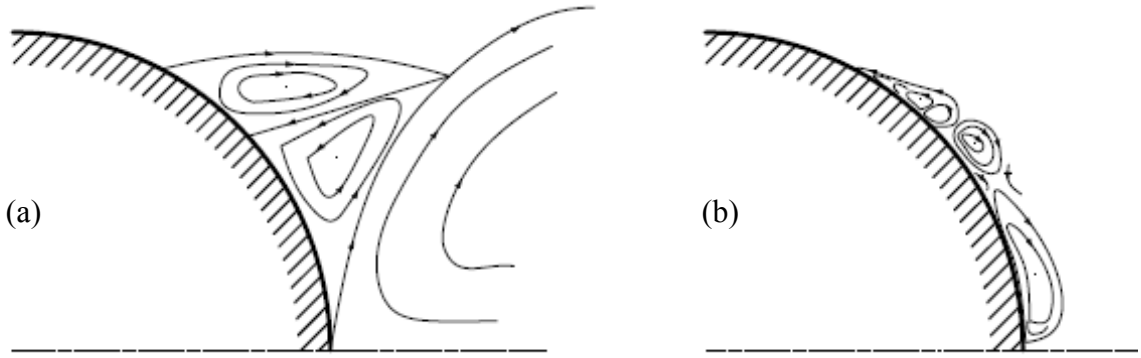

Figure 2.4: The schematic representation of the secondary eddy pair: (a) α phenomenon, (b) β phenomenon.

flow is able to reach a steady velocity after an impulsive start, without any vortex shedding or asymmetry. This range of Re is characterized by a steady increase in the recirculation zone length, L_R, and the location of the primary vortex in the streamwise direction, *a* (Figure 2.3).

For 60 < Re < 550 (corresponding to the moderate range of Re), the secondary phenomenon of the wake starts to appear. The streamlines display some bulges after separation and there is a large reduction in the velocities. The bulges eventually develop into secondary vortices just above the main eddies (Figure 2.2). The isolated secondary eddies rotate in the opposite direction to that of the main eddies. Although the secondary vortices are not observed in steady flow, various studies have shown a slight difference in the Re at which the secondary vorticity begins to appear in impulsively started flows. Honji and Taneda (1969) and Bouard and Coutanceau (1980) both reported the appearance of the secondary vorticity at Re ≥ 550 while Nagata *et al*. (1975) reported the appearance at Re ≥ 520.

The time development of the flow above Re = 550 (corresponding to high Re) is complicated by the appearance of two phenomena: the α and β phenomena. The α phenomenon is a pair of secondary vortices of equivalent size and strength which results

from the splitting of the main eddy into parts by the secondary eddy (Figure 2.4(a)). The α phenomenon is distinctively visible from the numerical calculation of Ta Phuoc Loc and Bouard (1985) for Re = 3000 at $t^* = 4.5$ and 5.5. In the moderate Re range, Koumoutsakos and Leonard (1995) observed the phenomenon at $t^* = 2.5$, for Re = 550 from numerical simulations. The β phenomenon, on the other hand (Figure 2.4 (b)), is the first pair of secondary eddies that appears immediately after an impulsive start and disappear to pave way for the formation of the second pair of the secondary eddies. Bouard and Coutanceau (1980) noted that for Re > 3000, the β phenomenon can be observed at very early phase of the flow establishment, at $t^* < 1.5$.

2.4 Effects of Acceleration Parameter on the Impulsively Started Motion

Although it is computationally and theoretically possible to get a true impulsively started motion (e.g. in computational fluid dynamics (CFD) simulations), it is experimentally impossible. In practice, there will be a brief acceleration phase where the fluid or the object has to accelerate to a steady velocity (Figure 2.1). The acceleration phase has been quantified using a dimensionless acceleration parameter, either a^*, defined as $a^* = aD/U^2$, or a^{**}, defined as $a^{**} = aD^3/\upsilon^2$, where a is the acceleration. The acceleration parameters, together with the Reynolds number, are the main governing parameters in the study of impulsively started flows (or non-impulsively started or accelerated flows).

The practical case, therefore, is an approximation of the ideal impulsively started flow. Depending on the nature of the test facility, an experimental curve (shown in Figure 2.1) may have an overshoot to reach a peak velocity (curve I) that finally settles down to the

desired velocity but with some fluctuations, or may just approach a steady value without an overshoot (curve II). Huang *et al.* (1989) used a motion system whose velocity characteristics showed an overshoot, reaching its peak after $t^* = 0.01$ (equivalent to $a^* = 100$). When studying the starting vortex behind impulsively started bluff bodies in a water channel, Lian and Huang (1989), used a test facility where the velocity of water at the test section accelerated gently at different rates to the desired velocity (curves similar to the practical curve II). It is fair to say, however, that few experimental studies in the literature have quantified the acceleration (or velocity-time profile) used to attain an "impulsive start."

Experimental studies have been made to determine conditions under which a flow can be said to be impulsively started. Sarpkaya (1991), from his experimental work based on force measurements at Re = 16,200 to 33,200 (probably the highest Reynolds numbers at which this flow has been studied), examined such conditions and concluded that the flow could be considered impulsively started if $a^* > 0.27$. Essentially, a truly impulsively started flow has an infinite acceleration (i.e. $a \rightarrow \infty$). Therefore, the higher the acceleration parameter, a^* or a^{**}, the more close is the experiment to a true impulsive start. An increase in a^* or a^{**}, however, cannot go on indefinitely. There reaches a point where any further increase does not make any meaningful change in the flow and flow features. This 'cut off' point is a point beyond which the flow becomes independent of a^* or a^{**}, meaning that the conditions of approximating an impulsive start have been attained. There has not been much study done to establish this point and it is part of this current work.

2.5 Impulsively Started Square Cylinder

A square cylinder is a long slender bluff body with a square cross-section. It has sharp edges which are potential points of flow separation if the flow Reynolds number is sufficiently high. Previous studies in *steady* flow for low Re (e.g. Sumer and Fredsoe, 2006)) show that for Re < 5, the flow over a bluff body (including a square cylinder) occurs without any separation – this is known as creeping flow. Compared to the circular cylinder, there have been relatively few studies (experimental or numerical) of the impulsively started flow around a square cylinder.

Using a visualization technique, Finaish (1991) observed the gradual growth of the recirculation zone behind a square cylinder in impulsively started flow at Re = 200. Although he did not show quantitatively the variation of various flow features with time, he did manage to show the time-evolution of the primary eddies from the initial stages of formation to the vortex shedding regime.

Lee *et al.* (1996) used a numerical method to study impulsively started flow past a square cylinder at the early stages. He observed the formation and the time development of the recirculation zone. He noted that the recirculation zone formed at the back of the cylinder was due to the flow separation at the trailing edge of the cylinder. His simulations showed that the flow development behind an impulsively started square cylinder was dependent on the Reynolds numbers. At low Re, the initial stages of an impulsively started flow around a square cylinder were characterized by the absence of visible flow separation or reattachment while for high Re, the recirculation zone grew faster due to the flow separation occurring at the leading edges of the square cylinder.

Lee *et al.* (1996) also noted that at lower Re the length of the recirculation zone increased in an almost parabolic manner whereas for higher Re the recirculation length increased almost linearly with time in the initial stages of the flow but reached a point where there was no further change in the recirculation length irrespective of a change in time. This observation remains to be confirmed with the current experimental studies. Also from their numerical simulations, no secondary vortices were observed and the flow remained symmetric to very high values of t^*, much higher than for circular cylinder experiments and simulations (see Figure 3 in Lee *et al*., 1996). It is noted, however, their numerical simulations were not validated against any experiments.

2.6 Impulsively Started Flow over Other Bodies

Researchers have also examined impulsively started flow around other bodies, such as flat plates, elliptic cylinders, and airfoils.

Like any other impulsively started flow, an impulsively started flow over a flat plate (in vertical orientation with the flow directly perpendicular to its surface) is irrotational everywhere just at the start of motion. There is, however, a small separation region near the sharp edges. Then immediately afterwards, a wake bubble (vortex pair) appears at the rear of the plate. Taneda (1977), from visualization experiments, observed that the vortex sheet starts to form from the edges of the plate and deforms so that the edges wrap themselves into spirals.

A more extensive experimental study of an impulsively started flow over a flat plate was done by Lian and Huang (1989). They observed the growth of the vortices behind the impulsively started flat plate and examined the growth of the recirculation zone with time. The recirculation zone, formed at the back of the plate, contains a pair of symmetrical

vortices which grow with time, then become asymmetrical and are eventually shed. The vortex development was similar to that behind the impulsively started circular and square cylinder but with no formation of secondary eddies. Finaish (1991) performed a flow visualization of vortex shedding from an impulsively started flat plate at a 50° angle of attack. His visualization and numerical simulation matched very well.

Nair and Sengupta (1996) examined the flow over an impulsively started elliptic cylinder. They noted that for an elliptic cylinder at $\theta = 0°$ (where the major axis is parallel to the flow), a small isolated vortex begins to form immediately after the start of the impulsive motion and is convected downstream. The recirculation zone formed at the back of the elliptic cylinder continues to grow steadily with time. As opposed to the case of a circular cylinder, asymmetry in the attached vortices is reached earlier for elliptic cylinders.

Izumi and Kuwahara (1983) studied extensively the flow field around an impulsively started elliptic cylinder and circular-arc airfoil. They particularly examined the development of the flow field for various angles of attack and showed the relationship between the unsteady forces acting on the body and the corresponding changes in the flow fields.

Impulsively started flow over prisms with non-uniform cross-section, on the other hand, is mostly affected by the taper of the prism and Reynolds number. For Re < 45 the flow develops with time without a visible flow separation within the first few time steps, but thereafter separation starts to occur from the rear surface of the prism and form aft-end symmetrical eddies within a recirculation zone. From his numerical calculations, Lee (1998) showed that the twin eddies start to develop when $t^* > 1.5$, for Re = 500. At this point the length and width of the recirculation zone remains smaller than the width of the aft end of the prism.

CHAPTER THREE

EXPERIMENTAL APPARATUS AND INSTRUMENTATION

3.1 Introduction

This research is a purely experimental study of unsteady flow over cylindrical objects. Experiments involving unsteady fluid motion can be conducted in two ways: (i) the object can be towed in a quiescent fluid, or (ii) the fluid itself can be accelerated over a stationary object. Although both options are experimentally possible, to precisely control the motion of an object in a quiescent fluid is much easier than to control the flow parameters of a large volume of fluid. And also, to move an object through a stationary fluid requires less power than accelerating and maintaining the velocity of a large mass of fluid. It is for these reasons, coupled with the availability of a towing tank, that the first option was adopted for this research.

A water towing tank is an experimental research tool commonly used in the aerodynamic and hydrodynamic studies (Gad-el-Hak, 1987). The size of a towing tank depends on the scale of the research. Large towing tanks are found in big research centers, e.g. naval research institutes, while small-scale versions of the facility, commonly used in the study of unsteady flows, are found in some fluid mechanics laboratories. Recent applications show that the towing tank is suitable for flow visualization and particle image velocimetry

(PIV) techniques. For example, Huang *et al.* (1999) studied the vortex evolution of an impulsively started wing using PIV in a towing tank while Sumner *at al*. (1999) investigated an impulsively started flow around tandem cylinders using PIV in a towing tank.

Other advantages of the towing tank are that it provides the ability to study accelerating and decelerating flows with ease and with negligible turbulence intensity (Gad-el-Hak, 1987). There are, on the other hand, some disadvantages associated with the use of the towing tank, including (i) the effect of the limited running time as a result of the finite length of the tank, (ii) the sensitivity of the motion to the vibration which may be transmitted by the model to the fluid, (iii) the water must be stationary before the start of every experimental run and (v) the sensitivity of the water to the external conditions, e.g. the contamination and changes in temperatures, as was shown by Anagnostopoulos and Gerrard (1976).

Nevertheless, the towing tank has been a facility of choice for studying unsteady flows in fluid mechanics since most of the associated disadvantages can be minimized to negligible values or avoided altogether. Experiments by Taneda (1977), Nagata *et al*. (1979), Bouard and Coutanceau (1980), Chu and Liao (1992), Huang *et al.* (1999), Sumner *et al*. (1999) and Jeon and Gharib (2004), all done in towing tanks, confirm the importance of a towing tank as a research facility in fluid mechanics. Other researchers, such as Lian and Huang (1989) and Sarpkaya (1991), opted to use water tunnels in their works for various reasons.

3.2 Experimental Set-up

The experiments were conducted in an X-Y towing tank (Figure 3.1) with ordinary tap water as the working fluid. The tank, whose internal dimensions are 3960 mm long, 1030

mm wide and 750 mm deep, has an open top with glass side walls, end walls, and floor to give optical access for the PIV system. The primary towing direction (X-direction) runs along the length of the tank and has a 3.5 m. The main carriage straddles the tank width and moves on two parallel rails. It is driven by two timing chains and a stepping motor. A linear motion stage, containing the secondary carriage is mounted on the main carriage and used for transverse movement across the tank (Y-direction, 280 mm length of travel). The secondary carriage is mounted between two parallel rails and is driven by a lead screw and a stepping motor.

The motion control system consists of a National Instruments (NI) PCI-7344 motion controller card, two Intelligent Motion Systems IM1007 micro-step drivers (configured at 1600 steps/revolution for both axes), a NI UMI-7764 universal motion interface and a personal computer (Intel Pentium 4 Processor). The encoders on each axis provide feedback while the home and limit switches used on both axes control the start and end positions for the motion trajectories. Further details on the X-Y towing tank are described by Sumner *et al*. (2005).

The user interface, written in the LabVIEW programming language, enables the user to enter the variable parameters of the test and to monitor the motion of the object on the display screen. The parameters that are entered by the user are the diameter of the cylinder, D, the temperature of the water (in degrees Celsius), the acceleration parameter, a^*, and the Reynolds number, Re. Using this information, together with the program in-built formulae and fundamental constants, the program calculates and displays the expected final velocity of the object, the acceleration of the object, the alternative acceleration parameter (a^{**}), the water density and the viscosity.

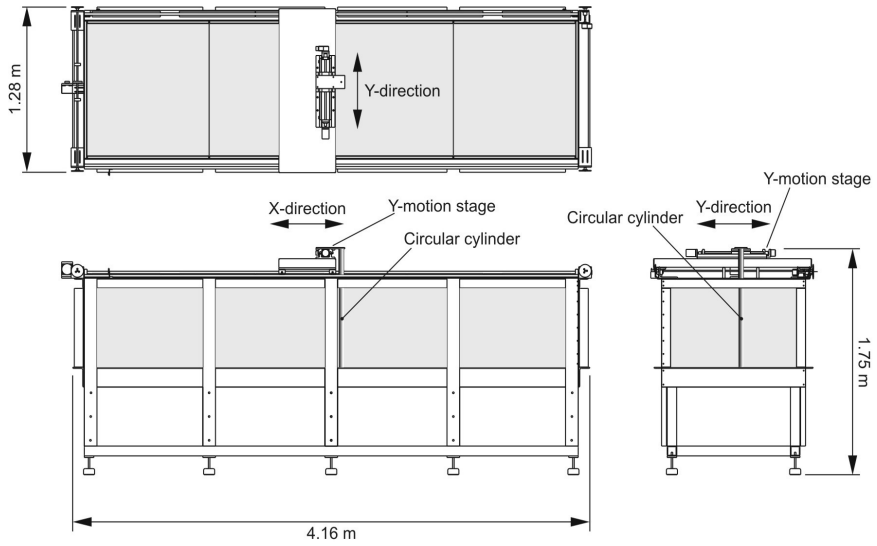

Figure 3.1: Three-view drawing of the X-Y towing tank, showing the circular cylinder suspended in the water beneath the Y-motion stage.

Owing to the presence of other experiments set up along the length (X-direction) of the towing tank, all experiments in this research were carried out along the width, in the Y-direction. This axis has a smaller length of travel and therefore the maximum possible experimental results were limited to the early development of the flow around the impulsively started cylinders up to $t^* = 11$.

A circular cylinder of diameter D = 25.4 mm and a square cylinder with sides D = 25.4 mm, were used, one at a time. To obtain a diamond-shaped cylinder, the square cylinder was inclined 45° to the direction of motion. The cylinder was suspended in the water vertically beneath the Y-direction motion stage (Figure 3.1) using a specially designed bracket that ensured that the cylinder was tight and vertical. Table 3.1 specifies the range of the working parameters in the present experiments.

The working depth of water in the towing tank was maintained at 720 mm. When the cylinder was immersed, a small gap of 16 mm (0.63D) between the end of the cylinder and the bottom of the tank was left, giving a cylinder aspect ratio of AR ≈ 28, which ensured that

Table 3.1: The range of experimental parameters used in this research.

Re	a^*	a [mm/s^2]	t^* [end of acceleration]	U [mm/s]
200	10	25.2	0.1	7.5
500	0.5	7.9	2.0	20
	1	15.7	1.0	
	3	47.2	0.3	
	5	78.6	0.2	
	10	157	0.1	
1000	3	188.7	0.3	40
	5	314	0.2	

a two-dimensional (2D) flow was maintained at the central portion of the cylinder. Slaouti and Gerrard (1981) after studying the end effect of a circular cylinder concluded that a more 2D flow is achieved by minimizing the size of the gap between the bottom end of the cylinder and the bottom of the tank; they recommended a gap of between 0.15D and 0.2D based on their experiments at Re = 75 and 100.

3.3 Seeding Particles

PIV is based on the determination of the two fundamental dimensions of velocity – the length and the time. However, the measurements are indirect since PIV determines the movement of the seeding (tracer) particles, i.e. the displacement or velocity of the tracer particles. The tracer particles, therefore, should be able to trace the flow faithfully to avoid any significant variation in the motions. The choice of the appropriate tracer particle depends on the medium where they will be used, their light scattering ability, the sizes of the particles, the density, their availability, and costs (Markus *et al*., 2007).

The gravitational force may be a major cause of error in PIV. It results when there is a disparity in the densities of the fluid and the tracer particles. This makes the particles settle

very fast at the expense of tracing the fluid motion. If d_p is the particles' diameter, ρ_p and ρ are the particle and water densities, respectively, and μ is the viscosity of the water, then from the Stokes' drag law, the induced velocity, U_g, due to gravitational force is given by

$$U_g = d_p^2 \frac{(\rho_p - \rho)}{18\mu} g. \tag{3.1}$$

In a continuously accelerating fluid, the velocity lag, U_s, of a particle is given by

$$U_s = U_p - U = d_p^2 \left(\frac{\rho_p - \rho}{18\mu} \right) a, \tag{3.2}$$

where U is the free stream velocity, U_p is the particle velocity and a is the acceleration (Markus *et al.,* 2007)

An impulsively started flow is equivalent to the application of a step increase in the flow velocity. Typically, the particle velocity in such a case follows an exponential law if the density is much greater than the fluid density (Markus *et al.,* 2007),

$$U_p(t) = U\left[1 - \exp\left(\frac{-t}{\tau_s}\right)\right], \tag{3.3}$$

$$\tau_s = d_p^2 \frac{\rho_p}{18\mu}, \tag{3.4}$$

where t is the time and τ_s is the relaxation time.

In their review, Markus *et al*. (2007) discussed various types of tracers that can be used with liquid flows including polystyrene, aluminium flakes, and hollow glass spheres. They noted that aluminium flakes have very small size particles that are ideal for accurate tracing of motion but poor in light scattering ability. On the other hand, polystyrene and hollow glass spheres have the same range of particle sizes and good light scattering ability; hence the choice between the two is basically the availability and cost.

The availability of the hollow glass spheres together with their reasonable cost made them the choice for this research. The hollow glass spheres came as a white powder, with particles 8 – 12 μm in diameter. They are insoluble in water and have a relative density of 1.1, very close to the density of water. From Equation (3.1), this small difference in the densities causes a gravitational induced velocity, $U_g \approx 3.5\times10^{-5}$ m/s, a velocity lag upon a constant acceleration of between 1.8×10^{-13} m/s (for $a^* = 0.5$) and 3.5×10^{-12} m/s (for $a^* = 10$) (Equation (3.2)) and a relaxation time $\tau_s \approx 1.0\times10^{-5}$ s, (Equation (3.5)). These are very negligible values and thus it can be concluded that the tracer particles used in the present study trace the fluid flow accurately.

3.4 Velocity Field Measurements

The velocity fields were measured using a TSI PIV system. The system is made up of three major components: the laser, the camera, and computer software to process the captured images.

The laser light sheet, of wavelength $\lambda = 532$ nm, was supplied by a 120 mJ/pulse dual Nd:YAG Gemini PIV 15 laser from New Wave Research (Figure 3.2). The Nd:YAG is a solid state type of laser commonly used in PIV systems. The laser had a maximum pulse frequency of 15 Hz and was positioned 350 mm from the side wall of the tank. The operating pulse frequency of the laser was chosen based on the velocity (determined by Re) of the cylinder – a frequency of 3.75 Hz was used for Re = 200, 7.5 Hz for Re = 500 and 15 Hz for Re = 1000. To produce a laser sheet, the light sheet optics used were a 50-mm cylindrical lens and 1000-mm spherical lens.

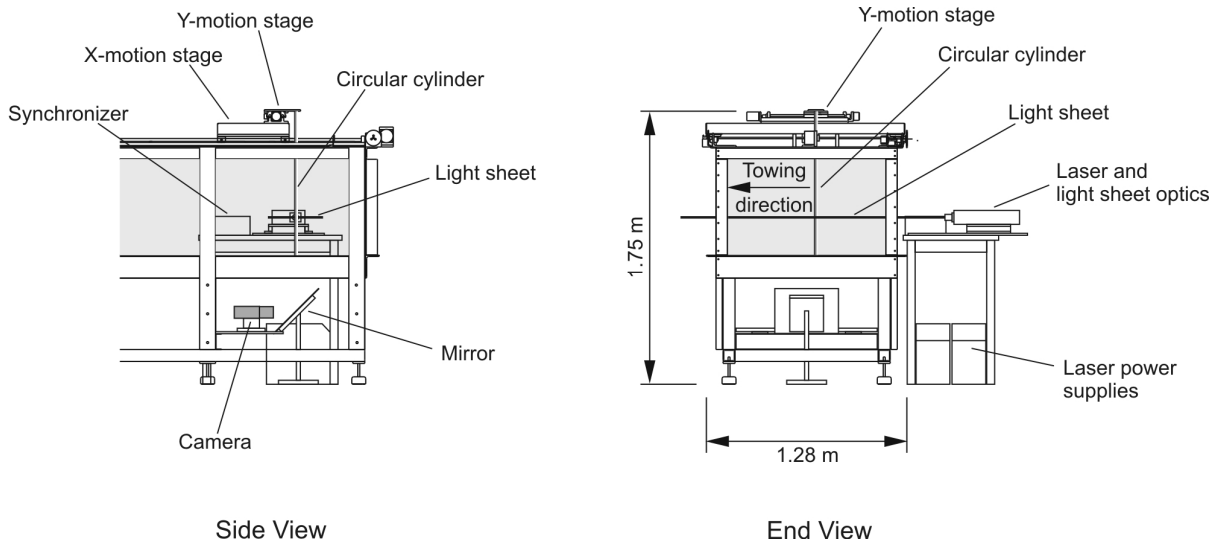

Figure 3.2: The experimental set-up for the PIV experiments in the X-Y towing tank (only a partial side view is shown). The cylinder is suspended vertically in the water from beneath the Y-motion stage. The laser light sheet forms a horizontal plane that intersects the cylinder axis. The cylinder is towed from right to left, as shown in the end view. The camera remains at a fixed position beneath the tank. Images are acquired with the aid of a mirror set at 45 degrees, as shown in the side view.

The light sheet from the laser was about 5 mm thick and cut through the cylinder at 294 mm (11.6*D*) above the lower end of the cylinder. Because the plane of measurement was more than 4*D* from the lower end of the cylinder and the fact that the gap between the cylinder and the bottom of the tank is small, the end effects, were not expected to influence the flow (Slaouti and Gerrard, 1981); hence no end plates were used.

In the experiments for the circular cylinder, Re = 500, a TSI PIVCAM 10-30 model (1 Megapixel) camera fitted with a Sigma 28-105 mm f/2.8-4 zoom lens was used for image acquisition. The camera was mounted horizontally (shown in Figure 3.3(a)) at a fixed location beneath the tank and captured the moving cylinder images through a mirror inclined at 45° (Figure 3.2). The images were captured by a frame grabber (90 MB/s TSI model 600068 High-Speed Camera interface) on a dual processor (Intel Pentium III, 1-GHz) computer.

(a)

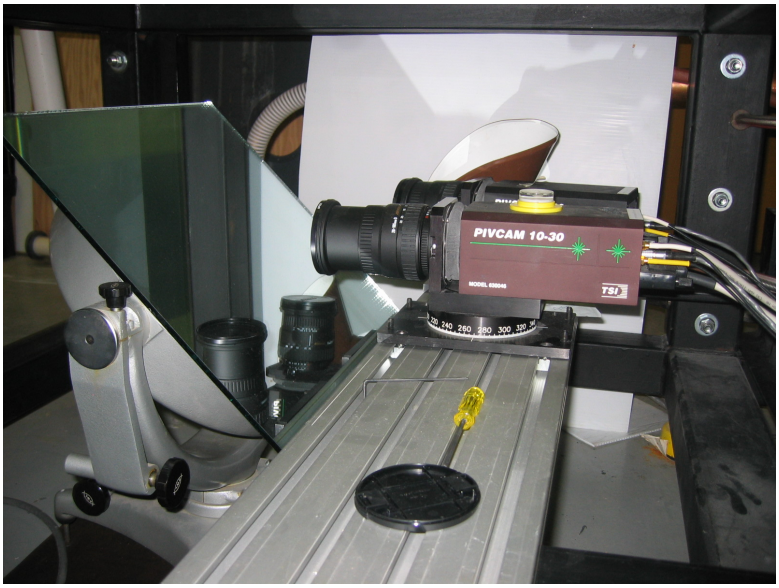

(b)

Figure 3.3: The orientation of the PIV camera during the experiments: (a) horizontal orientation with a mirror, and (b) vertical orientation.

In all the other experiments, a TSI PowerView Plus 2MP (2 Megapixel) PIV camera was used. Unlike the earlier type, the camera was positioned facing upwards underneath the

tank, (Figure 3.3(b)). This orientation eliminated the use of a reflecting mirror and instead the images of the moving cylinder were captured directly. Any alignment errors that resulted from the earlier arrangement were significantly reduced. A new computer (Intel Pentium IV, 2 GHz), a new frame grabber and new software (Insight 3G) were also used with this camera.

The field of view in the first part of the experiments (circular cylinder, Re = 500), taken using the TSI PIVCAM 10-30 camera, was 75 mm × 75 mm, resulting in velocity vector fields of 55 × 55 vectors with a vector spacing of approximately 0.054*D*. For the rest of the experiments, taken using the TSI PowerView Plus 2MP camera, the field of view was typically 92 mm × 68 mm, resulting in rectangular velocity vector fields of 56 × 41 vectors, with a vector spacing of 0.065*D*.

3.5 Image Recordings

For the circular cylinder experiments at Re = 500, a TSI LaserPulse synchronizer together with TSI Insight 5 software was used for timing, while for the rest of the experiments the same synchronizer together with TSI Insight 3G software was used. The data recordings were done using the multi-frame/single exposure technique. The images were recorded on a two frame straddle mode setting as shown schematically in Figure 3.4.

The interval, Δt, between the image recordings of frame A and B, also called the pulse separation, is an important parameter that determines the quality of the PIV recordings. It determines how far a particle would move between the two laser pulses. If Δt is too small the particles would barely move between the two frames and if it is too large, the particles would move out of the frame. As a rule of thumb, the aim was to ensure that the maximum

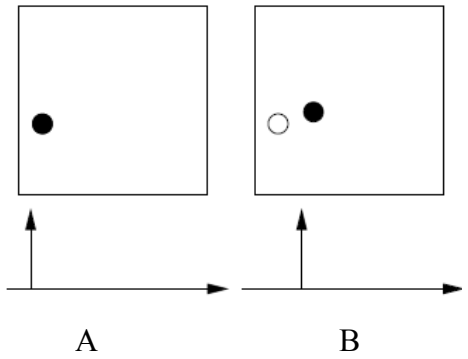

Figure 3.4: The two frame straddle mode of PIV image recording, frame B recorded shortly after frame A.

distance moved by the particle between the two frames was a quarter of the interrogation spot (16 pixels for a 64-pixel spot) (TSI, 2008).

Therefore, the Δt value was varied to match the flow velocities which was determined by Re. Regardless of the type of cylinder, for Re = 200, Δt = 10,000 ms was used and for Re = 500, Δt = 8000 ms while for Re = 1000, Δt = 2500 ms was used.

3.6 Data Processing

Once the images have been captured, recorded and stored, they can then be processed. The processing involves the analysis of the image pairs to determine how far the particles moved between the frames and because the time between the frames is known, the velocity vector can then be established. Since there are so many particles captured in each frame, it is not computationally possible to analyze the motion of each particle individually. Instead, a statistical approach using an interrogation scheme is used. The image is sub-divided into small regions called interrogation spots where the particle image displacements are averaged to obtain the flow velocity.

The data processing was done using the TSI Insight 5 or Insight 3G software. The first step in data processing is to break down the image into small spots – the interrogation

spots-using a grid generation engine. Insight 3G software provides a variety of grid generation engines including Nyquist, Recursive Nyquist grid and Rectangular grid. The Nyquist grid generation engine is a classic PIV grid which processes the vector field in a single pass and a 50% overlap fitting the Nyquist sampling criteria. Because it is faster, Nyquist grids with spot sizes of 32 × 32 pixels (for Insight 5) and 56 × 56 pixels (for Insight 3G) were used for data analysis in this research.

Once the interrogation spots have been generated, they need to be conditioned before being passed to the correlation engine. The conditioning of the spots is aimed at increasing the signal-to-noise ratio (SNR). For these data analyses, a zero pad mask engine was used since it increases the SNR (TSI, 2008).

The correlation engine computes the correlation function of the masked spot A and B and returns the results as a correlation map. The correlation function is an algorithm that represents the sum of all displacements of the particle image matches within the displacement range. The coordinates of the correlation plane are the two components of displacement- x and y. The highest correlation map pixel is the particle displacement peak and is assumed to be a contribution of the several particle pairs. In TSI Insight 3G software, there are three correlation engines that can be selected for data processing – the Fast Fourier Transform (FFT), Hart correlation and the direct correlation. The Hart correlation is a form of direct correlation method that processes only the most significant pixels in order to improve the processing speeds. After a number of trial and error using various correlation engines, the Hart correlation was found to be much faster and gave good results. Figure 3.5 (from one the images processed) shows a clear peak.

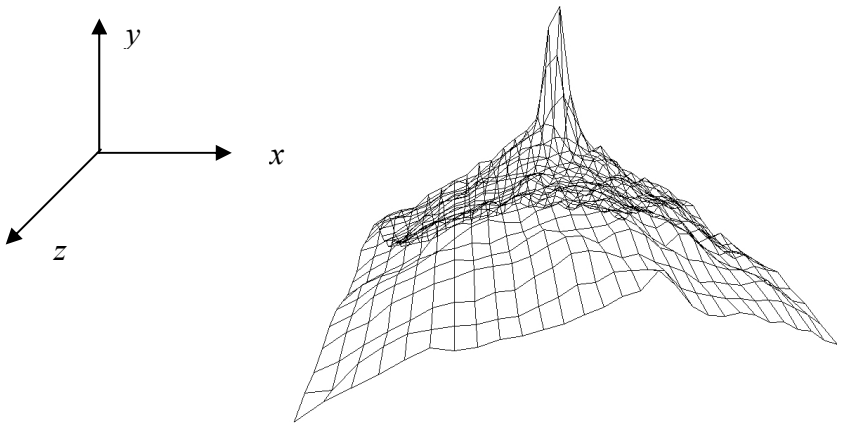

Figure 3.5: The distinct peak obtained by using Hart correlation and located using the bilinear peak algorithm (circular cylinder, Re = 1000, t^* = 1.8).

The correlation algorithms more often than not generate peaks of different sizes, slopes and shapes. Therefore, choosing the right peak is essential in order to improve the accuracy. The measurement accuracy is greatly improved by matching the right peak algorithm to a correlation algorithm. Default peaks provided by most correlation engines are deemed the best match for the correlation engine. Two peak algorithms are available for use in Insight 3G software: Gaussian peak and bilinear peak. In the Gaussian peak algorithm, the peak is located with sub-pixel accuracy using a Gaussian curve fitted to the highest pixel and four of its neighbors while the bilinear algorithm, the correlation peak is located with sub-pixel accuracy by using sets of linear functions fitted to the highest pixels and four of its neighbors (TSI, 2008). In order to match the Hart correlation algorithm used for correlation, the bilinear peak algorithm was used for peak detection.

Even with excellent settings and good procedure, PIV measurements can never produce 100% correct velocity measurements. The existence of some lost pairs due to in-plane and out-of-plane motion, or low seeding density result in low correlation signal strength and in turn lead to spurious vectors. This happens when the highest peak is picked not from the particles moving with the flow but from other random pairing of particles. To

eliminate these spurious vectors and to fill the resultant holes using interpolation, the vector field validation functions are used. The vector validation in Insight 3G is done as a post-processing step.

The best post-processing procedure was determined after performing a number of trial and error procedures involving the variation of various parameters, e.g. the neighborhood size, the velocity tolerances and even the number of filters used. The final procedure developed involved both local and global validation of the vectors. As the first step of vector validation, local validation was done using a mean test with a 5 × 5 neighborhood size and a velocity tolerance of 1 pixel. This test identified the bad vectors in the midst of 25 neighboring vectors. The bad vectors were replaced by the local median. Then, a global validation using an absolute range filter for the entire field follows. The absolute range filter identifies and removes all the vectors whose displacement was either less than the minimum or more than the maximum specified. The minimum displacement for both horizontal and vertical components of velocity was -12 pixels while the maximum was 12 pixels Using a 5 × 5 neighborhood size the holes were filled recursively with a local mean. Finally a low pass filtering was done using a 3 × 3 neighborhood filter size to smooth the vectors.

The processed velocity vector fields (u and v components) were non-dimensionalised using Tecplot software. The horizontal and vertical displacements were non-dimensionalised using the diameter of the cylinder, D, as x/D and y/D, respectively. The horizontal and vertical components of velocities were non-dimensionalised using the final velocity, U, as u/U and v/U, respectively, while the vorticity, ω, was non-dimensionalised using the diameter, D, and the final velocity, U, as $\omega^* = \omega U/D$. After the velocity fields were non-

dimensionalised, the cylinder was added to the flow field by masking off the region corresponding to the cylinder position. To account for inaccuracies of the vector fields close to the cylinder, an additional one interrogation spot (56 pixels) from the cylinder was also blanked. Then, data files containing the dimensionless parameters were extracted.

Two C++ programs were written to read, calculate, and output in a text file, the required flow features. One was written to calculate the vortex location in both the cross-stream (y) and streamwise (x) directions, the maximum vorticity, ω^*_{max}, and the circulation, Γ, while the other was written to calculate the length of the recirculation zone, L_R, and to extract the velocities long the wake centerline. In order to change the frame of reference (from a moving cylinder to a moving fluid), a freestream velocity was added before calculation of the recirculation zone lengths.

From the tecplot data, the negative vorticity was calculated from the upper half of the recirculation zone, while the positive vorticity from the lower half. The upper rectangular region coordinates, (defined from the left top corner to the bottom right corner of the region) were (0, 1), (2, 0) for the circular cylinder, (0, 1), (2.5, 0) for the square cylinder and (0, 1.2), (2.5, 0) for the diamond cylinder. The lower region coordinates were (0, 0), (2, -1) for the circular cylinder, (0, 0), (2.5, -1) for the square cylinder and (0, 0), (2.5, -1.2) for the diamond cylinder.

The length of the recirculation zone, L_R was obtained by determining the point downstream along the wake centerline where the dimensionless horizontal velocity, $u/U = -1$. This is equivalent to a point of zero horizontal velocity if the flow itself was set to motion. The positions of the vortex centers, on the other hand, were located using the vorticity centroids. The location of the vortex centers in the streamwise direction, a, was determined

by finding the distance of the vorticity centroid from the back of the cylinder while the cross-stream spacing of the vortices, b, was the distance between the two vorticity centroids (Figure 2.3). Other methods of finding the location of the vortex center such as the use of maximum vorticity and the area centroid, gave similar results. The equations for vorticity centroid were:

$$y = \sum[\omega(i,j) * (y(i,j)]/\sum[\omega(i,j)], \tag{3.5a}$$

$$x = \sum[\omega(i,j) * (x(i,j)]/\sum[\omega(i,j)]. \tag{3.5b}$$

By visual evaluation, the minimum dimensionless vorticity that favorably defined the vortices was established to be $\omega^* = +/-2$. The summation of the product of vorticity and the area at the nodes of the grids gave the total circulation of the vortex,

$$\Gamma = \sum[\omega(i,j)] * (dxdy), \tag{3.5c}$$

where $dx = dy$ is the size of the vector spacing.

3.7 Impulsively Started Flow

The study of how a truly impulsive motion is achieved was done using the motion system at different acceleration parameters. Figure 3.6(a) and 3.6(b) shows velocity-time profiles and velocity-distance profiles, respectively, for various acceleration parameters at Re = 500. It is clear that while lower a^* values need a longer duration to reach a uniform velocity, U, higher a^* values take a much shorter duration to achieve the final velocity.

The acceleration phase for a motion at a constant acceleration, as is the case in these experiments, is completed after an elapsed time of $t^* = 1/a^*$, Figure 3.6(a), after which the cylinder will have traveled a distance of $S/D = 1/(2a^*)$, Figure 3.6(b). Therefore, for $a^* = 10$

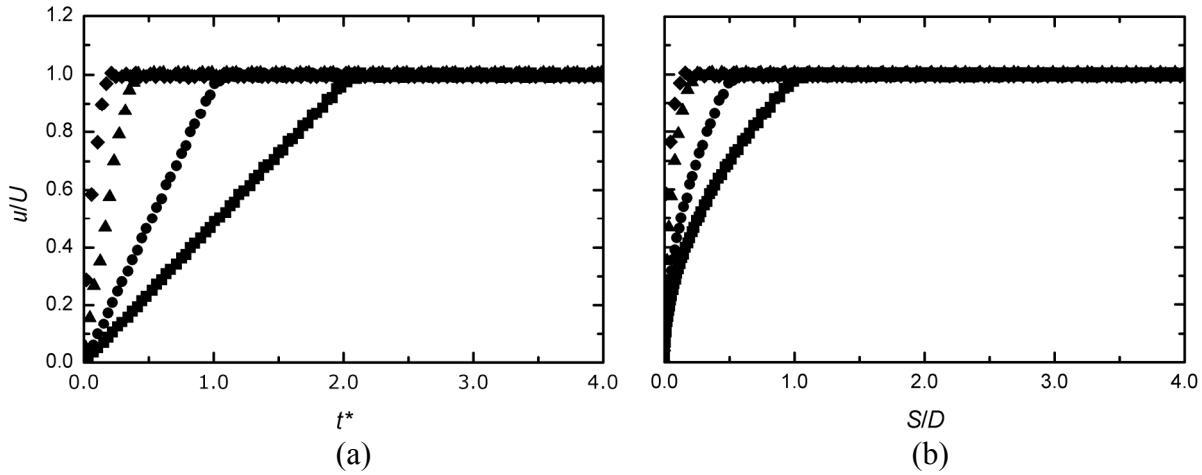

Figure 3.6: The effect of the acceleration parameter on the velocity change of an impulsively started circular cylinder: (a) velocity-time profile; (b) velocity-distance profile; Re = 500; ■, a^* = 0.5; ●, a^* = 1; ▲, a^* = 3; ◆, a^* =10.

for example, at the end of the acceleration phase, the cylinder will have traveled a relative distance, $S/D = 0.05$ after an elapsed time of $t^* = 0.1$.

Based on Sarpkaya's (1991) criterion that for a motion to be regarded as an impulsive start, a^* should be greater than 0.27, all of the cases shown in Figure 3.6 are impulsively started flows. However, it is quite clear that higher acceleration parameters are closer to the 'true' impulsively started motion. In Figures 3.6(a) and 3.6(b), the profiles of $a^* \geq 3$ are almost the same and nearly collapse onto a common curve. Therefore, $a^* = 3$ seems to be the critical acceleration parameter beyond which a^* may have no further effect on the flow development and corresponds to the conditions of an impulsive start.

3.8 Measurement Uncertainty

Measurements in this research are subject to uncertainties that may arise from various sources, including the instrumentation, data acquisition and data processing and analysis. The final error in a measurement, X, is a combination of errors in different measured variables, x_i. The contribution of each variable to the overall error, E, in the result can be expressed as

$$E_X = \left[\sum_i^n \left(\frac{\partial X}{\partial x_i} E_{xi} \right)^2 \right]^{\frac{1}{2}}, \tag{3.6}$$

where E_x is the uncertainty of the result X, $\partial X/\partial x_i$ is the sensitivity of the variable x_i, and E_{xi} is the uncertainty of variable x_i.

The uncertainty in the position of the cylinder (given by the motion system) is equivalent to one encoder count (0.00375 mm). Therefore, the uncertainty in x/D and y/D is negligibly small (0.000125). The velocity of the cylinder, U, is calculated from the motion system data − the distance moved by the cylinder and the time. Therefore, the error associated with this variable is also very small. The cylinder has been machined with precision; hence the uncertainty in the diameter of the cylinder is also negligible. Since the acceleration, a, is calculated from U and D, the uncertainty in the acceleration, and acceleration parameter, a*, are also negligible.

The length of the recirculation zone of the cylinder, L_R/D, is calculated from the PIV measurements by determining the location of the stagnation point inside the recirculation zone, along the wake centerline. The point is located at the 'nodes' of the grids generated by the vectors. Therefore, the uncertainty in the measurements is equivalent to the size of the vector spacing, 0.054D (for the Insight 5 data). The streamwise position of the vortices and the cross-stream spacing of the spacing are also calculated at the nodes of the grids. Hence, the error also is 0.054D (equivalent to the vector spacing).

The measurement uncertainty of the velocity components, u and v, is estimated from the PIV images. Since the towing velocity of the cylinder, U, is known from the motion system, it is expected that the cylinder's velocity in the horizontal axis should be the same as U once the acceleration phase is over. This information can be used to estimate the

Table 3.2: The instantaneous velocity, *u*, of the cylinder at *t* * = 3 at various Re (*U* is the cylinder velocity from the motion system).

Re	CYLINDER	*U* [mm/s]	*u* [mm/s]	error	% error
200	CC	7.65	8.24	0.59	8%
	SC	7.80	8.18	0.38	5%
500	SC	19.70	18.69	-1.01	-5%
	DC	19.70	18.14	-1.56	-8%
1000	CC	39.97	41.16	1.19	3%
	SC	40.17	40.60	0.43	1%
	DC	38.92	39.67	0.75	2%

uncertainty in velocity. Table 3.2 shows the velocity of the cylinder at various times and Reynolds numbers. The uncertainty in the measurements of *u* and *v* is less than 10%.

The uncertainty in the dimensionless vorticity, ω^*, is estimated to be ±1. This is equivalent to the intervals between the vorticity contours.

The temperature was measured using a digital instrument (DORIC) (to one decimal place) and therefore the uncertainty was 0.1°C. The density of the water was determined from the following correlation (White, 1999),

$$\rho = 1000 - 0.0178(T-4)^{1.7}, \tag{3.7}$$

where T is in °C. The uncertainty of the density is then determined as follows, where the error in the correlation itself (Equation (3.7)) is 0.02% (White, 1999):

$$E_\rho = \left[\left(\frac{\partial \rho}{\partial T} E_T\right)^2 + \left(E_{corr}\right)^2\right]^{\frac{1}{2}} \tag{3.8}$$

$$E_\rho = \left[-0.03026\left((T-4)^{0.7}\right)^2 + \left(0.0002\rho\right)^2\right]^{\frac{1}{2}} \tag{3.9}$$

The viscosity is then determined using the expression below (White, 1999).

$$\mu = 0.001788\left(e^{\left(-1.704 - 5.306\left(\frac{273.16}{T} \right) + 7.003\left(\frac{273.16}{T} \right)^2 \right)} \right) \tag{3.10}$$

The uncertainty of the viscosity was then calculated as

$$E_\mu = \left[\left(\frac{\partial \mu}{\partial T} E_T \right)^2 + \left(E_{corr} \right)^2 \right]^{\frac{1}{2}}. \tag{3.11}$$

The uncertainty in the correlation (equation (3.10)) was not given by White (1999) and therefore was neglected.

Having determined all the uncertainties associated with other variables the uncertainty of the Reynolds number was then calculated. The Reynolds number was defined using the diameter of the cylinder, *D*, or using one side of the square or diamond cylinder as

$$\mathrm{Re} = \frac{\rho U D}{\mu}. \tag{3.12}$$

The uncertainty of Re was determined as

$$E_{\mathrm{Re}} = \left[\left(\frac{\partial \mathrm{Re}}{\partial \rho} E_\rho \right)^2 + \left(\frac{\partial \mathrm{Re}}{\partial U} E_U \right)^2 + \left(\frac{\partial \mathrm{Re}}{\partial D} E_D \right)^2 + \left(\frac{\partial \mathrm{Re}}{\partial \mu} \right)^2 \right]^{\frac{1}{2}}. \tag{3.13}$$

Since the uncertainty in both *D* and *U* are negligible, the uncertainty in Re was basically as a result of the uncertainty in viscosity and density, as follows.

$$E_{\mathrm{Re}} = \left[\left(\frac{UD}{\mu} E_\rho \right)^2 + \left(\frac{-\rho U D}{\mu^2} E_\mu \right)^2 \right]^{\frac{1}{2}} \tag{3.14}$$

Table 3.3 presents a summary of all the variables used in the research and the uncertainties in each variable.

Table 3.3: Variables in this research together with the uncertainty of each variable. The typical values presented are based on the circular cylinder, at Re = 500, t^* = 3.

VARIABLE	TYPICAL VALUE	UNCERTAINTY	%
Circulation, Γ^*	4.00	± 0.054	1%
Cylinder diameter, D	0.00254 m	± 0.000	0%
Cross-stream spacing of the primary eddies, b/D	0.70	± 0.054	5%
Freestream velocity, U	0.01951 m/s	± 0.000	0%
Length of the recirculation zone, L_R/D	1.25	± 0.054	4%
Reynolds number, Re	200	± 0.625	0%
	500	± 1.564	0%
	1000	± 3.128	0%
Streamwise location of the primary eddies, a/D	0.5000	± 0.054	11%
Temperature, T	21^0 C	± 0.1000	0%
Horizontal velocity components, u	0.0185 m/s	± 0.0098	5%
Viscosity, μ	0.0001 Ns/m^2	± 2.4038E-06	0%
Maximum vorticity, ω^*_{max}	15.00	± 1.000	7%
Water Density, ρ	997.80	± 1.996	0%
x/D and y/D	0.00	± 0.000	0%

CHAPTER FOUR

CIRCULAR CYLINDER RESULTS AND DISCUSSION

4.1 Introduction

In this chapter, the results for the impulsively started circular cylinder are presented. The development of the recirculation zone in time is examined by looking at the features used to quantify the zone, i.e. the length of the zone, the streamwise location of the primary eddies, the cross-stream spacing of the primary eddies, the maximum vorticity and the circulation. Each feature is examined first for Re = 500 and then, comparatively, for Re = 200 and 1000. The results for three runs of the experiments done at every a^* and Re are presented at a typical time interval, $t^* = 0.2$.

4.2 Velocity Fields

Figure 4.2 shows a PIV image of a moving circular cylinder (shown schematically in Figure 4.1), at an instant, as captured by the camera. The uniformly distributed bright spots in the image are the tracer particles, which form the basis for the analysis of the image. Only the wake of the cylinder is visible.

The images are processed to produce the instantaneous velocity and vorticity fields at various time intervals. Clearly shown in Figures 4.3 and 4.4 are the velocity and vorticity fields near the cylinder at various Re and t^* and the way they change with an increase in time elapsed from the start of motion. It is from these velocity fields that other parameters of

interest, including the length of the recirculation zone, the streamwise and cross-stream locations of the vortices, the circulation and the maximum vorticity, are calculated.

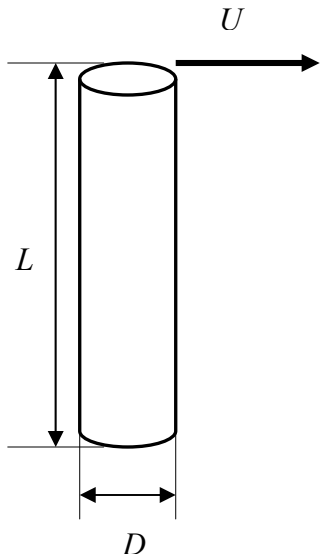

Figure 4.1: Schematic drawing of the circular cylinder of diameter, *D*, and length, *L* in an impulsively started motion. The cylinder is towed from left to right with a velocity, *U*.

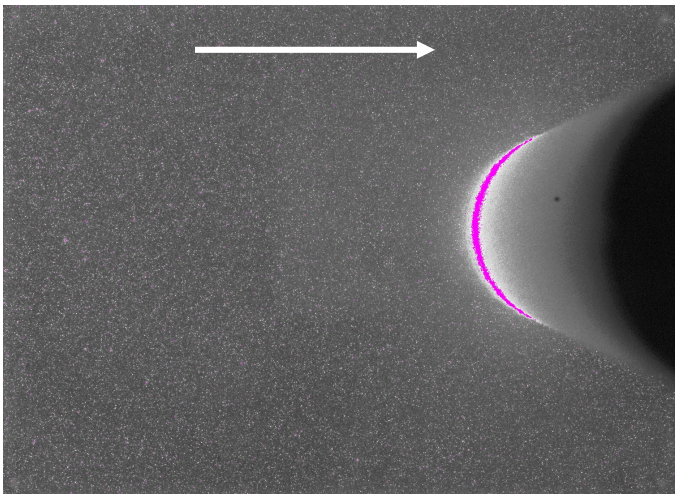

Figure 4.2: An image of a moving circular cylinder. The cylinder is moving from left to right and the laser light sheet is shone from the left of the picture.

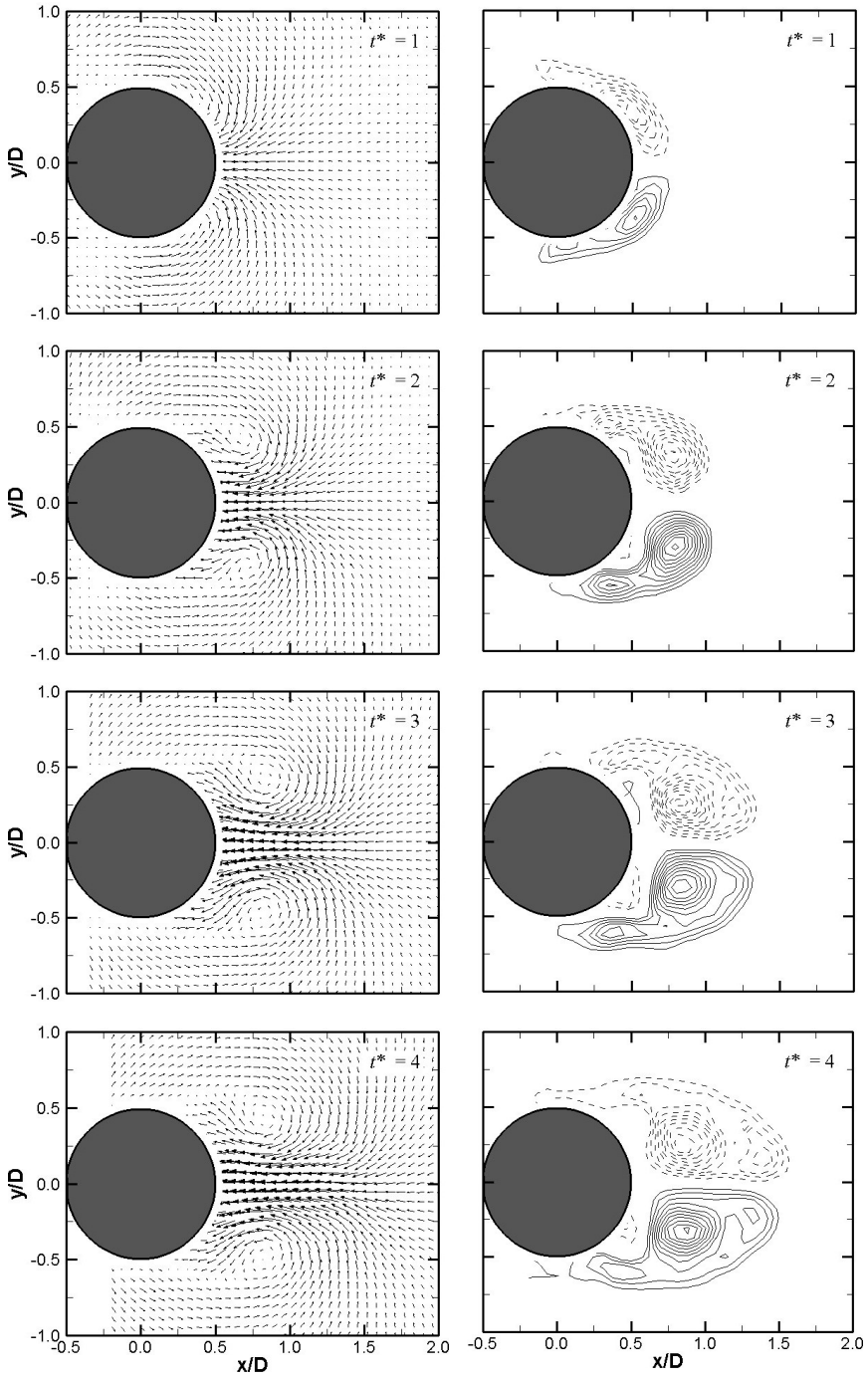

(a) (b)

Figure 4.3: An impulsively started circular cylinder at Re = 1000, $a^* = 5$: (a) instantaneous velocity fields and (b) corresponding instantaneous vorticity fields. The cylinder is towed from right to left. Dashed lines represent negative vorticity (CW), solid lines represent positive vorticity (CCW), the minimum dimensionless vorticity contour is $|\omega^*| = 2$ and the contour interval is $\Delta\omega^* = 1$.

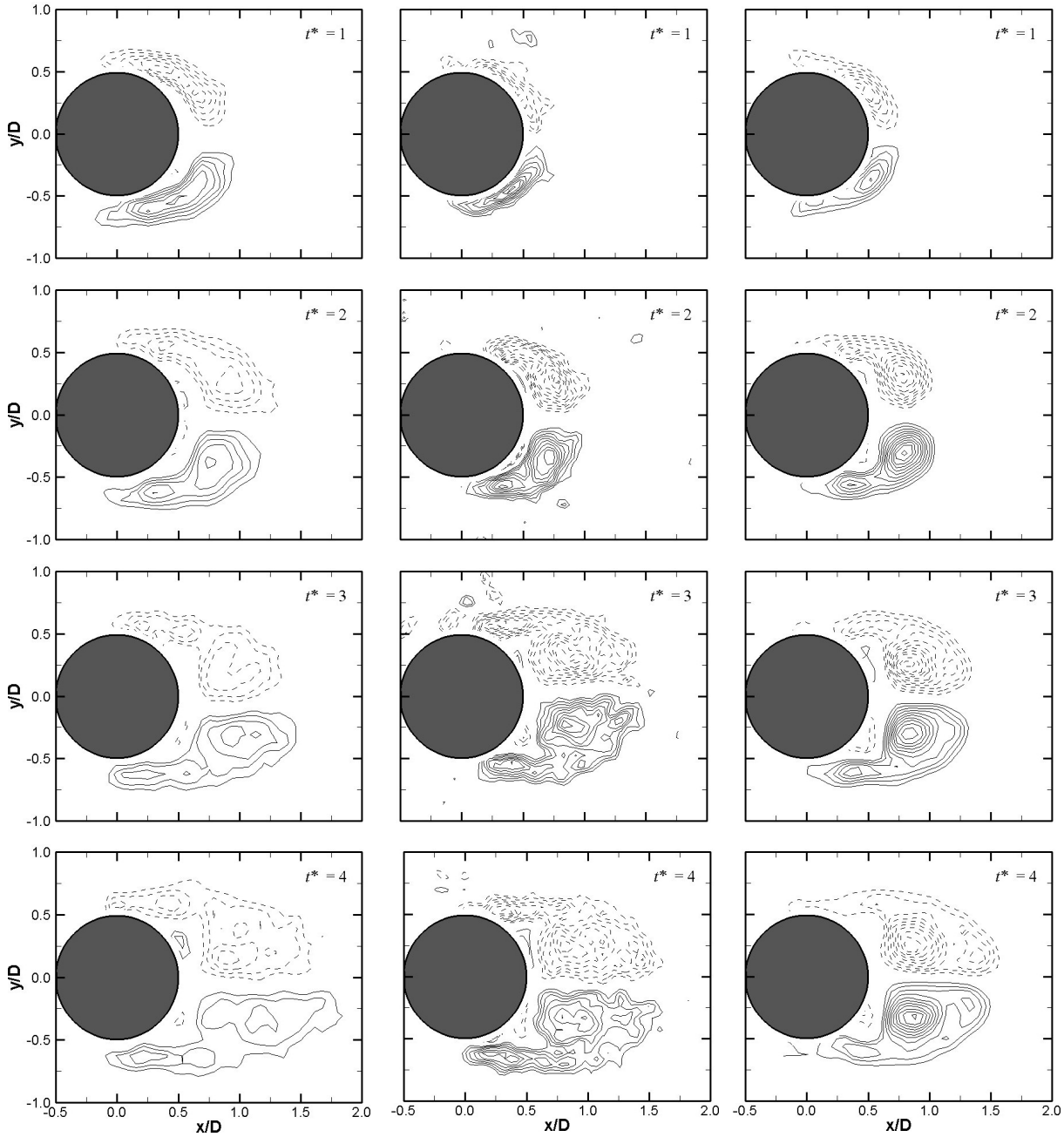

Figure 4.4: A comparison of the vorticity contours for an impulsively started circular cylinder at (a) Re = 200, $a^* = 10$, (b) Re = 500, $a^* = 10$ and (c) Re = 1000, $a^* = 5$, for $t^* = 1$, 2, 3 and 4. The cylinder is towed from right to left. Dashed lines represent negative vorticity (CW), solid lines represent positive vorticity (CCW), the minimum vorticity contour is $|\omega^*| = 2$ and the contour interval is $\Delta\omega^* = 1$.

4.3 Length of the Recirculation Zone

The length of the recirculation zone of an impulsively started circular cylinder increases with time regardless of the acceleration parameter. Figure 4.5(a) shows the length of the recirculation zone plotted against the elapsed time for Re = 500 for various acceleration parameters. The results show that L_R increases as a^* increases. At any given time, L_R for a lower value of a^*, e.g. $a^* = 0.5$, is relatively shorter compared with a higher value of a^* e.g. $a^* = 10$. The influence of a^* on the length of the recirculation zone ceases when $a^* \geq 3$, at which point the L_R/D data collapse to a single curve. This corresponds to the onset of a 'true' impulsive start based on the velocity-time profiles seen in Figure 3.5(a).

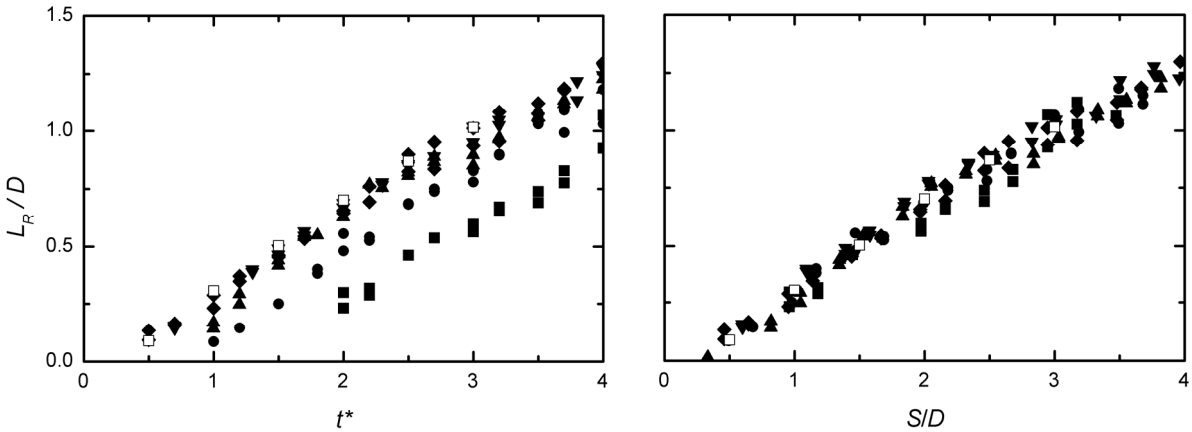

Figure 4.5: Variation of the recirculation zone length (a) with time and (b) with the distance moved, for an impulsively started circular cylinder, Re = 500. ■, $a^* = 0.5$; ●, $a^* = 1$; ▲, $a^* = 3$; ▼, $a^* = 5$; ◆, $a^* = 10$; □, Bouard and Coutanceau (1980), Re = 550.

The L_R/D data for $a^* \geq 3$ agree very well with the published results of Bouard and Coutanceau (1980). (These authors did not specify their acceleration parameter, but it is estimated to be $a^* \approx 50$). For the acceleration parameters studied, there is minimal recirculation zone length at the early stages of motion, since the flow is initially irrotational.

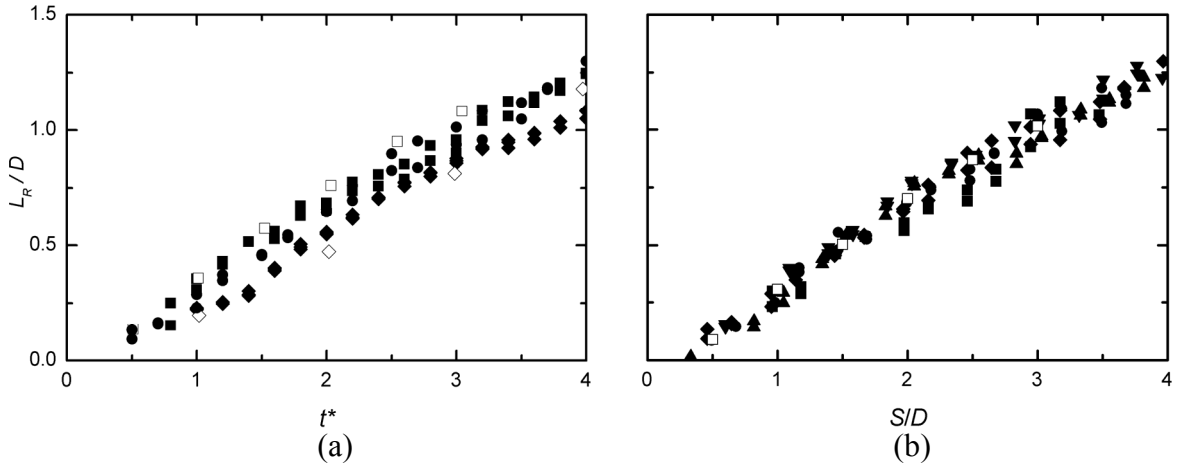

Figure 4.6: Variation of the recirculation zone length (a) with time and (b) with the distance moved, for an impulsively started circular cylinder, ■, a^* = 10, Re = 200; ●, a^* = 10, Re = 500; ◆, a^* = 5, Re = 1000; □, Bouard and Coutanceau (1980), Re = 200; , ◇, Ta Phuoc Loc (1980), Re = 1000.

Then, as more time elapses after the start of motion, the symmetrical vortices formed continue to grow in size and so does L_R.

Figure 4.5(b) shows the length of the recirculation zone plotted against the distance moved by the cylinder. All the data are seen to collapse to a single common curve, an indication the length of the recirculation zone is more dependent on the distance moved by the circular cylinder following the start of motion. This also is a confirmation that all the a^* examined are impulsively started based on the velocity-distance moved profiles, as was proposed by Sarpkaya (1991).

Figures 4.6(a) and 4.6(b) shows the L_R for the impulsively started circular cylinder at Re = 200 and 1000, plotted against time and distanced moved, respectively. Also shown on the graphs are the results for Re = 500, a^* = 10. The results show that the length of the recirculation zone is also somewhat dependent on the Reynolds number. Although the scope of the study is limited (by the research facility) to Re = 200 to 1000, it can be seen that there is a notable trend. At any given t^*, the L_R for Re = 200 is higher than those of Re = 500 and

1000. The L_R data for Re = 200 compare very well with the results for Bouard and Coutanceau (1980) while that of Re = 1000 matches the numerical data of Ta Phuoc Loc (1980). The L_R data for various Re collapse almost onto a common curve when plotted against the distance moved by the cylinder following an impulsive start (Figure 4.6(b)). These results are in agreement with the results of Honji and Taneda (1969) who observed a similar collapse for L_R for impulsively started cylinder at various Reynolds numbers.

4.4 Streamwise Location of the Primary Eddies

The streamwise location of the symmetrical vortices in the streamwise direction, *a,* is the distance from the back of the cylinder to the vorticity centroid in the recirculation zone in the streamwise direction. As the primary eddies grow with the elapsed time following an impulsive start, the centers of the primary eddies move farther away from the base of the cylinder. Figure 4.7(a) shows the variation of a/D with time for Re = 500 for various acceleration parameters examined. For all the a^*, a/D increases almost linearly with t^*. The a/D values for low a^* are lower than those of higher a^* indicating that at any given t^*, the primary eddies are located closer to the base of the cylinder at lower values of a^*. The a/D data for $a^* \geq 3$ (corresponding to a near true impulsive start) compare favorably with the results of Bouard and Coutanceau (1980).

Again, all the curves collapses onto a common curve when the results are plotted against the distance moved, S/D, as shown in Figure 4.7(b). The maximum value of a/D reached, before the onset of asymmetry at $t^* \approx 4$, in an impulsively started flow is about $0.6D$ which is almost half the length of the recirculation zone (it is about $1.2D$) reached at the same time.

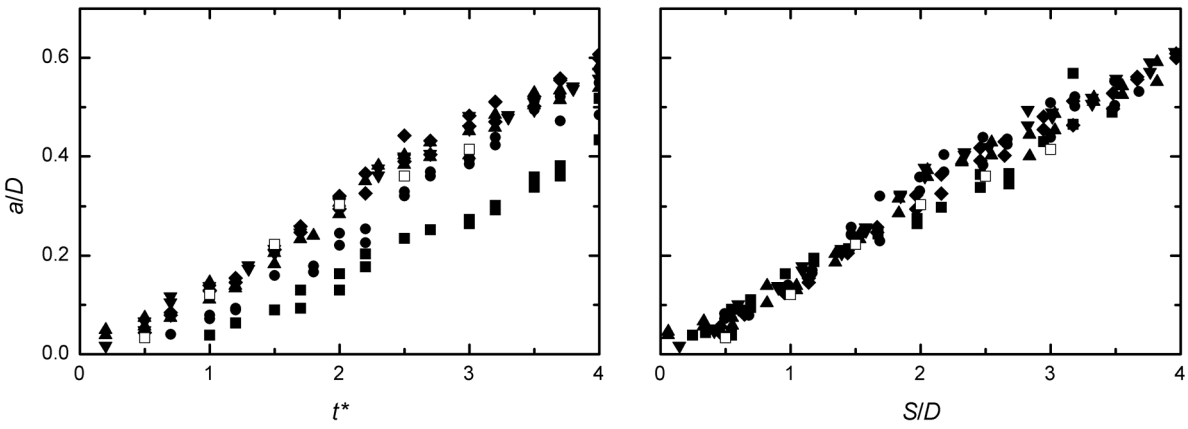

(a) (b)

Figure 4.7: Variation of the streamwise vortex location, (a) with time and (b) with the distance moved, for an impulsively started circular cylinder, Re = 500. ■, a^* = 0.5; ●, a^* = 1; ▲, a^* = 3; ▼, a^* = 5; ◆, a^* = 10; □, Bouard and Coutanceau (1980), Re = 550.

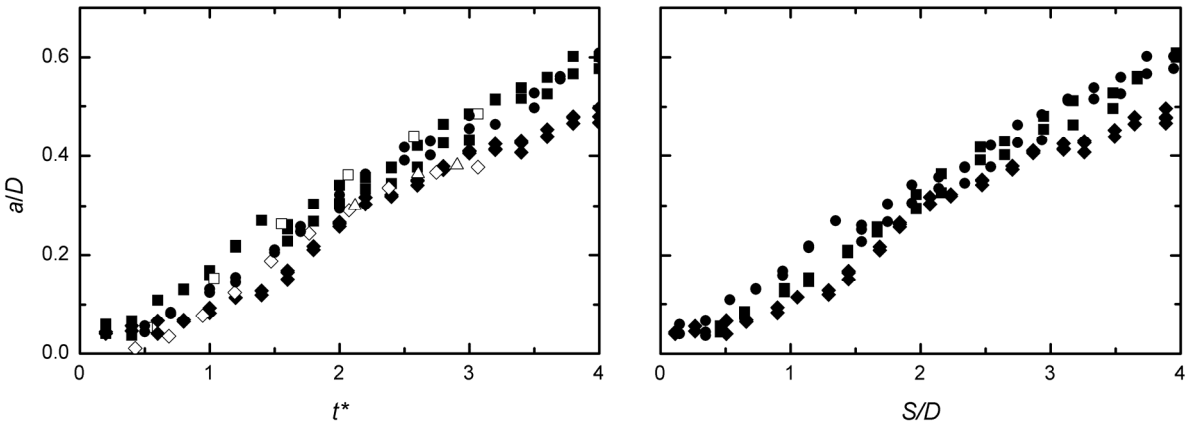

(a) (b)

Figure 4.8: Variation of the steamwise position of the vortices (a) with time and (b) with the distance moved, for an impulsively started circular cylinder, ■, a^* = 10, Re = 200; ●, a^* = 10, Re = 500; ◆, a^* = 5, Re = 1000; □, Bouard and Coutanceau, Re = 200; ∆, Chu and Liao (1992), Re = 1000; ◇, Wu and Chu (1989), Re = 1000.

The streamwise position of the vortices is also dependent on Re. Figure 4.8(a) shows the variation of the a/D with t^* for different Re. Observations similar to that of L_R can be made, that at any given t^*, the streamwise location of the vortex centers for a lower Re is higher than that of a higher Re. The results for Re = 200 are in good agreement with the

results of Bouard and Coutanceau (1980) while those for Re = 1000 agree very well with the results of Wu and Chu (1989) and Chu and Liao (1992).

When plotted against the distance moved, Figure 4.8(b), the results also collapse to common curve. This is an indication that the streamwise location of the primary eddies is independent on Re.

4.5 Cross-Stream Spacing of the Primary Eddies

Figure 4.9(a) shows the cross-stream (transverse) spacing of the centers of the primary eddies, which is the spacing between the vorticity centroids of the two eddies. It can be seen that the spacing is relatively independent of both a^* and t^*. A closer look at the behavior of b/D shows that it undergoes a slight increase from $t^* = 0$ to 2. This is attributed to the variation of the separation angles which takes place at the start of the impulsive motion. Sarpkaya (1992) observed that at the start of an impulsive motion the separation points move from the rear stagnation point before eventually settling at a constant angle which is close to the laminar separation angle. Earlier, using numerical calculations for Re = 1000 to 3000, Chang and Chern (1991) had noted that indeed the separation angles around an impulsively started circular cylinder vary in the first two time intervals. According to their calculations, the separation angle for Re = 1000 settles at a near constant value of $\theta = 120^0$ (where θ is the angle measured from the upstream stagnation point) after $t^* \approx 2$.

In Figure 4.9(b), the cross-stream spacing of the vortices is plotted against the distanced moved by the cylinder following the impulsive start. These results, just like those of L_R and a/D, collapse onto one common curve. It is notable, however, that the results are relatively higher than those Bouard and Coutanceau (1980), possibly due to the method of calculation used (vorticity centroid).

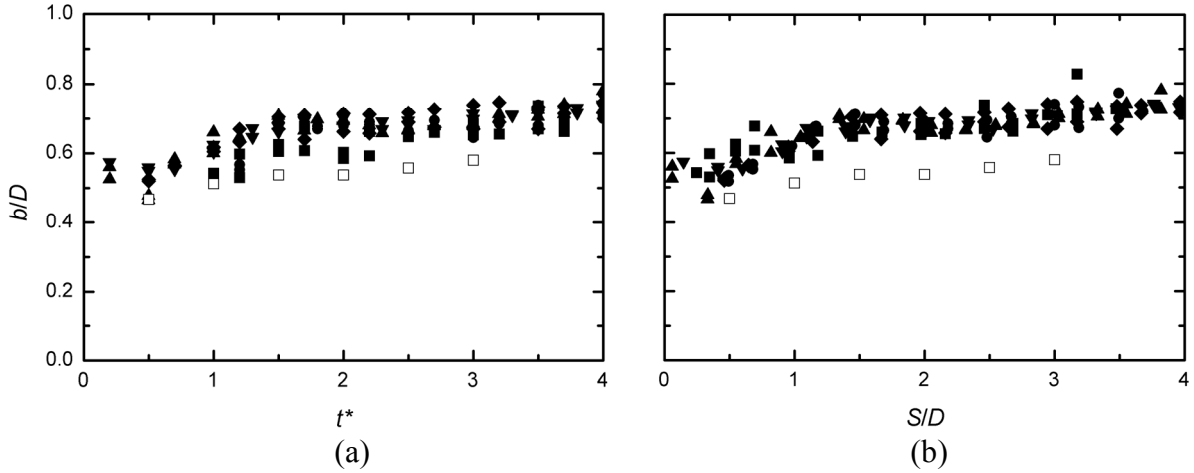

Figure 4.9: Variation of the cross-stream spacing of the vortices (a) with time and (b) with the distance moved, for an impulsively started circular cylinder, Re = 500. ■, a^* = 0.5; ●, a^* = 1; ▲, a^* = 3; ▼, a^* = 5; ◆, a^* =10; □, Bouard and Coutanceau (1980), Re = 550.

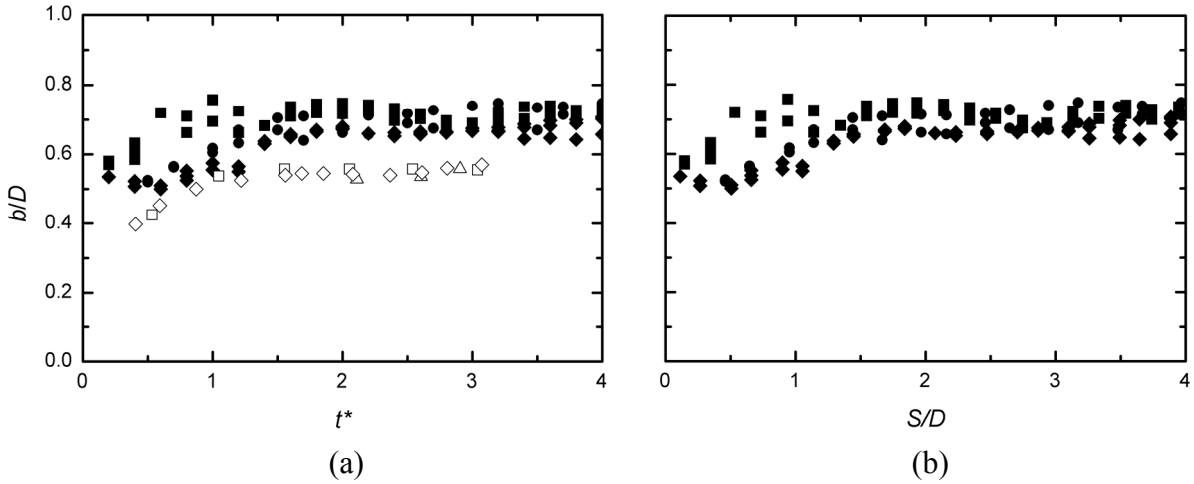

Figure 4.10: The cross-stream spacing of the primary eddies (a) with time and (b) with the distance moved, for an impulsively started circular cylinder, ■, a^* = 10, Re = 200; ●, a^* = 10, Re = 500; ◆, a^* = 5, Re = 1000; □, Bouard and Coutanceau (1980), Re = 200; ∆, Chu and Liao (1992), Re = 1000; ◇, Wu and Chu (1989), Re = 1000

The cross-stream spacing of the centers of primary eddies does not depend on the value of the Reynolds number. Figures 4.10(a) and (b) show the b/D data for Re = 200, 500 and 1000 plotted against t^* and S/D, respectively. The results for all the Reynolds numbers examined are scattered around the same value, $b/D \approx 0.7D$. Although the data from the

literature are relatively lower, they follow the same trend and are seen to form a single curve irrespective of the Re.

4.6 Circulation of the Primary Vortices

The circulation (strength), $\Gamma^* = \Gamma/UD$, of the primary eddy increases with the elapsed time from the start of an impulsive motion because of the continued supply of the vorticity from the separated boundary layer. Figure 4.11(a) shows that for all the a^* examined, the strength of the primary eddies increases almost linearly with t^*. While the Γ^* data for smaller values of a^* are relatively lower, the circulation for $a^* \geq 3$, corresponding to the near true impulsively started motion, converge onto a single curve and agree very well with the published data of Chu and Liao (1992). The collapse of the data for $a^* \geq 3$ is consistent with the behavior of the length of the recirculation zone, Figure 4.5(a), and the streamwise location of the vortex centers, Figure 4.7(a). A similar collapse of the data with a^* is reported by Jeon and Gharib (2004) when they non-dimensionalised their circulation data with the strength of the first shed vortex.

Figure 4.11(b) shows the circulation data plotted against the distance moved by the cylinder. It can be seen that all the data collapse onto a single curve. This behavior is also consistent with the behavior of the length of the recirculation zone, the streamwise location of the vortices and the cross-stream spacing of the vortices.

The effect of Re on the strength of the primary eddies is shown in Figures 4.12(a) and 4.12(b). For $t^* < 1$, the circulation for Re = 200 is higher than those of Re = 500 and 1000. However, after $t^* = 1$, the circulation within the vortex for Re = 200 begins to level off in similar manner as the maximum vorticity (Figure 4.13(a)). Chu and Liao (1992) observed that the circulation strength of the impulsively started circular cylinder reaches an asymptote

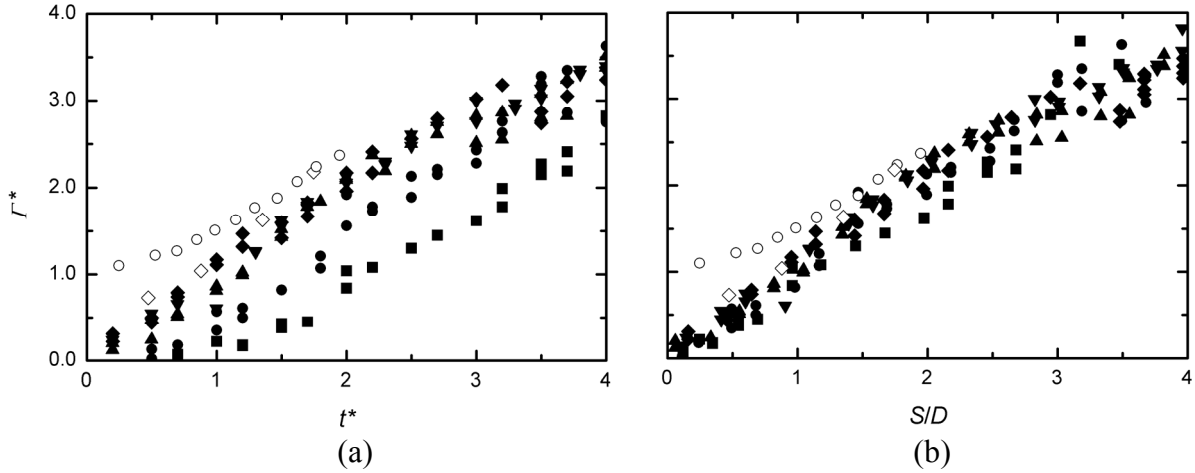

(a) (b)

Figure 4.11: The variation in strength (circulation) of the primary eddies (a) with time and (b) with the distance moved, for an impulsively started circular cylinder, Re = 500. ■, $a^* = 0.5$; ●, $a^* = 1$; ▲, $a^* = 3$; ▼, $a^* = 5$; ◆, $a^* = 10$; ◊, Chu and Liao (1992), Re = 500; ○, Nagata *et al.* (1989), Re = 550.

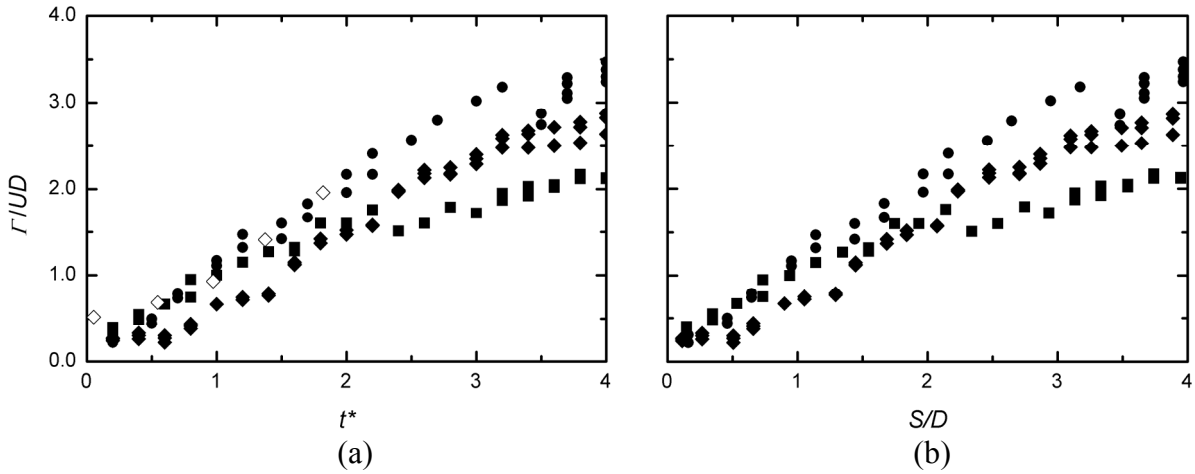

(a) (b)

Figure 4.12: The change of strength (circulation) of the primary eddies (a) with time and (b) with the distance moved, for an impulsively started circular cylinder, ■, $a^* = 10$, Re = 200; ●, $a^* = 10$, Re = 500; ◆, $a^* = 5$, Re = 1000; ◊, Chu and Liao (1992), Re = 1000.

after $t^* > 2$, for Re = 3000, and further noted that for all the Re, the circulation has to reach an asymptotic value before the occurrence of vortex shedding

4.7 Maximum Vorticity within the Primary Vortex

The maximum vorticity-time profile for an impulsively started circular cylinder has characteristics similar to the velocity-time profile (Figure 3.6). The profile is characterized by a region of steady rise (similar to acceleration phase), a peak and a final steady value. The peak maximum vorticity is reached at a time shortly after the end of the cylinder's acceleration phase. Figure 4.13(a) shows that although the maximum vorticity values for different a^* values are different at the start of the motion, they converge to a common curve once the peak value has been attained.

Figure 4.13(b) shows the maximum vorticity within the primary vortex plotted against the distance moved by the cylinder from the start of the motion. The results merge onto a common curve and level off after reaching the peak value.

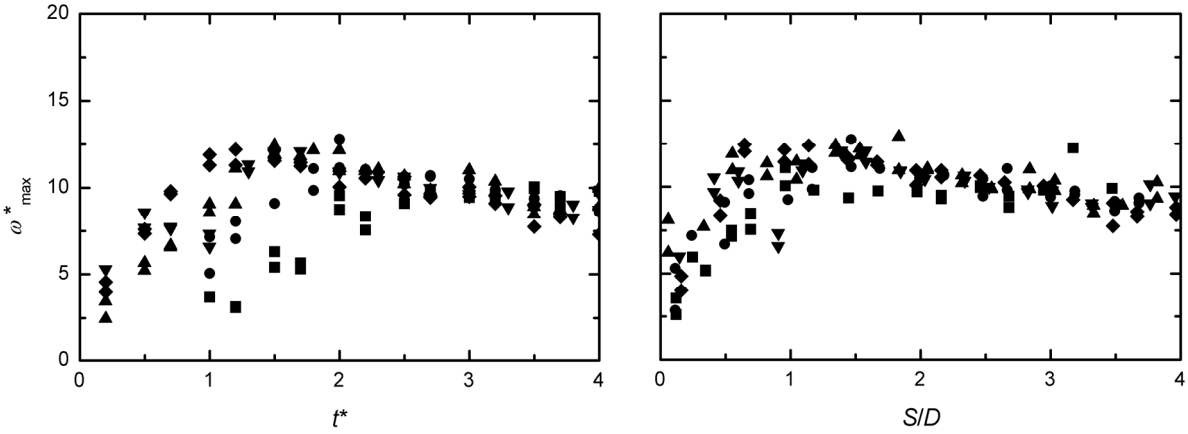

Figure 4.13: The variation of the maximum vorticity within the primary eddies (a) with time and (b) with the distance moved, for an impulsively started circular cylinder, Re = 500. ■, a^* = 0.5; ●, a^* = 1; ▲, a^* = 3; ▼, a^* = 5; ◆, a^* = 10.

The graphs for the maximum vorticity for Re = 200, 500 and 1000 follow distinct profiles, as shown in Figures 4.14(a) and 4.14(b). The profiles for Re = 200 and Re = 500 follow the same trend since they have the same a^*. However, that of Re = 200 reaches its

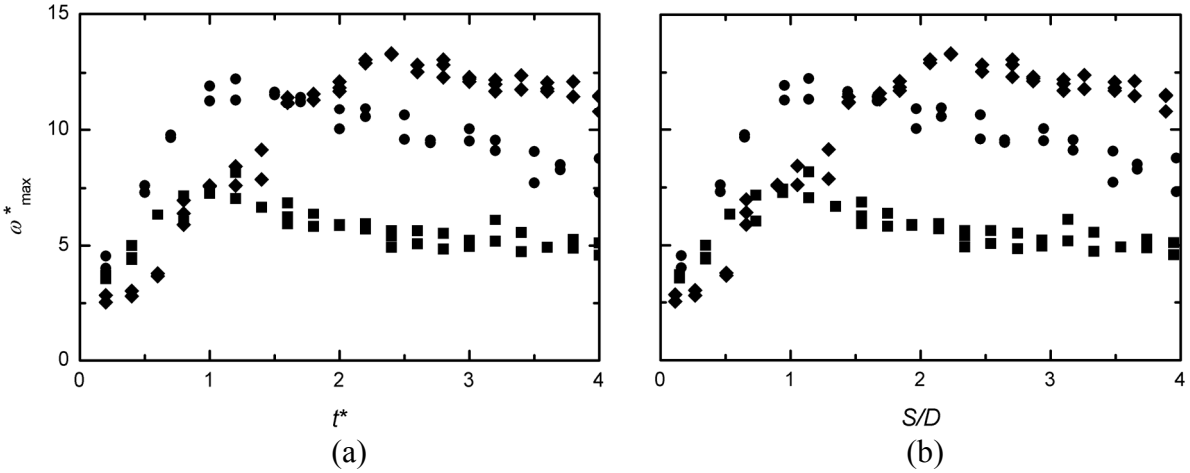

Figure 4.14: The maximum vorticity within the primary eddies, plotted against (a) time and (b) the distance moved, for an impulsively started circular cylinder, ■, a^* = 10, Re = 200; ●, a^* = 10, Re = 500; ◆, a^* = 5, Re = 1000.

peak value sooner and starts to level off. Once the peak value has been reached, the results for Re = 1000 are higher than those of both Re = 500 and 200. This may be an indication that the maximum vorticity depends on Re and indeed the final maximum vorticity within a primary vortex increases as the Re increases.

4.8 Velocities along the Wake Centerline

Figure 4.15 shows a typical distribution of the streamwise velocity along the wake centerline of an impulsively started circular cylinder. The data for $a^* \geq 3$ are in good agreement with the published data of Bouard and Coutanceau (1980), indicating that this range of the acceleration parameters corresponds to conditions of an impulsive start. For this range of a^*, a maximum negative velocity almost equal to the freestream velocity, U, is reached, unlike for lower a^* which has hardly any negative velocity range.

The effect of Re on the streamwise wake centerline velocity is shown Figure 4.16. These results are consistent with the earlier results of the length of the recirculation since the point at which the velocity is zero indicates the end of the recirculation zone. The curve for

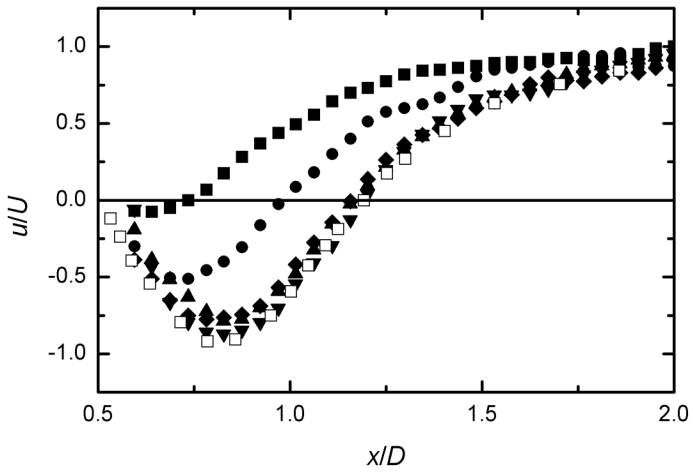

Figure 4.15: The distribution of the streamwise velocity along the wake centerline of an impulsively started circular cylinder at $t^* = 2$, Re = 500. ■, $a^* = 0.5$; ●, $a^* = 1$; ▲, $a^* = 3$; ▼, $a^* = 5$; ◆, $a^* = 10$; □, Bouard and Coutanceau (1980), Re = 550.

Re = 200 agrees very well in magnitude and shape with the data available in the literature. The maximum negative velocity reached at the wake centerline is about $0.8U$. According to Bouard and Coutanceau (1980), the presence of these large negative velocities at the wake of the cylinder leads to the appearance of the secondary features such as the bulge phenomenon which is seen to occur at $t^* > 2$.

At a particular point in the distance moved by the cylinder following the start of motion, the velocity profiles along the wake centerline for all acceleration parameters almost collapse onto a common curve (Figure 4.17). This is consistent with the collapse of L_R (Figure 4.5(b)), a/D (Figure 4.7(b)), and Γ^* (Figure 4.11(b)) when plotted against the distance moved by the cylinder. It means that the growth of the recirculation zone is more dependent on the distance moved than the mode of acceleration.

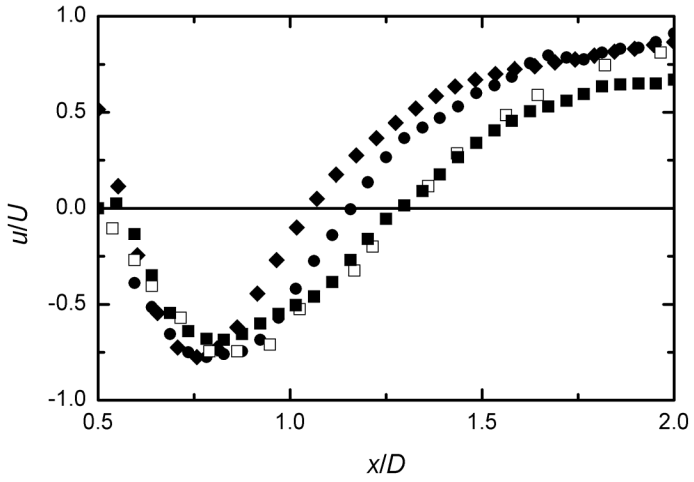

Figure 4.16: The distribution of the streamwise velocity along the wake centerline of an impulsively started circular cylinder at $t^* = 2$; ■, $a^* = 10$, Re = 200; ●, $a^* = 10$, Re = 500; ◆, $a^* = 5$, Re = 1000; □, Bouard and Coutanceau (1980), Re = 200.

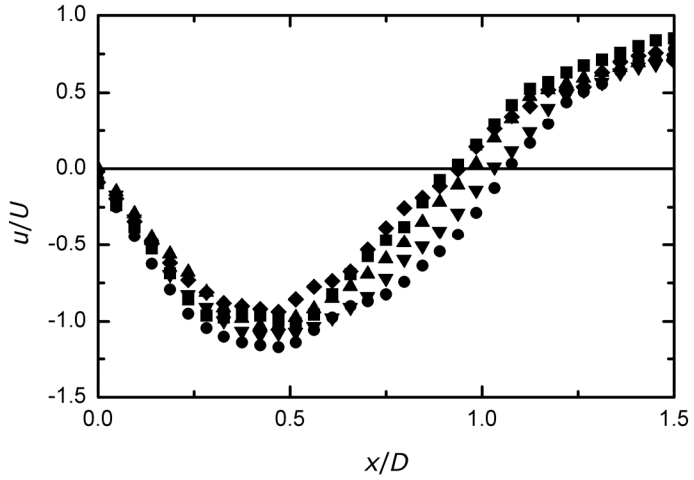

Figure 4.17: The velocity along the wake centerline at Re = 500 after the cylinder has moved a distance of $S/D = 3$ following the start of motion; ■, $a^* = 0.5$ ($t^* = 4$); ●, $a^* = 1$ ($t^* = 3.5$); ▲, $a^* = 3$ ($t^* = 3.2$); ▼, $a^* = 5$ (t* = 3.2); ◆, $a^* = 10$ ($t^* = 3$).

CHAPTER FIVE

SQUARE CYLINDER RESULTS AND DISCUSSION

5.1 Introduction

Results for the impulsively started square cylinder are presented in this Chapter. The development of the recirculation zone in time is also examined by looking at the features used to quantify the zone, i.e. the length of the zone, the streamwise location of the primary eddies, the cross-stream spacing of the primary eddies, the maximum vorticity and the circulation of the zone. Each feature is examined first for Re = 500 and then, comparatively, for Re = 200 and 1000.

5.2 Velocity Fields

Figure 5.1 shows a PIV image of a square cylinder as captured by the camera at some instant during motion. The cylinder is moving from left to right and the laser light sheet is casted from left making only the wake and the back of the cylinder visible. The tracer particles appear as bright spots in the image while the visible side appearing as a bright line forms the reference frame for determining the spatial position of the cylinder. The images are processed using the procedure described in Section 3.6 to obtain the velocity and vorticity fields.

Figure 5.2 shows the instantaneous velocity and vorticity fields for an impulsively started square cylinder at Re = 500 while Figure 5.3 shows, comparatively, the instantaneous vorticity fields for an impulsively started square cylinder at Re = 200, 500 and 1000. The

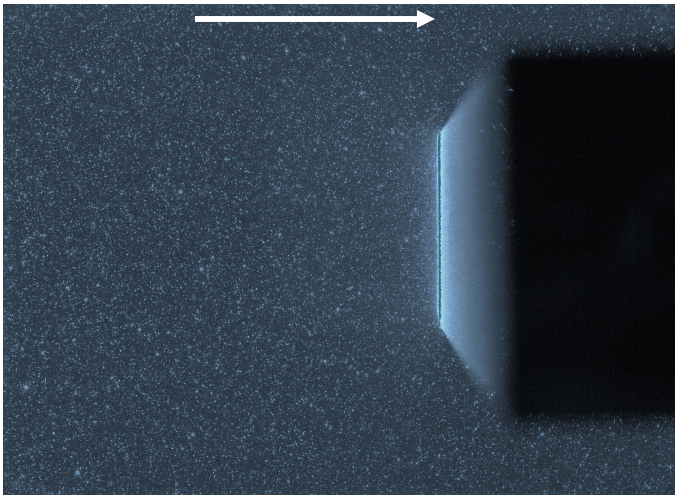

Figure 5.1: An image of the square cylinder in motion captured by the camera at some point after the start of the impulsive motion. The cylinder is moving from left to right and the laser light sheet is shone from the left.

diagrams depict the development of the recirculation zone with time up to $t^* = 4$ (the vortex shedding regime is not reached). From the velocity field diagrams, the time development of the flow at Re = 200 are similar to the photographic presentation made by Finaish (1991). The secondary vorticity can be seen to start forming at Re = 500 and 1000 at $t^* \geq 2$. This secondary vorticity did not appear in the numerical simulations of Lee *et al.* (1996), as shown earlier in Figure 2.5.

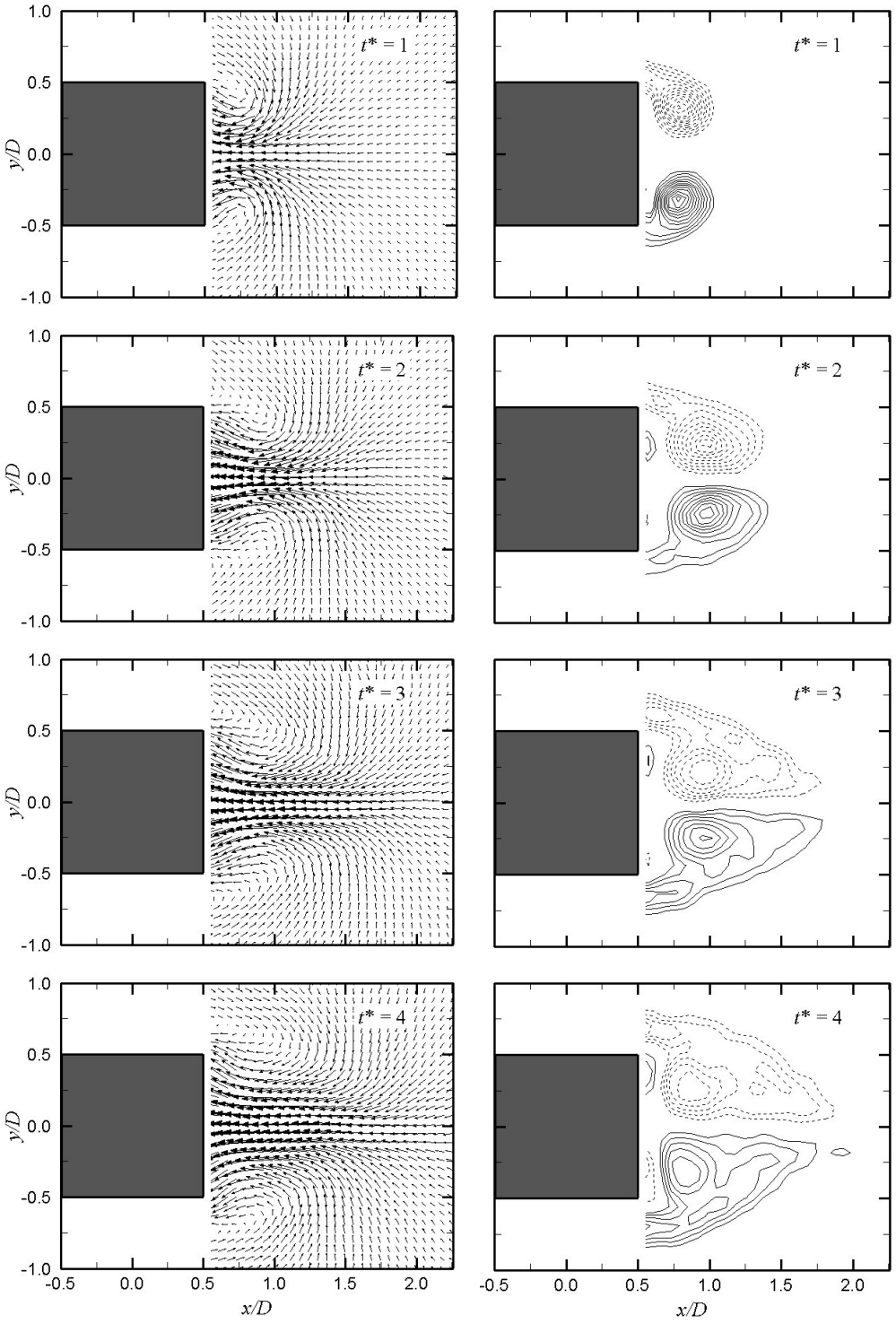

Figure 5.2: The instantaneous (a) velocity and (b) vorticity fields diagrams of an impulsively started square cylinder at Re = 500, $a^* = 5$. The dashed lines represent negative vorticity while the solid lines represent positive vorticity. The minimum vorticity contour is $|\omega^*| = 2$ and the interval between contours is $\Delta\omega^* = 1$.

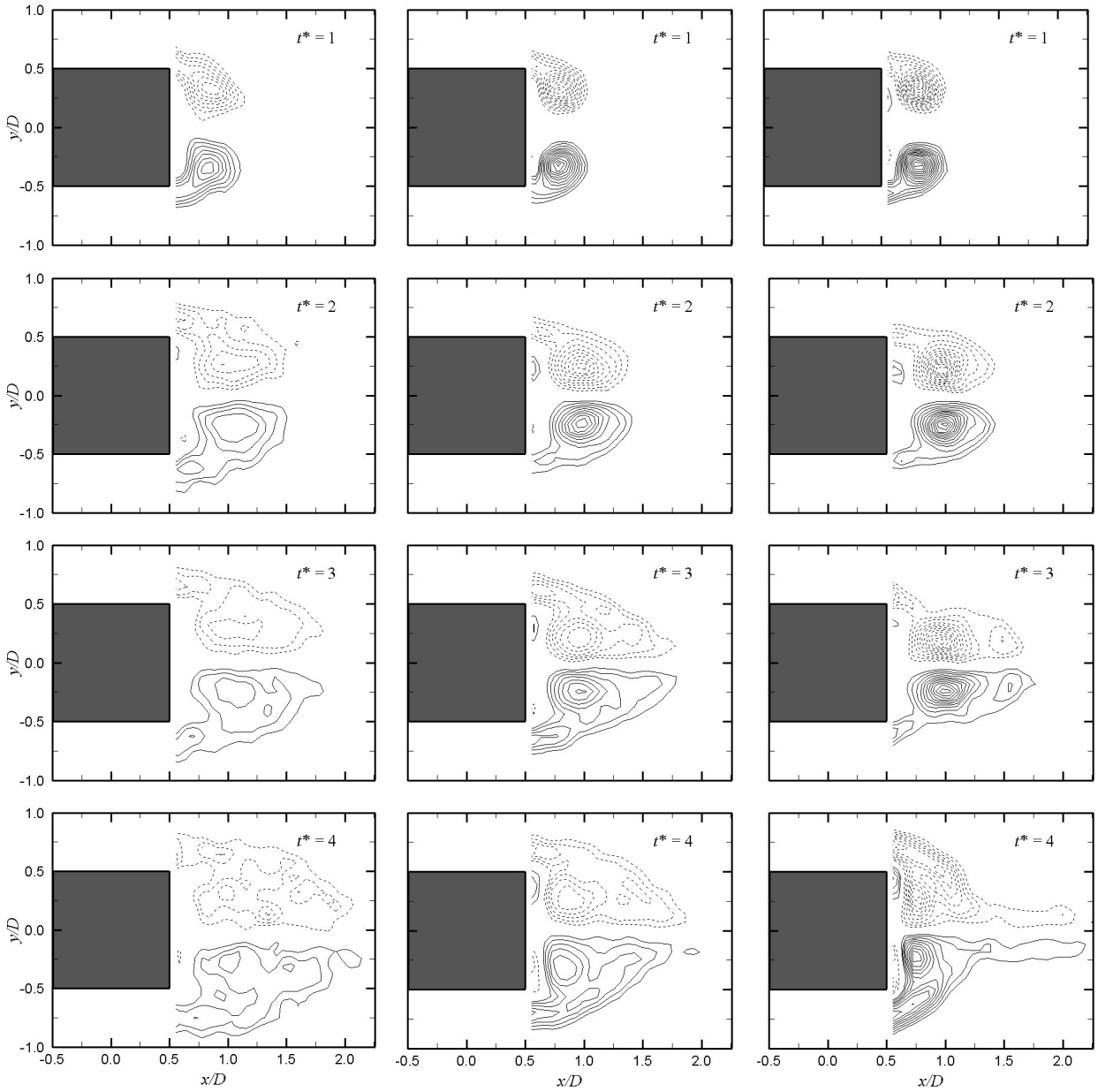

Figure 5.3: A comparison of the vorticity contours in the wake of an impulsively started square cylinder: (a) Re = 200, (b) Re = 500, (c) Re = 1000, at t^* = 1, 2, 3 and 4 after the start of motion. The dashed lines represent negative vorticity while the solid lines represent positive vorticity. The minimum vorticity contour is $|\omega^*| = 2$ and the interval between the contours is $\Delta\omega^* = 1$.

5.3 Length of the Recirculation Zone

The recirculation zone behind the cylinder is a low pressure zone formed as a result of the flow separation at the edges of the cylinder. From the velocity and vorticity field diagrams, Figures 5.2 and 5.3, the recirculation zone is seen to grow in size with time, a variation that is presented graphically in Figure 5.4(a) for Re = 500. For $t^* < 2$, there is an almost linear relationship between L_R/D and t^*; thereafter the rate of increase of L_R/D reduces and approaches an asymptote. The L_R/D curves for $a^* \geq 3$ are seen to merge into a common curve, an indication that the conditions corresponding to impulsive start have been attained. At any given point in time the L_R/D for low acceleration parameters, e.g. $a^* = 1$, is lower than for a higher acceleration parameters.

In Figure 5.4(b), L_R/D is plotted against the distance moved by the cylinder following the start of the impulsive motion, S/D. All the curves collapse onto a clear common curve. Therefore, the growth of the recirculation zone, at a particular Re, is primarily dependent on the distance moved rather than time. A similar observation is made for the circular cylinder (Figure 4.5(b)).

The length of the recirculation zone for a square cylinder is relatively independent of Re because of the fixed separation points. In fact, Lian and Huang (1989), from their study of the starting vortex behind a bluff body with sharp edges, noted that Re was of minor influence. In Figures 5.5(a) and 5.5(b), the recirculation zone length for Re = 200, 500 and 1000, is plotted against time and distance moved, respectively. Although the results seem close, a closer look at the data shows that the L_R/D for Re = 200 is higher than both for Re = 500 and 1000 and increases linearly with time and distance for the entire test.

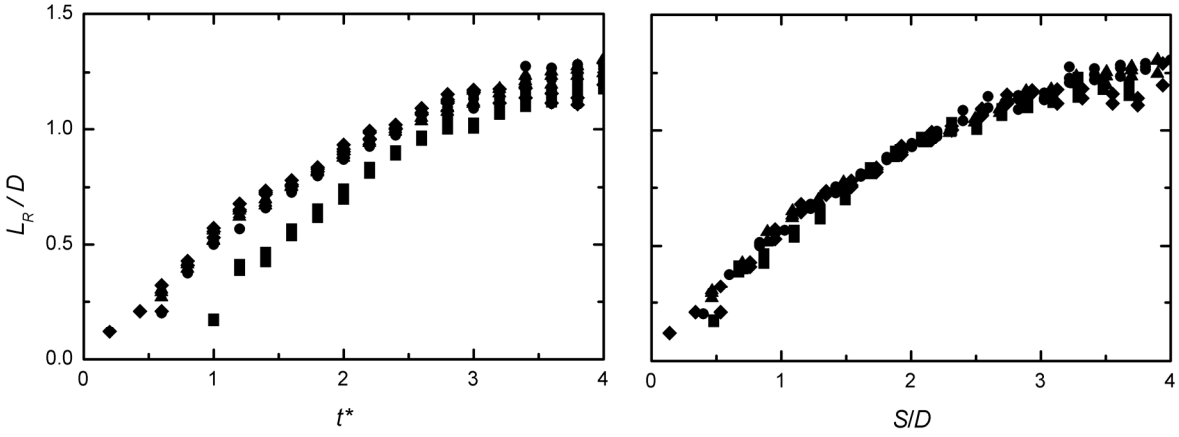

(a) (b)

Figure 5.4: Variation of the recirculation zone length (a) with time and (b) with the distance moved, for an impulsively started square cylinder, Re = 500. ■, $a^* = 1$; ●, $a^* = 3$; ▲, $a^* = 5$; ◆, $a^* = 10$.

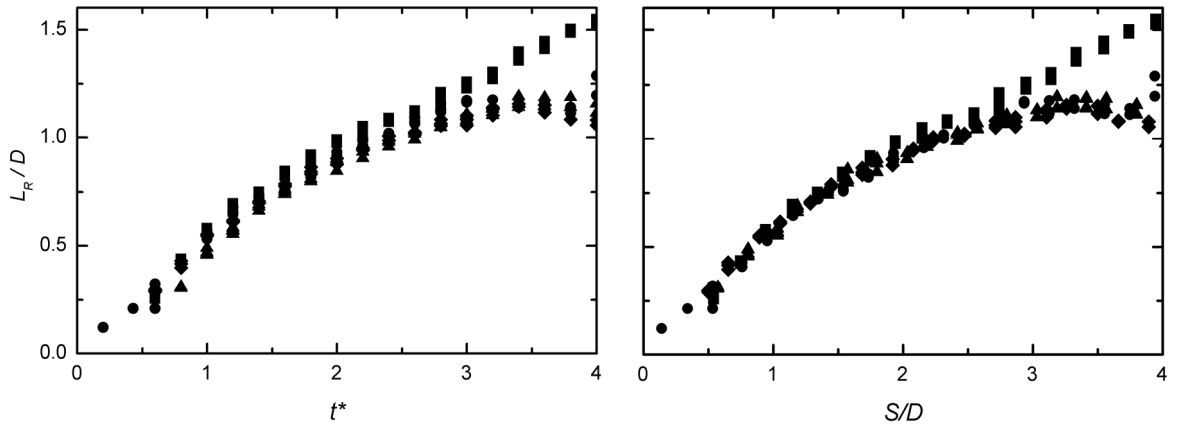

(a) (b)

Figure 5.5: Variation of the recirculation zone length (a) with time and (b) with the distance moved, for an impulsively started square cylinder, ■, Re = 200, $a^* = 10$; ●, Re = 500, $a^* = 10$; Re = 1000; ▲, $a^* = 3$; ◆, Re = 1000, $a^* = 5$.

5.4 Streamwise Location of the Primary Eddies

The location of the centers of the primary eddies in the streamwise direction, a/D, increases as the time advances from the start of the impulsive motion (Figure 5.6(a)). Because the vortices are located within the recirculation zone, which continues to grow with time as more vorticity from the separated shear layer is fed into it, the location of their

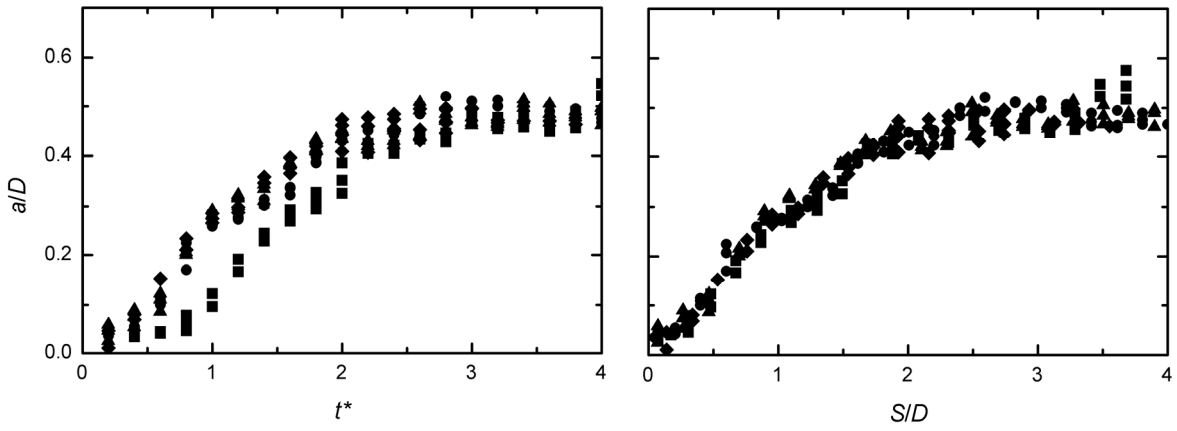

(a) (b)

Figure 5.6: The streamwise location of the primary vortices plotted against (a) time and (b) the distance moved, for an impulsively started square cylinder, Re = 500. ■, $a^* = 1$; ●, $a^* = 3$; ▲, $a^* = 5$; ◆, $a^* = 10$.

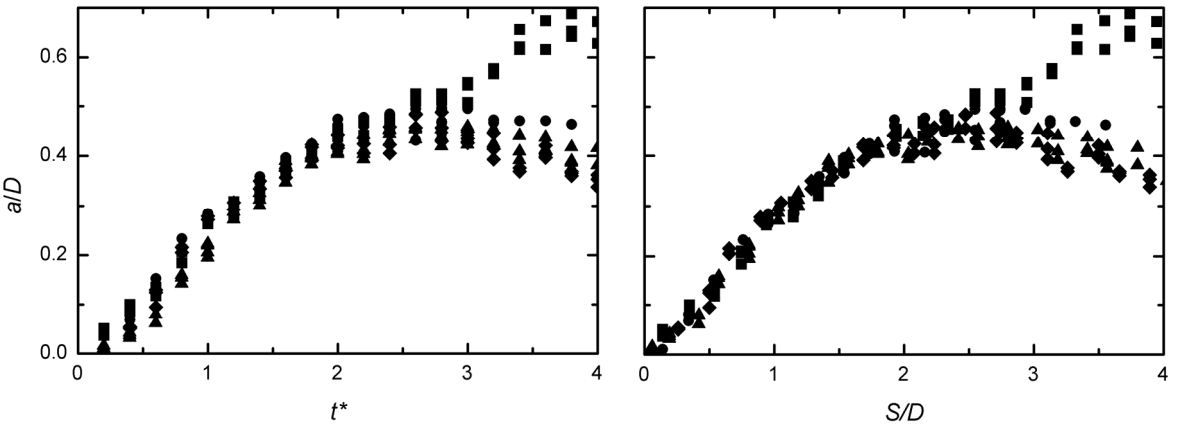

(a) (b)

Figure 5.7: Variation of the streamwise location of the primary vortices (a) with time and (b) with the distance moved, for an impulsively started square cylinder, ■, Re = 200, $a^* = 10$; ●, Re = 500, $a^* = 10$; Re = 1000; ▲, $a^* = 3$; ◆, Re = 1000, $a^* = 5$.

centers moves progressively farther away from the cylinder with the growth of the recirculation zone. At any given point in time, the location of the vortices for low a^* are lower than those of higher a^*. Although all the curves merge when a maximum value of a/D is reached, the curves for $a^* \geq 3$ are seen merge onto a common curve from $t^* = 0$. For all the a^* examined, a maximum value of $a/D \approx 0.5$ is reached, beyond which, there seems to be no

further increase in a/D within the time measured. While this occurs for $t^* > 2.5$, a similar behavior in the L_R results for Re > 500 occurs for $t^* \geq 3$. The maximum a/D attained is about half the maximum value of L_R attained.

Figure 5.7(a) shows the streamwise location of the primary vortices for Re = 200, 500 and 1000 plotted against elapsed time. There is a slight difference between the data for all the Re examined. For $t^* < 2$, all the curves follow the same trajectory with those for Re = 200 being slightly higher than the rest. However, at $t^* > 2$, a clear trend is established: the curves for Re = 500 and 1000 start to settle while that of Re = 200 continues to increase until the end of the test range, in line with the increase in size of the recirculation zone.

When the results are plotted against the distance moved, Figure 5.7(b), the data follow a similar trend as when plotted against t^*, Figure 5.7(a). The fact the data remain distinct even when plotted against the distance moved, shows that the location of the primary eddies depends on the Re.

5.5 Cross-Stream Spacing of the Primary Eddies

The primary eddies, at the early stages of formation, appear as small spiral wraps at the edges of the cylinder, as seen in the vorticity contour diagrams in Figure 5.2(b), $t^* = 1$. This is due to the presence of a small separation region near the sharp edge of the square while the entire flow field is basically potential flow (Lian and Huang, 1989). However, as time advances, the primary vortices grow in size and their center moves closer towards the wake centerline. The generation of the reversal flow in the recirculation zone enhances the movement of the vortex centers towards the centerline.

Figure 5.8(a) shows the variation of the cross-stream spacing between the primary eddies, b/D, with time. The spacing of the vortices at the start of the early stages of formation

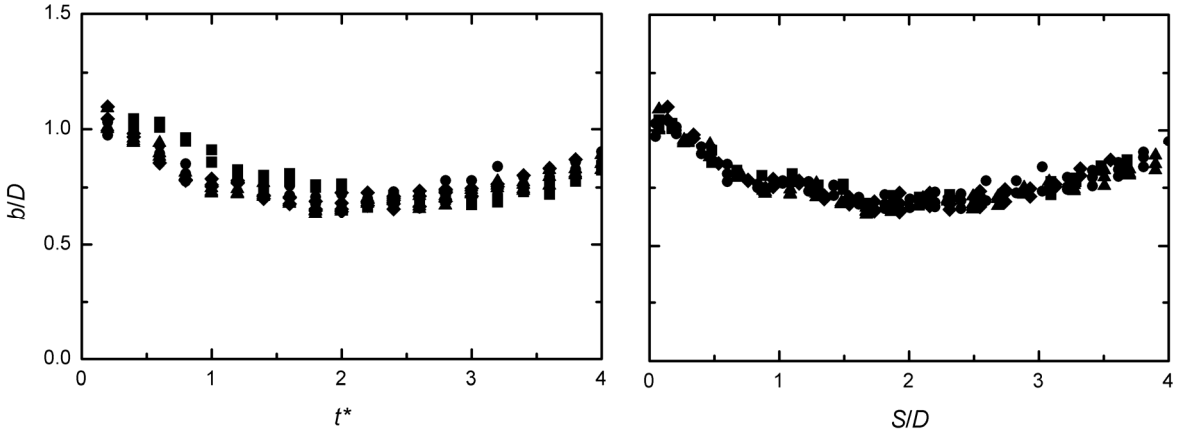

(a) (b)

Figure 5.8: The cross-stream (transverse) spacing between the centers of the primary eddies within the recirculation zone of an impulsively started square cylinder plotted against (a) time and (b) the distance moved, at Re = 500. ■, $a^* = 1$; ●, $a^* = 3$; ▲, $a^* = 5$; ◆, $a^* = 10$.

is at the highest value, equivalent to about one side of the cylinder in size. As time advances, there is a reduction in the cross-stream spacing of the vortices owing to the movement of the vortices towards the centerline, a situation occasioned by the creation of a low pressure zone.

The cross-stream spacing then settles at a constant value before beginning to increase again at $t^* > 3.5$. Lee *et al.* (1996) explained that this observation was due to the joining of the "tertiary" flow to the recirculation flow. Tertiary flow is the flow that develops on the upper and lower surfaces of the cylinder following flow separation from the leading edges of the cylinder. Therefore, once the separated flow from the leading edge of the cylinder joins the recirculation zone, the size of the recirculation zone increases in width and therefore the location of the vorticity centroid moves outwards.

From the current experiment, it was impossible to see the separation from the leading edge of the cylinder when the cylinder was moved from left to right, since the cylinder shadow was formed when the laser sheet was shone, making only the wake visible (Figure 5.1). However, when the cylinder was moved in the opposite direction, the separation was

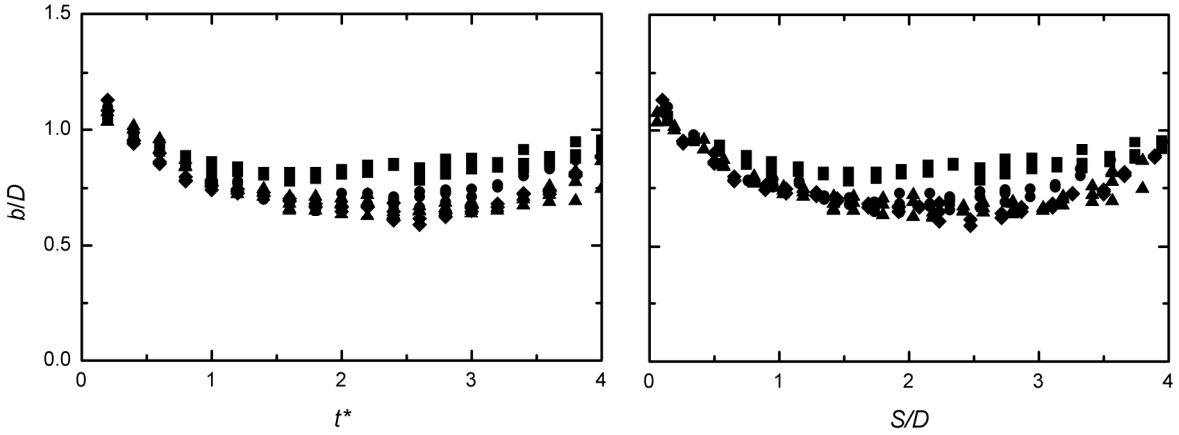

(a) (b)

Figure 5.9: The transverse spacing of the primary eddy centers for an impulsively started square cylinder plotted against (a) time and (b) the distance moved, ■, Re = 200, $a^* = 1$; ●, Re = 500, $a^* = 10$; ▲, Re = 1000, $a^* = 3$; ◆, Re = 1000, $a^* = 5$.

seen to occur, as shown in Figure 5.10. These instantaneous velocity and vorticity fields show the separation at the front side of the cylinder.

The b/D results for various a^*, at Re = 500, are seen to collapse onto a common curve when plotted against the distance moved from the start of motion, Figure 5.8(b). This behavior is consistent with the results of L_R/D, (Figure 5.5(b)), a/D (Figure 5.6(b)), and Γ^*, (Figure 5.10(b)). The development of the transverse spacing with time is different for different Re. Figure 5.9(a) shows that the cross-stream spacing for Re = 200 is greater than those of Re = 500 and 1000. Although at the start of the motion, all the Re yield a similar value of b/D, the profile for Re = 200 is higher immediately afterwards as compared to those of Re = 500 and 1000. The recirculation zone for Re = 200 is slightly larger than those for Re = 500 and 1000 (Figure 5.3) at any point in time, yet the amount of vorticity supplied to the vortices was the same for all the Re (Section 5.4). Therefore, the same amount of vorticity had to be spread over a larger area for Re = 200 and a smaller area for both Re = 500 and 1000. The resultant high concentration of vorticity for the high Re (Re = 500 and 1000) flows

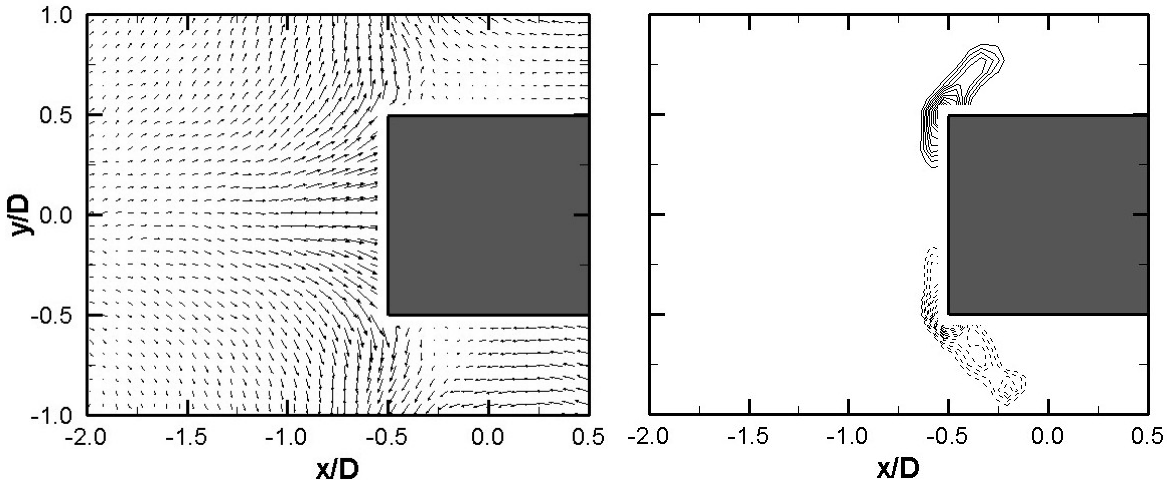

(a) (b)

Figure 5.10: A front view of an impulsively started cylinder at Re = 500, $a^* = 10$, $t^* = 4$; (a) the instantaneous velocity field diagram and (b) the corresponding vorticity field diagram. Dashed lines represent negative vorticity while solid lines represent positive vorticity. The minimum vorticity contour is $|\omega^*| = 2$ and the contour interval is $\Delta\omega^* = 1$. The cylinder is moving from right to left.

increases the rate of vorticity diffusion towards the low pressure zone (closer to the centerline). The overall effect is the movement of the vorticity centroid closer to the centerline for higher Re while for lower Re, the vorticity remains relatively farther from the centerline. The profiles for all the Re are similar and follow the same trend, a trend that is not affected when the transverse spacing, *b/D*, is plotted against the distance moved from the start of the motion, Figure 5.9(b).

5.6 Strength (Circulation) of the Primary Vortices

Owing to the symmetry of the square cylinder, the primary vortices formed in the recirculation zone are of always equal strength and rotate in opposite directions. As the shear layers separate from the surface of the cylinder, they are fed to the zone thereby increasing the strength of the primary eddies. Figure 5.11(a) shows that the strength of the primary eddies increases linearly with time. At any given point in time, the circulation for a lower

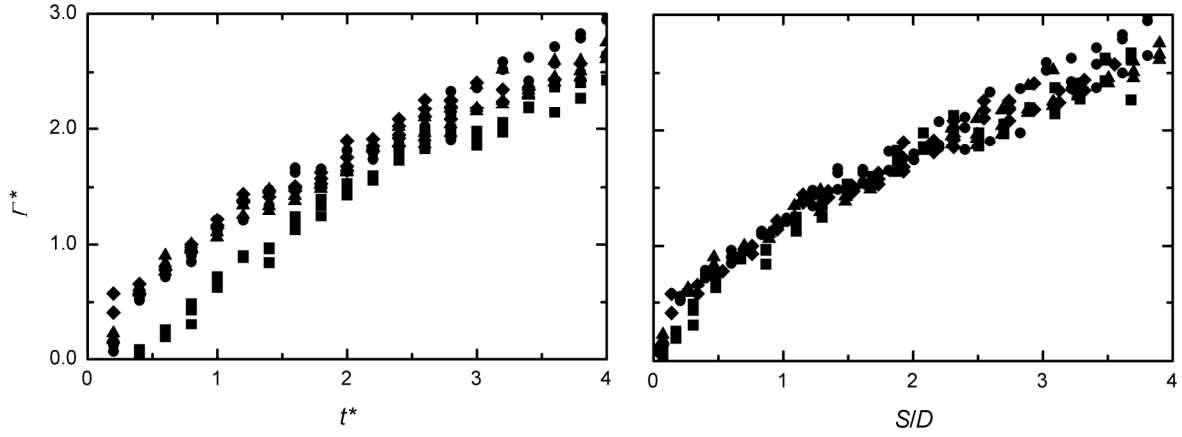

Figure 5.11: The dimensionless strength (circulation) of the primary vortex plotted against (a) time and (b) the distance moved, for an impulsively started square cylinder, Re = 500. ■, $a^* = 1$; ●, $a^* = 3$; ▲, $a^* = 5$; ◆, $a^* = 10$.

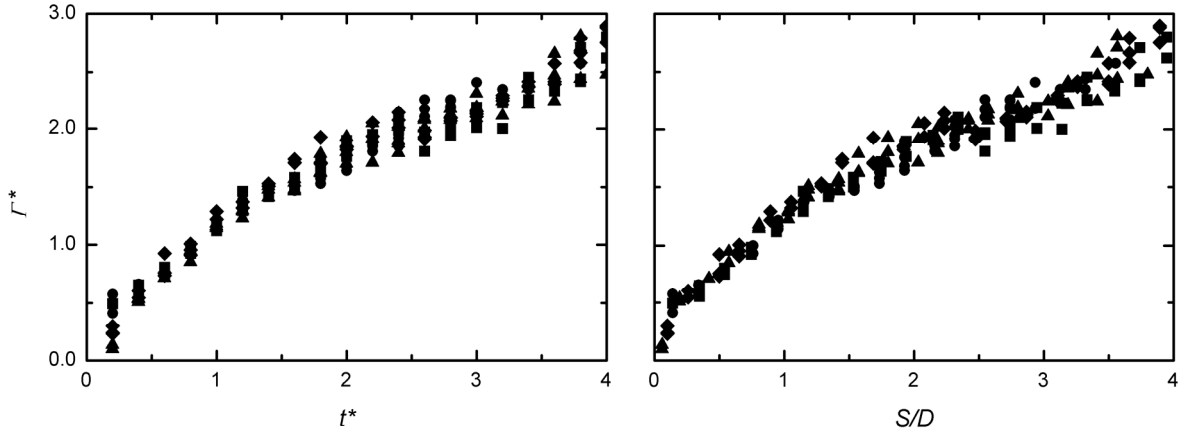

Figure 5.12: The dimensionless strength (circulation) of the primary vortex plotted against (a) time and (b) the distance moved, for an impulsively started square cylinder. ■, Re = 200, $a^* = 10$; ●, Re = 500, $a^* = 10$; ▲, Re = 1000, $a^* = 3$; ◆, Re = 1000, $a^* = 5$.

value of a^* is lower than that of higher value of a^*. For $a^* \geq 3$ (corresponding to impulsive start), the circulation curves merge to form a common curve right from $t^* = 0$.

When the results are plotted against the distance moved from the beginning of the impulsive motion, Figure 5.11(b), the results are seen to collapse onto a single curve with a definite linear relationship.

Unlike the circular cylinder, the strength of the primary vortex for a square cylinder is independent of Re. Figure 5.12(a) shows the variation of circulation with t^* for Re = 200, 500 and 1000. As it can be seen, there is an insignificant difference in the curves of each Re − they follow the same trend. This is mainly attributed to the fact the separation points of the square cylinder are fixed and independent of Re. All curves for different Re are seen to collapse onto a common curve when plotted against the distance moved from the start of motion, Figure 5.12(b).

5.7 Maximum Vorticity within the Primary Vortex

The maximum vorticity, ω_{max}, within the primary vortex for an impulsively started square cylinder increases with time, as shown in Figure 5.13(a) for Re = 500. The peak of the curve, corresponding to a maximum value, is reached at a time similar to the end of the acceleration phase of the cylinder. At low values of a^* it takes a much longer time to reach the local maximum value, and when reached, the peak value is much lower than that of $a^* \geq 3$. The peak vorticity may be a result of the transfer of vorticity from the surface of the cylinder to the recirculation zone by the force of inertia when the cylinder stops accelerating at the end of the acceleration phase. The rate of vorticity generation and transfer into the recirculation zone is the same for all the a^*, therefore, once the peak value has been reached the curves then collapse onto a common curves with similar values. There is a small decay (possibly by diffusion) in the values of the maximum vorticity before eventually settling at a constant value.

Figure 5.13(b) shows the relationship of the maximum vorticity for an impulsively started square cylinder with distance moved from the impulsive start. The curves for $a^* \geq 3$ collapse very well onto a single curve right from $S/D = 0$. For $S/D < 2$, the maximum

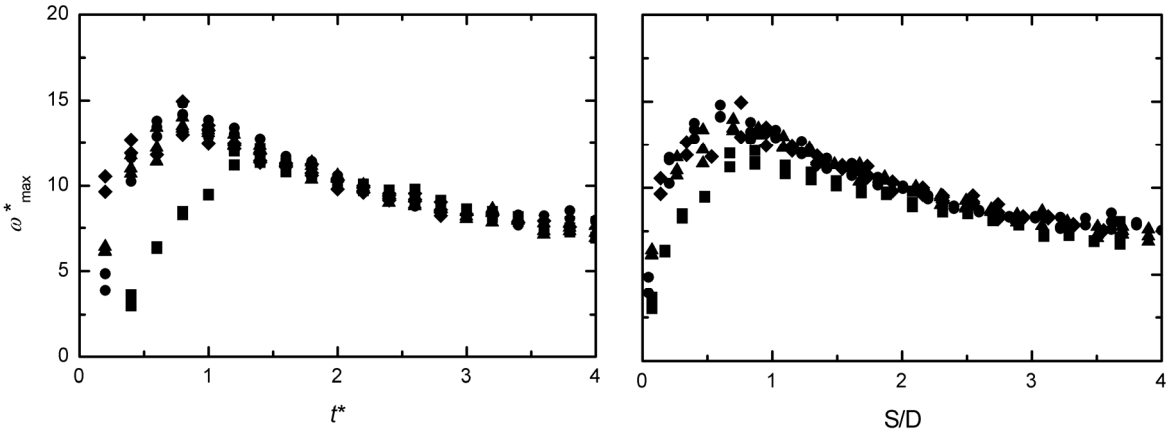

Figure 5.13: The maximum vorticity inside the primary vortex, plotted against (a) time and (b) the distance moved, for an impulsively started square cylinder, Re = 500. ■, $a^* = 1$; ●, $a^* = 3$; ▲, $a^* = 5$; ◆, $a^* = 10$.

vorticity of $a^* = 1$ is lower than those of $a^* \geq 3$, because the peak maximum vorticity reached within the vortex is different. All the curves begin to collapse onto a single curve from $S/D > 2$, corresponding to the point when the cylinder has reached a constant steady velocity and is also the point at which the curves of various a^* begin to merge to a single line (Figure 3.6(b)).

The maximum vorticity within the primary vortex for the impulsively started square cylinder is dependent on the Reynolds number. Figure 5.14(a) shows the variation of ω^*_{max} with time for Re = 200, 500 and 1000. The peak values of ω^*_{max} are directly affected by Re. The maximum vorticity within the primary vortex increases as the Re increases as shown in Table 5.1.

Figure 5.14(b) shows the relationship between the maximum vorticity and the distance moved from the start of the impulsive motion. Behaviour, similar to Figure 5.14(a), is observed, indicating that there is a change in ω^*_{max} whenever Re changes.

Table 5.1: The relationship between the maximum vorticity, Re and a^*

Re	U [mm/s]	a^*	a [mm/s^2]	Peak ω^*_{max}	Steady ω^*_{max}
200	7.5	10	25.2	10	5
500	20	1	15.7	11	8
		10	157	14	8
1000	40	5	314	17	11

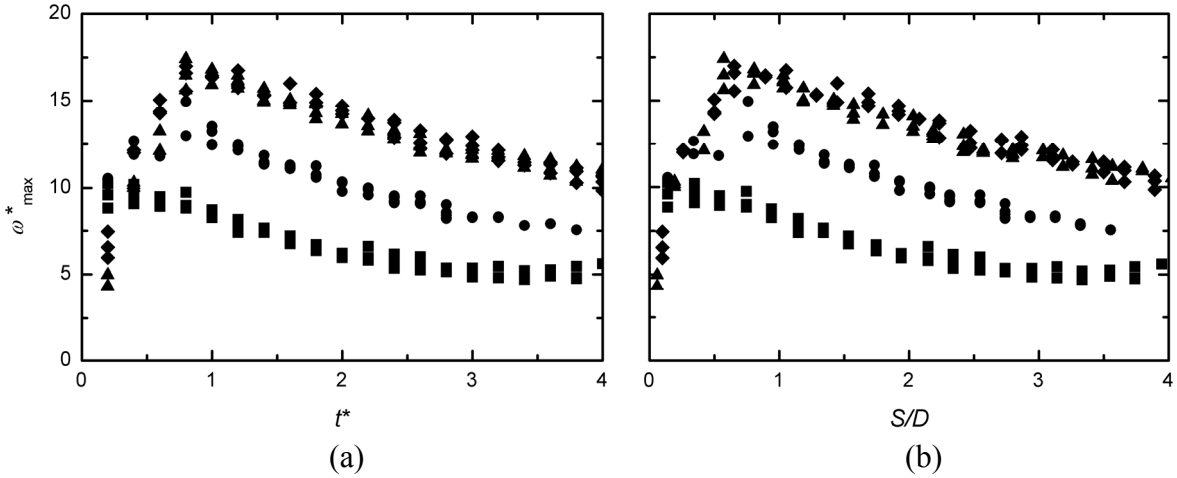

(a) (b)

Figure 5.14: The maximum vorticity inside the primary vortex of an impulsively started square cylinder plotted against (a) time and (b) the distance moved. ■, Re = 200, a^* = 1; ●, Re = 500, a^* = 10; ▲, Re = 1000, a^* = 3; ◆, Re = 1000, a^* = 5.

5.8 Velocities along the Wake Centerline

The velocity along the wake centerline for an impulsively started square cylinder at Re = 500 is shown in Figure 5.15. The profiles at t^* = 2 for $a^* \geq 3$ collapse onto a single curve while that of a^* = 1 is distinctively different from the rest (Figure 5.15(a)). This was due to the fact that the cylinder had not reached a steady velocity − the cylinder, at this instant was moving at a lower velocity (still in the acceleration phase). Once a steady velocity is reached for all the a^*, the profiles collapse onto a common curve, or at least take up values close to one another (Figure 5.15(b)).

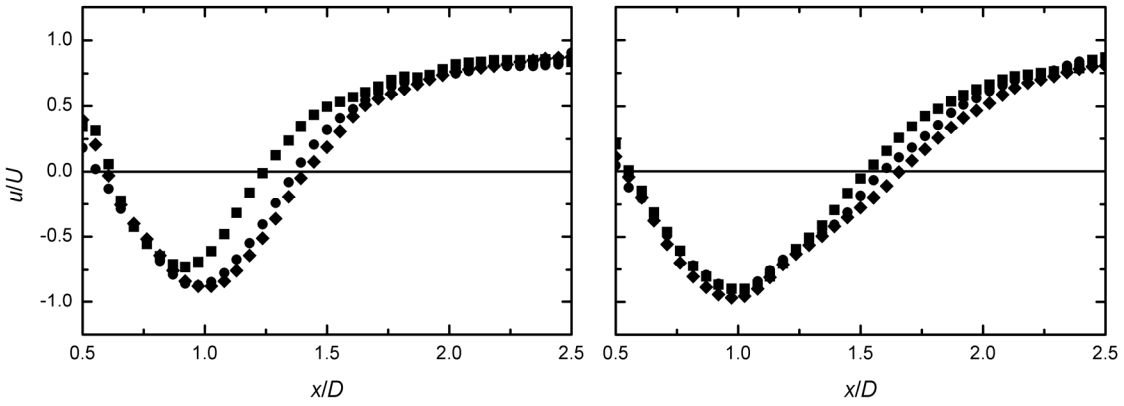

Figure 5.15: The velocity along the wake centerline of an impulsively started square cylinder, Re = 500, for (a) $t^* = 2$, (b) $t^* = 3$. ■, $a^* = 1$; ●, $a^* = 3$; ◆, $a^* = 10$.

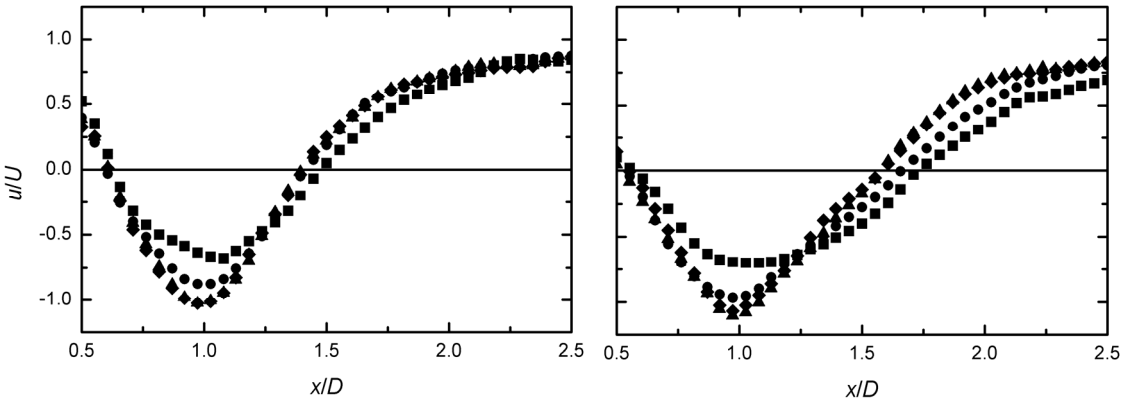

Figure 5.16: The velocity along the wake centerline for an impulsively started square cylinder at (a) $t^* = 2$, (b) $t^* = 3$. ■, Re = 200, $a^* = 10$; ●, Re = 500, $a^* = 10$; ◆, Re = 1000, $a^* = 3$.

A comparison between the wake centerline velocity at $t^* = 2$ and $t^* = 3$, for Re = 200, 500 and 1000, is shown in Figure 5.16(a) and Figure 5.16(b), respectively. The curves reach their lowest peak at about the same point, $x/D \approx 1.0$. The velocity profile for Re = 1000 has a sharp trough with the highest negative velocity value while Re = 200 has a gentle trough with the lowest negative velocity value. At all the t^*, the curves of Re = 200 cross the rear stagnation line ($u/U = 0$) much later than those of Re = 500 and 1000. This is consistent with the L_R results that L_R for Re = 200 is higher than L_R for Re = 500 and 1000 (Figure 5.5(a)). A

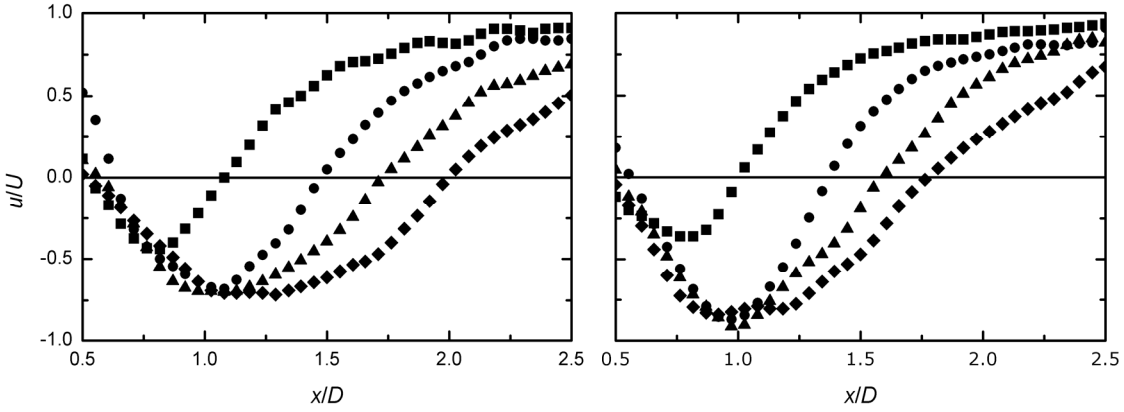

(a) (b)

Figure 5.17: The velocity along the wake centerline of an impulsively started square cylinder, (a) Re = 200, (b) Re = 500. ■, $t^* = 1$; ●, $t^* = 2$; ▲, $t^* = 3$; ◆, $t^* = 4$

strong reverse flow with a velocity magnitude greater than the freestream velocity is evident at $t^* = 3$ ($u \approx -1.2U$).

The velocity along the wake centerline for Re = 200 and Re = 500 at various t^* is shown in Figure 5.17(a) and Figure 5.17(b), respectively. The graphs show the development of the velocity along the wake centerline as time advances from the start of motion. At the start of motion, there is no back flow since the flow is irrotational. Once the separation occurs and the vortex pairs start developing in the recirculation zone, the backward flow is formed − this appears as the negative velocity flow in the centerline velocity diagrams. For both Re = 200 and Re = 500, the flow depicts very little backward flow at the initial stages of motion, for example, a minimum of $u/U = -0.5$, is attained at $t^* = 1$ for both Re = 200 and 500. However, the backwards flow velocity increases with time, e.g. at $t^* = 3$ (Figure 5.16(b)) the minimum backwards velocity has an absolute value more than the freestream velocity at some point ($u/U > -1$).

The maximum velocity along the wake centerline increases as the Re increases. The maximum negative velocity value for Re = 200 is -0.75 (Figure 5.17(a)) while that of Re =

500 is -0.9 (Figure 5.17(b)). This maximum value is reached after the cylinder has attained a steady velocity and does not change with time. The velocity profile for various t^* is the same as they descend to the peak. The only difference is how the velocity recovers after reaching the peak value, and this is what determines the position where the curves cross the "stagnation line" and in turn the L_R.

CHAPTER SIX

DIAMOND CYLINDER RESULTS AND DISCUSSION

6.1 Introduction

When a diamond-shaped cylinder is impulsively started from rest in a quiescent fluid, like any other bluff body with sharp edges, the flow immediately begins to separate at the side edges of the cylinder to form a wake at the back of the cylinder. A pair of vortices of equal strength and rotating in opposite direction is then formed in the wake. The vortices are initially symmetrical but as time goes by they become asymmetrical and are eventually shed.

For the diamond cylinder, the position of the vortex centers in the streamwise direction, a, is measured from the center of the cylinder while the cross-stream spacing, b, is the distance between the two vortex centers in the cross-stream direction, (Figure 6.1). The length of the recirculation zone, L_R, is the distance from the center of the cylinder to the point on the wake centerline where the velocity is the same as the freestream velocity.

Figure 6.2 shows a PIV image of the diamond cylinder as captured by the camera during motion. The tracer particles in the image appear as bright spots while the back of the cylinder appears as a continuous, 90^0-bend white line, which is used to determine the spatial position of the cylinder at any time. All the images captured are processed using the procedure described in Chapter 3 to obtain the instantaneous velocity and vorticity fields.

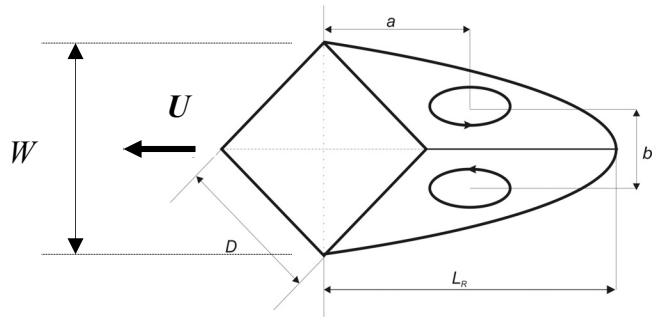

Figure 6.1: The nomenclature of the geometric parameters of a closed wake behind the diamond cylinder. *W* is the length of the cylinder diagonal.

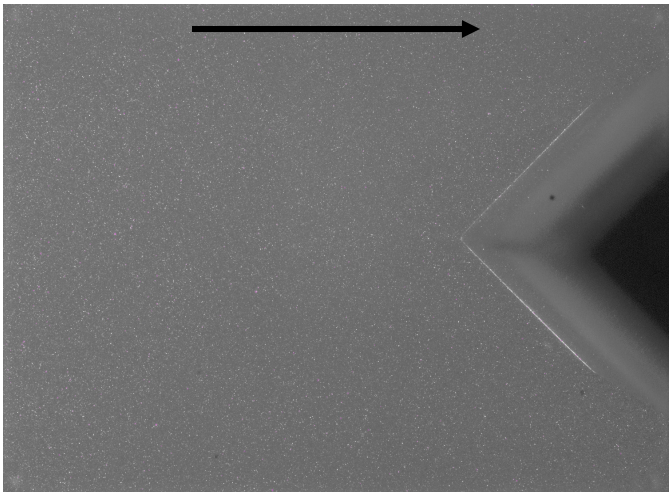

Figure 6.2: A PIV image of the cylinder at some point during the motion. The cylinder is moving from left to right.

6.2 Velocity Fields

Figure 6.3 shows the instantaneous velocity fields around an impulsively started diamond cylinder at Re = 1000 and the corresponding vorticity fields, while Figure 6.4 shows, in a comparative manner, the instantaneous vorticity fields for the impulsively started diamond cylinder at Re = 200, 500 and 1000. The development of the vorticity fields with time is a representation of how the flow develops with time. It can be seen that in the early stages of motion, the vortices start forming at the outermost edges of the cylinder and as time advances; they increase in size and move farther away from the cylinder. Sizewise, the

vortices at lower Reynolds number, e.g. Re = 200, are larger than those of higher Reynolds number.

Secondary vorticity is seen to appear after $t^* \geq 2$. The positive vorticity starts to build on the upper side of the cylinder while the negative vorticity appears on the lower side of the cylinder. The size of the secondary vortex is also seen to grow in time.

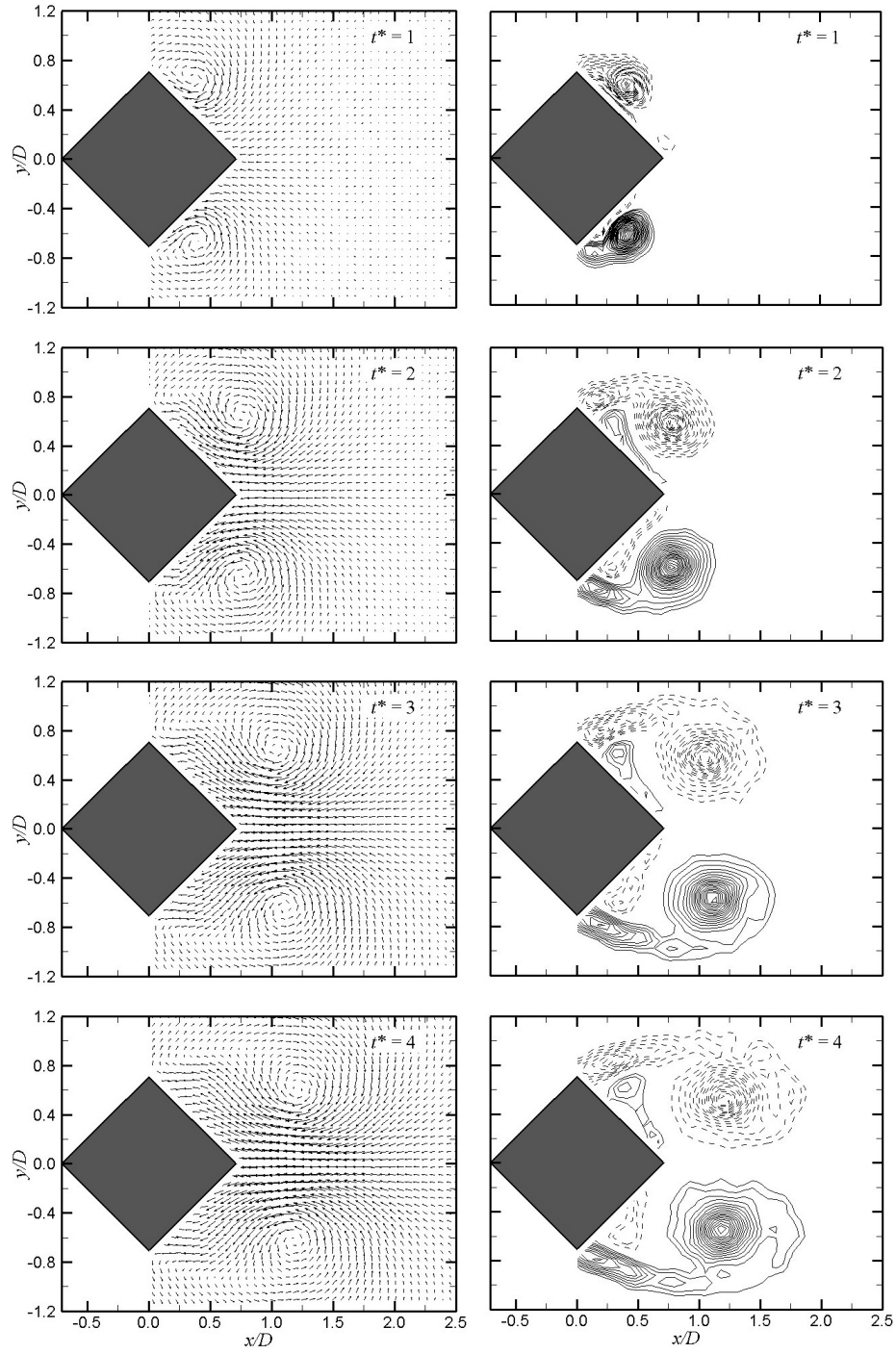

Figure 6.3: An impulsively started diamond cylinder at Re = 1000, $a^* = 5$: (a) instantaneous velocity fields, (b) corresponding instantaneous vorticity fields. The cylinder is towed from right to left. Dashed lines represent negative (CW) vorticity while the solid lines represent positive (CCW) vorticity. The minimum vorticity contour is $|\omega^*| = 2$ and the contour interval is $\Delta\omega^* = 1$.

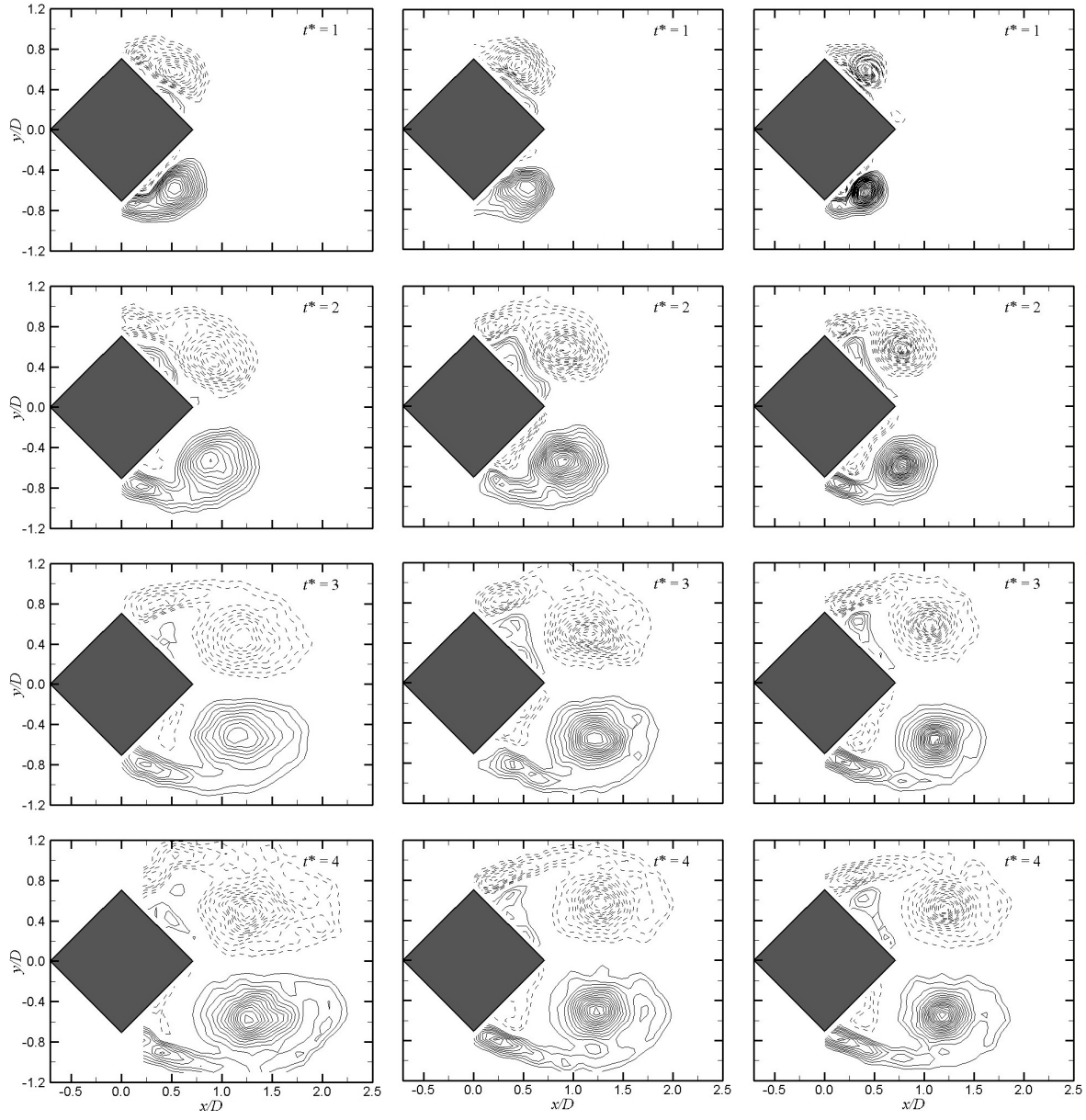

Figure 6.4: The instantaneous vorticity fields diagrams of an impulsively started diamond cylinder, (a) at Re = 200, $a^* = 10$; (b) at Re = 500, $a^* = 10$; (c) at Re = 1000, $a^* = 5$. The cylinder is towed from right to left. Dashed lines represent negative (CW) vorticity while the solid lines represent the positive (CCW) vorticity. The minimum vorticity contour is $|\omega^*| = 2$ and the contour interval is $\Delta\omega^* = 1$.

.

6.3 Length of the Recirculation Zone

The length of the recirculation zone behind an impulsively started diamond cylinder depends on the acceleration parameter and varies with time. Due to the fixed separation points at the edges of the cylinder, the vortex formation starts at the edges of the cylinder appearing as small spiral wraps which results from the separated shear layers (Lian and Huang, 1989). As these small wraps grow in size, the enclosing streamlines also grow and eventually meet at some point at the wake centerline forming a closed streamline which then clearly defines the recirculation zone (Figure 6.5). Until the closed streamline is formed, the length of the recirculation zone is not well defined since there is only a single stagnation point at the rear end of the cylinder.

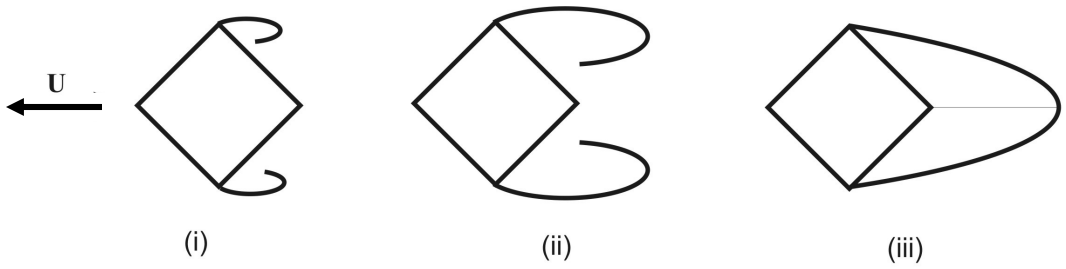

Figure 6.5: A schematic sketch of the vortex development in an impulsively started diamond cylinder at Re = 500: (i) the initial shear layer separation, (ii) the separated shear layers starts to form the vortices, (iii) the formation of a closed streamline.

In Figure 6.6(a), the variation of the length of the recirculation zone with t^* is shown for various acceleration parameters, at Re = 500. It can be noted that L_R increases linearly with t^* for all the a^* values examined. However, for $a^* \geq 3$, which corresponds to a near true impulsive start, the L_R curves clearly collapse onto a single curve whose values at any given point in time are higher than those of $a^* < 3$. The highest value of L_R of about $2.5D$ is reached at $t^* = 4$.

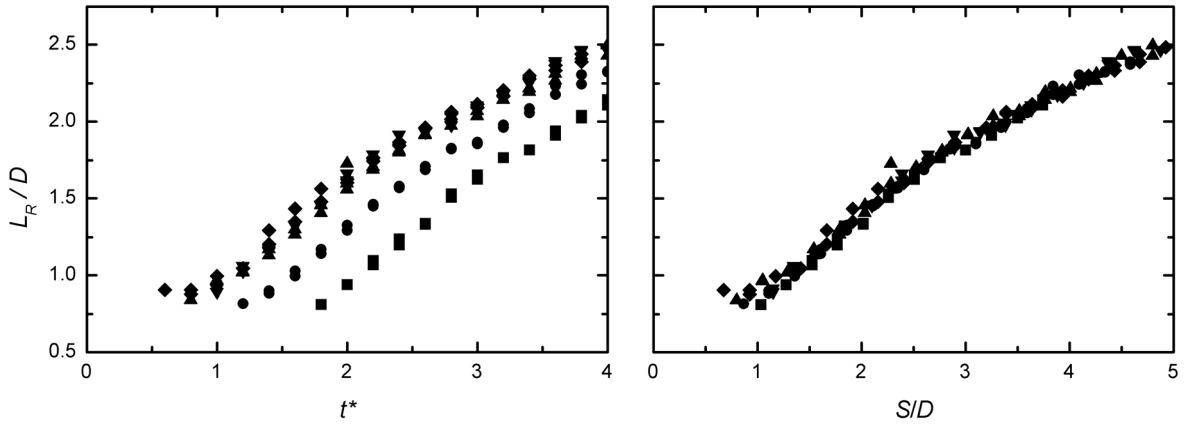

(a) (b)

Figure 6.6: The recirculation zone length of an impulsively started diamond cylinder plotted against (a) time and (b) the distance moved, Re = 500. ■, $a^* = 0.5$; ●, $a^* = 1$; ▲, $a^* = 3$; ▼, $a^* = 5$; ◆, $a^* = 10$.

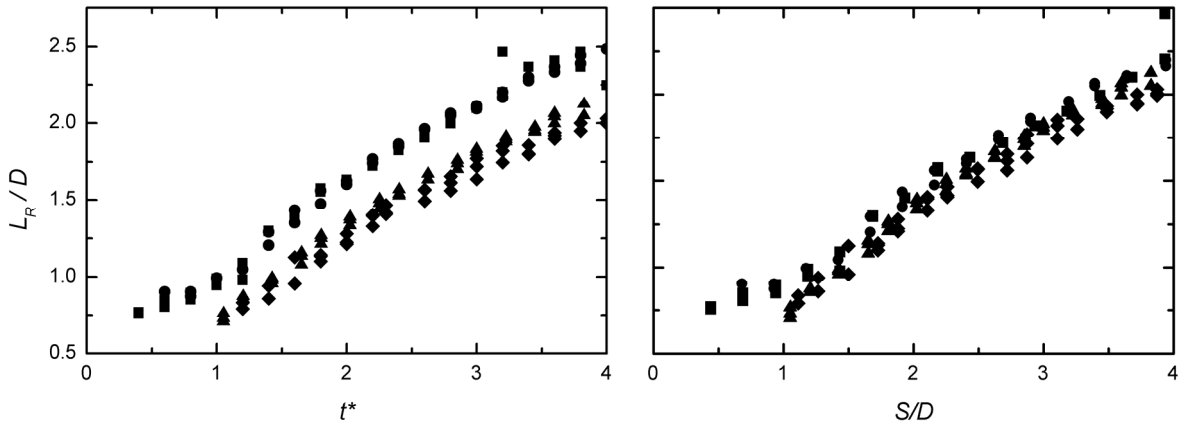

(a) (b)

Figure 6.7: Variation of the recirculation zone length (a) with time and (b) with the distance moved, for an impulsively started diamond cylinder, ■, Re = 200, $a^* = 10$; ●, Re = 500, $a^* = 10$; ▲, Re = 1000, $a^* = 3$; ◆, Re = 1000, $a^* = 5$.

Figure 6.6(b) shows the relation of L_R with the distance moved by the cylinder from the start of the impulsive motion. All the graphs collapse onto a common curve meaning that the rate of growth of the recirculation zone is more dependent on the distance moved by the cylinder from the start of the impulsive motion rather than the magnitude of acceleration.

The increase of the length of the recirculation zone occurs at different rates for different Re. Figure 6.7(a) shows the L_R/D - t^* profiles for Re = 200, 500 and 1000. For all

the Re, there exists a linear relationship between L_R and t^*, however, there are two clear curves- one for Re = 200 and 500 and the other for Re = 1000. When the results are plotted as a function of the distance moved from by the cylinder from the start of the impulsive motion, all the curves merge to a near common curve, Figure 6.7(b).

6.4 Streamwise Location of the Primary Eddies

The primary vortices formed following an impulsively started motion over a diamond cylinder, like in any other bluff body, undergo a series of stages in their development. When the motion begins, the vortices which are formed are symmetrical but as they continue to grow they become asymmetrical and are eventually shed in a periodic manner. This transformation of the vortices is accompanied by changes in their size and shape. The beginning of the symmetric stage is characterized by the vortices being closer to the cylinder and almost circular in shape (see Figure 6.3(b), $t^* = 1$, 2 and 3). Then as the time advances, they become large, elongated and take up a near oval shape (Figure 6.3(b), $t^* = 4$), and their centers, located using the vorticity centroid, move further away from the cylinder. Jeon and Gharib (2004) described this vortex development as the vortices' morphological change.

Figure 6.8(a) shows that the streamwise location of the vortices increases linearly with time for all the a^* examined. However, the rate of increase for a near true impulsively started motion, $a^* \geq 3$, is higher than that for a non-impulsively started motion, $a^* < 3$. The highest a/D value of $1.2D$ reached at $t^* = 4$ is about half the L_R reached at the same time. The variation of a/D with the distance moved from the start of an impulsive motion is shown in Figure 6.8(b). All the curves for various a^* examined collapse onto a single curve. This behavior is similar to the one seen in L_R (Figure 6.6(b)).

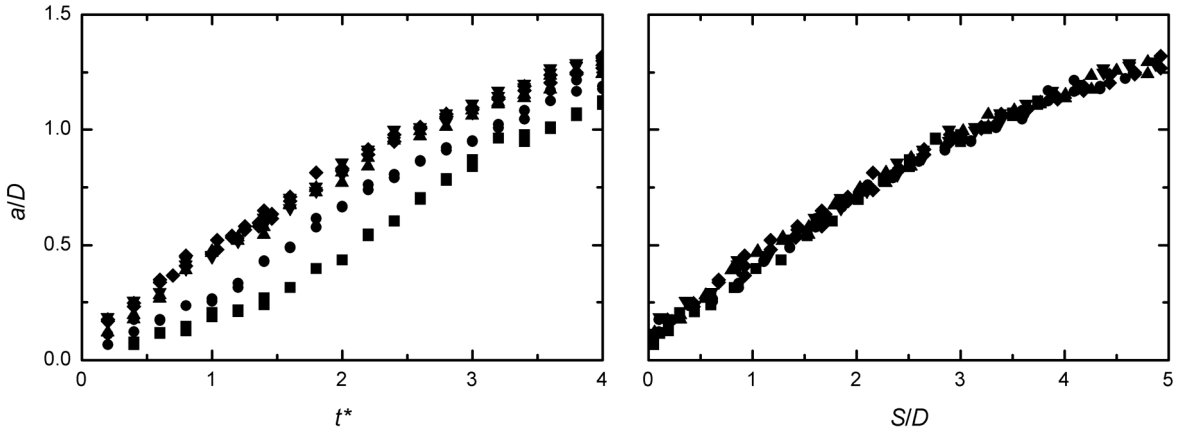

(a) (b)

Figure 6.8: The streamwise location, of the centers of the primary vortices in an impulsively started diamond cylinder plotted against (a) time and (b) the distance moved from the start of motion at Re = 500. ■, $a^* = 0.5$; ●, $a^* = 1$; ▲, $a^* = 3$; ▼, $a^* = 5$; ◆, $a^* = 10$.

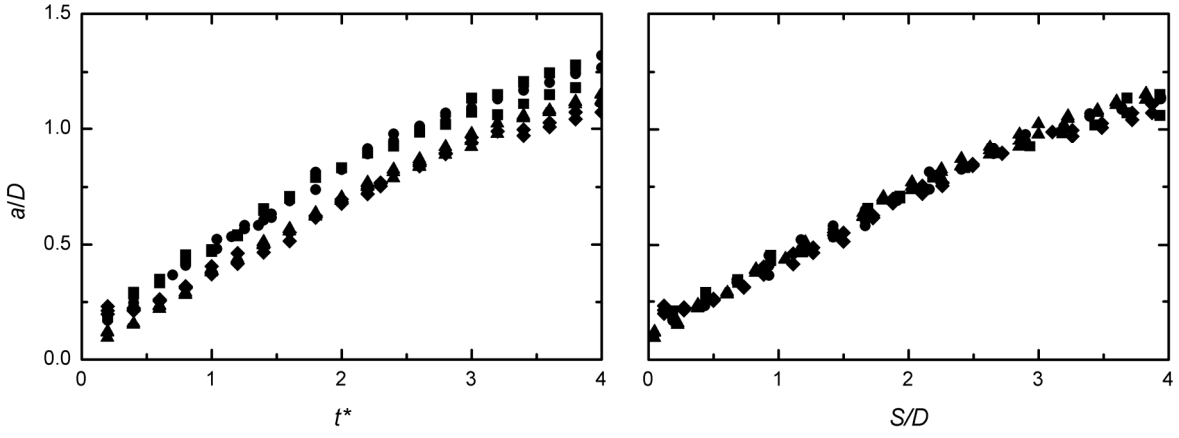

(a) (b)

Figure 6.9: Variation of the streamwise location of the primary vortices in an impulsively started diamond cylinder (a) with time and (b) with the distance moved, ■, Re = 200, $a^* = 10$; ●, Re = 500, $a^* = 10$; ▲, Re = 1000, $a^* = 3$; ◆, Re = 1000, $a^* = 5$.

Figure 6.9(a) shows the a/D - t^* profiles for Re = 200, 500 and 1000. The location of the centers of the primary eddies is dependent on Re. The location of the vortex center is closer to the cylinder for higher Re than for lower Re. The values, however, increase linearly with time for the entire test duration. In Figure 6.9(b), the a/D values for the various Re are plotted against the distance moved from the start of the impulsive motion and it can be

observed that the graphs once again merge onto a common curve. The location of the vortices is thus more dependent on the distance moved rather than the magnitude of acceleration.

6.5 Cross-Stream Spacing of the Primary Eddies

The cross-stream spacing of the vortices is relatively independent of both a^* and t^* due to the fixed separation points at the edges of the cylinder. Figure 6.10(a) shows the variation of b/D with t^*. At the start of the motion, the data are scattered around $\sqrt{2}$, which is equivalent to the length of the diagonal of the cylinder (the cylinder width, W, shown in Figure 6.1), before settling at some constant value of $b/D \approx 1.25$. Although the data show some scatter, especially for $t^* < 1.5$, corresponding to the acceleration phase, the data settle at an almost horizontal profile once the cylinder steady velocity has been attained, $t^* > 2$. Figure 6.10(b) shows the cross-stream spacing as a function of the distance moved from the start of the motion. All the curves merge onto a common horizontal profile.

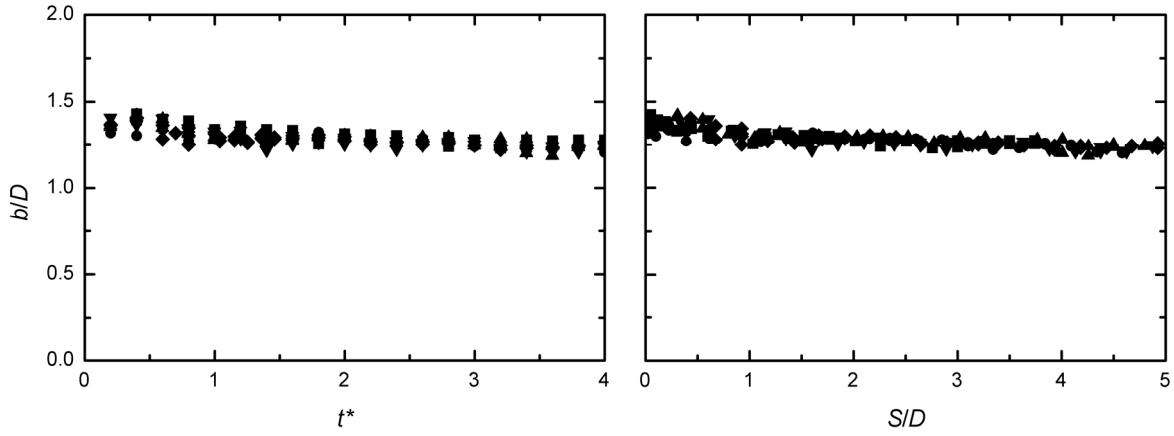

(a) (b)

Figure 6.10: The cross-stream spacing of the primary vortices in an impulsively started diamond cylinder plotted against (a) time and (b) the distance moved; Re = 500. ■, $a^* = 0.5$; ●, $a^* = 1$; ▲, $a^* = 3$; ▼, $a^* = 5$; ◆, $a^* = 10$.

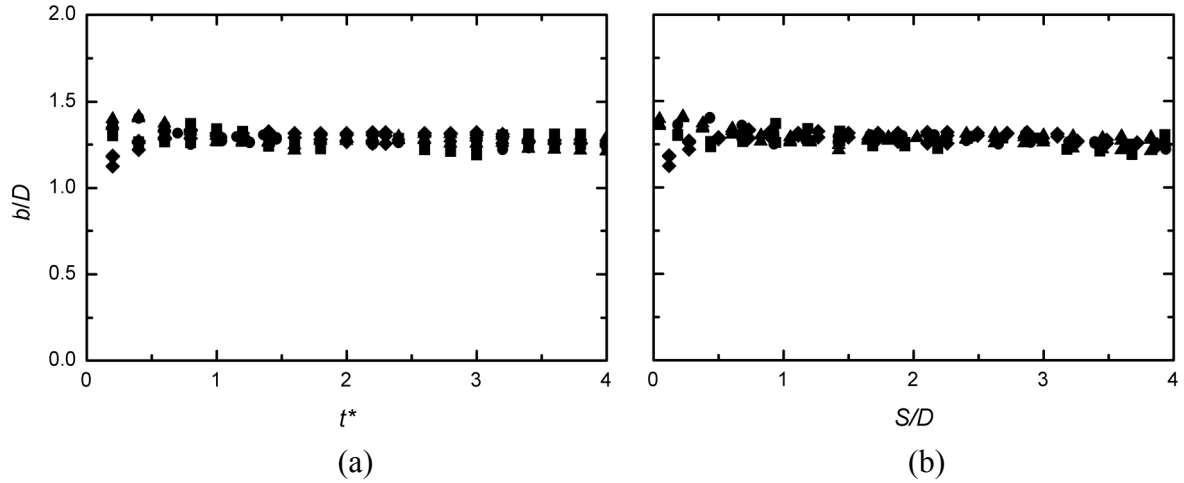

Figure 6.11: Variation of the cross-stream spacing of the primary vortices for an impulsively started diamond cylinder (a) with time and (b) with the distance moved, ■, Re = 200, $a^* = 10$; ●, Re = 500, $a^* = 10$; ▲, Re = 1000, $a^* = 3$; ◆, Re = 1000, $a^* = 5$.

The cross-stream spacing of the vortices is also independent on the Reynolds number (Figure 6.11(a)). All the curves for Re = 200, 500 and 1000 are virtually the same except at the start of the motion where there is some scatter. When the data finally settle, they assume a common horizontal curve. In Figure 6.11(b), the cross-stream spacing is plotted against the distance moved from the start of motion. It can be seen that all the curves merge onto a single common curve with a similar scatter around the start of motion. However, this scatter is lost once the cylinder reaches a steady velocity.

6.6 Strength of the Primary Vortices

Owing to the continuous supply of vorticity from the separated shear layers when the cylinder is moving, the circulation within the primary vortices increases almost linearly with time (Figure 6.12(a)). The rate of increase is, however, higher for higher values of a^* than for lower values of a^*. The vortex strength for $a^* \geq 3$ is seen to collapse onto a common curve. When the results are plotted against the distance moved from the start of the impulsive

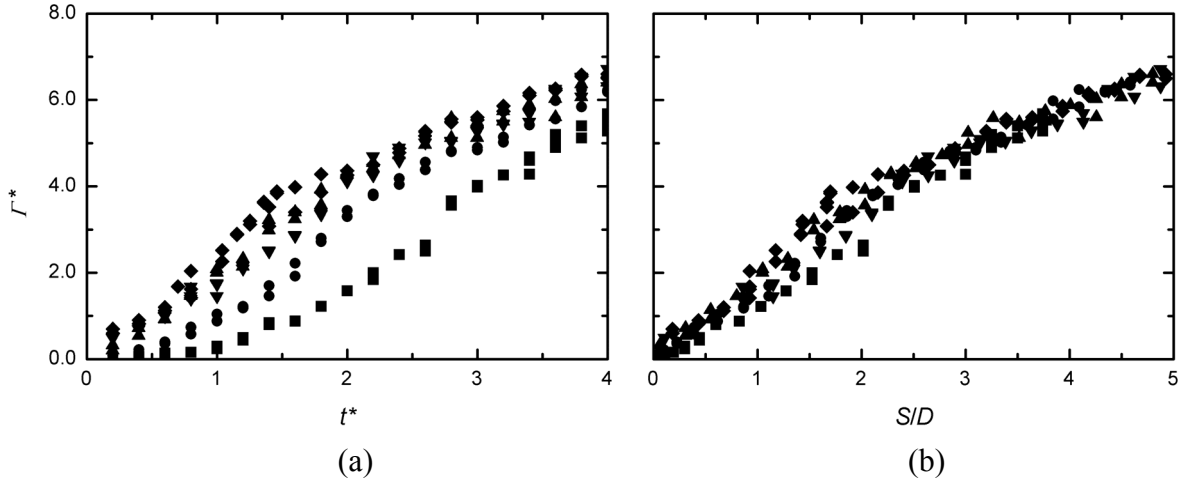

(a) (b)

Figure 6.12: The circulation (strength) of the primary vortices for an impulsively started diamond cylinder plotted against (a) time and (b) the distance moved at Re = 500. ■, $a^* = 0.5$; ●, $a^* = 1$; ▲, $a^* = 3$; ▼, $a^* = 5$; ◆, $a^* = 10$.

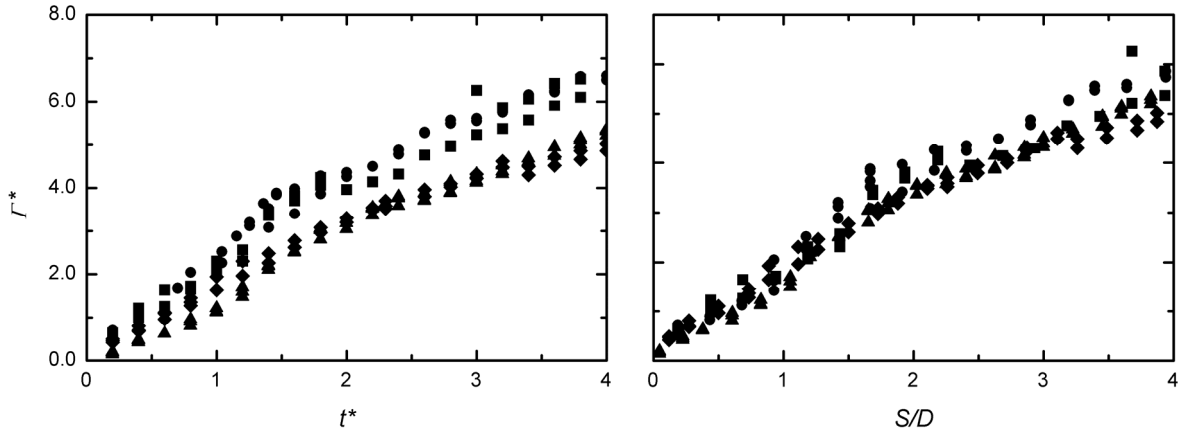

(a) (b)

Figure 6.13: The circulation (strength) of the primary vortices for an impulsively started diamond cylinder (a) with time and (b) with the distance moved, ■, Re = 200, $a^* = 10$; ●, Re = 500, $a^* = 10$; ▲, Re = 1000, $a^* = 3$; ◆, Re = 1000, $a^* = 5$.

motion, all the curves collapse onto a single common curve (Figure 6.12(b)), with a linear relationship.

Figure 6.13(a) shows the variation of the circulation with time for various Re. The circulation at all Re increases linearly with time but the circulation for Re = 1000 is lower than that of Re = 200 and 500. In Figure 6.13(b), the relationship between the circulation and

the distance moved from the start of motion is shown. All the curves merge onto one line with a definite linear relationship.

6.7 Maximum Vorticity within the Primary Vortex

The absolute maximum vorticity within the vortex is the maximum vorticity attained in the recirculation zone, usually in the 'eye' of the vortex, and it can be used to locate the vortex centers. The maximum vorticity increases linearly with time within the early stages of the start of the impulsive motion, (Figure 6.14(a)). The linear relationship ends at a time shortly after the end of the acceleration phase. The curves of $a^* \geq 3$ collapse onto a common curve and reach the highest peak value. Once the peak value has been reached the curves begin to settle and all the curves take up a similar profile with a steady value of $\omega^*_{max} \approx 15$. Unlike the impulsively started flow, which has an overshoot, the curves corresponding to the non-impulsively started flow, $a^* < 3$, begin to level off as they approach the highest $\omega^*_{max} \approx 15$. The ω^*_{max} values for the non-impulsively started flow are also much lower at any given point in time before the constant value is reached. It can also be noted that it takes much longer for the non-impulsively started flow to reach a constant value of ω^*_{max} , just like its acceleration phase of the flow.

The relationship between the maximum vorticity and the distance moved from the start of the impulsive motion is shown in Figure 6.14(b). Though the curves are similar at the start of the motion (they have the same value at $x/D = 0$), they begin to develop at different rates but eventually settle at the same steady value. It is therefore the way the vortices develop immediately after initiation (i.e. during the acceleration stage) that is unique for each a^*; this explains the why the curves do not merge for $S/D < 3$.

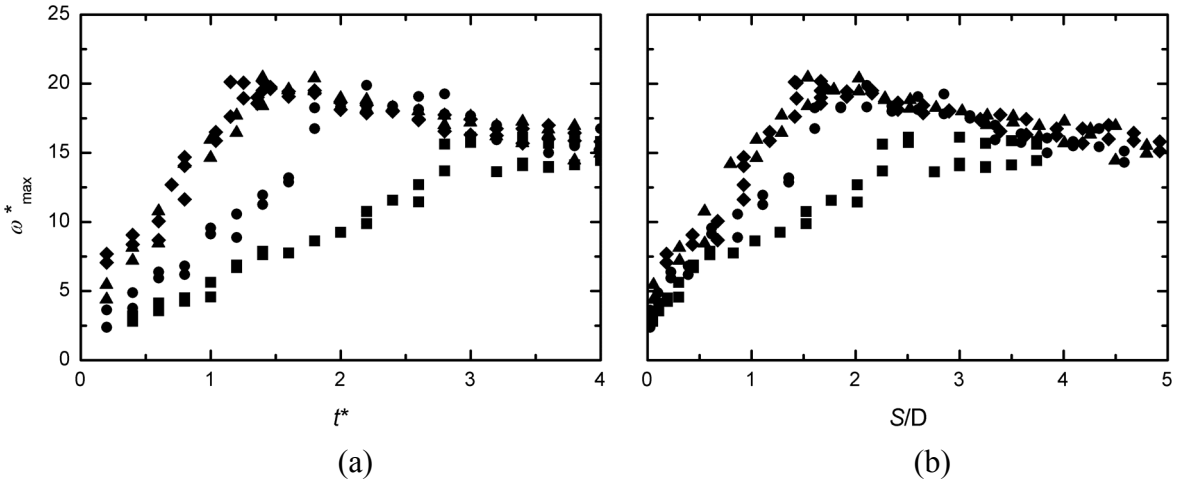

(a) (b)

Figure 6.14: The maximum vorticity within the primary vortices for an impulsively started diamond cylinder plotted against (a) time and (b) the distance moved; Re = 500. ■, $a^* = 0.5$; ●, $a^* = 1$; ▲, $a^* = 3$; ▼, $a^* = 5$; ◆, $a^* = 10$.

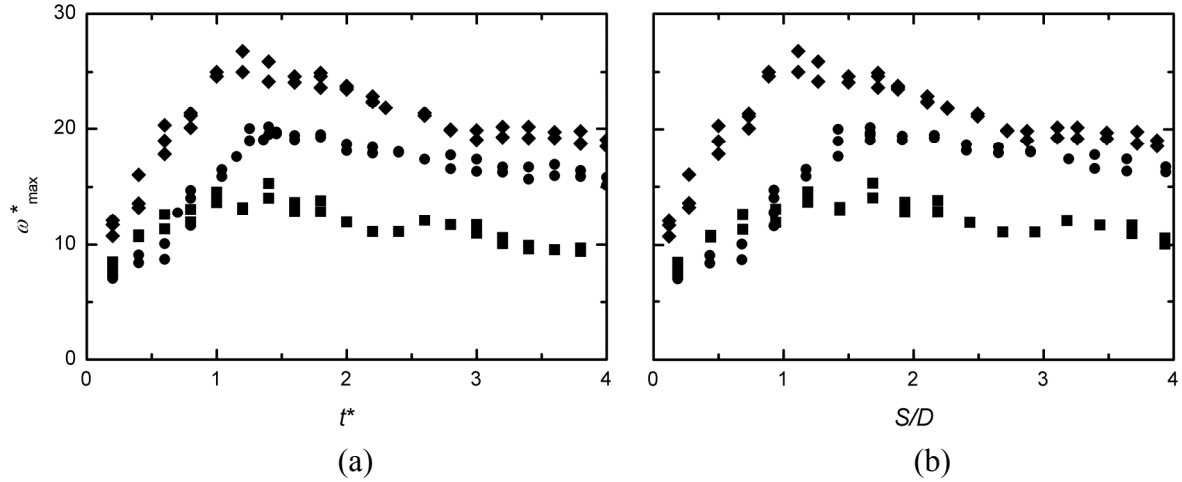

(a) (b)

Figure 6.15: The maximum vorticity within the primary vortices for an impulsively started diamond cylinder (a) with time and (b) with the distance moved, ■, Re = 200, $a^* = 10$; ●, Re = 500, $a^* = 10$; ◆, Re = 1000, $a^* = 5$.

The absolute maximum vorticity within the primary vortices increases with the increase in Re (Figure 6.15(a)). The profiles for various Re are similar in shape; they all undergo a rapid increase, before settling down at some constant value. The peak for Re = 1000 is about 25, while that of Re = 500 is about 20 and that of Re = 200 is just about 15. The graphs remain distinct with the same profile when plotted against the distance moved by

the cylinder (Figure 6.15(b)). This is an indication the maximum vorticity is dependent on Re.

6.8 Velocities along the Wake Centerline

Figure 6.16 shows the velocity variation along the wake centerline of an impulsively started diamond cylinder at Re = 500. The velocity profiles for $a^* \geq 3$ merge to form a single curve and take up higher negative values than for $a^* < 3$. The negative velocities show the presence of the flow reversal, which is caused by the pressure imbalance between the wake and its surroundings (Bouard and Coutanceau, 1980). The point at which the curves cross the horizontal axis is the stagnation point and marks the end of the recirculation zone.

The velocity profiles change with time although they maintain the same trend (Figure 6.17). Immediately after the start of motion, the velocity profiles are almost entirely positive (meaning the flow is in the streamwise direction). This is an indication that the recirculation zone is not fully developed and not clearly defined. However, as time advances, the flow velocities even at distances closer to the back of the cylinder are in the negative direction and can be much higher than the freestream velocity; for example, at $t^* = 3$, the velocity is almost twice the freestream velocity.

A look at the effect of the Re on the wake centerline velocity reveals that an increase in the Re leads to decrease in the velocity at the wake centerline (Figure 6.18). At any given point in time, the velocity at the wake centerline for Re = 1000 is lower than that of both Re = 200 and 500. The profiles, however, follow a similar trend and seem to converge at some point, downstream, where the velocity is equivalent to the freestream, ($u/U = 1$). Figure 6.19 shows how the velocity profile along the wake centerline develops for Re = 200 and 1000. It

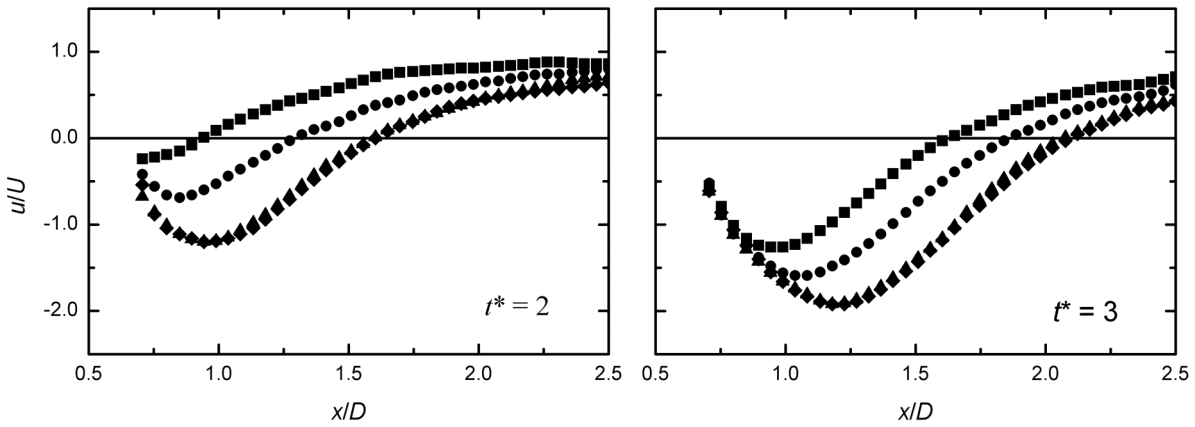

Figure 6.16: The velocity, u/U, along the wake centerline for an impulsively started diamond cylinder at Re = 500. ■, $a^* = 0.5$; ●, $a^* = 1$; ▲, $a^* = 3$; ▼, $a^* = 5$; ◆, $a^* = 10$.

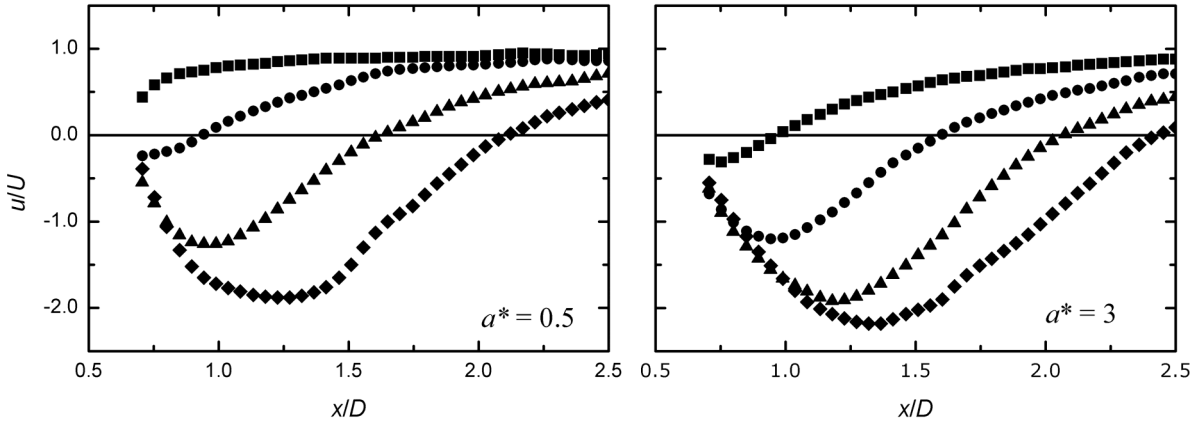

Figure 6.17: The velocity along the wake centerline for an impulsively started diamond cylinder at Re = 500. ■, $t^* = 0.5$; ●, $t^* = 1$; ▲, $t^* = 2$; ▼, $t^* = 3$; ◆, $t^* = 4$.

can be seen that for both cases the velocity continues to become more negative with the elapse of time from the start of the motion.

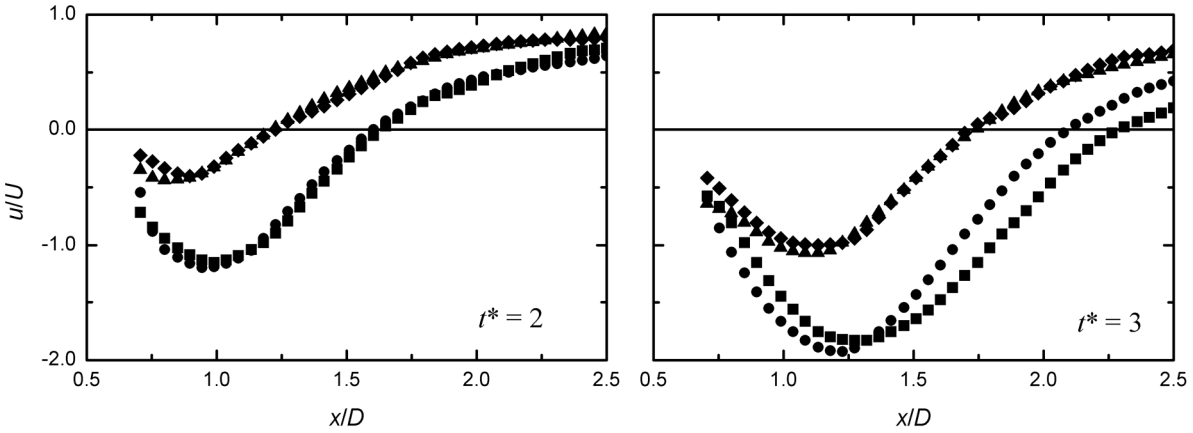

Figure 6.18: The velocity along the wake centerline of an impulsively started diamond cylinder. ■, Re = 200, $a^* = 10$; ●, Re = 500, $a^* = 10$; ▲, Re = 1000, $a^* = 3$; ◆, Re = 1000, $a^* = 5$.

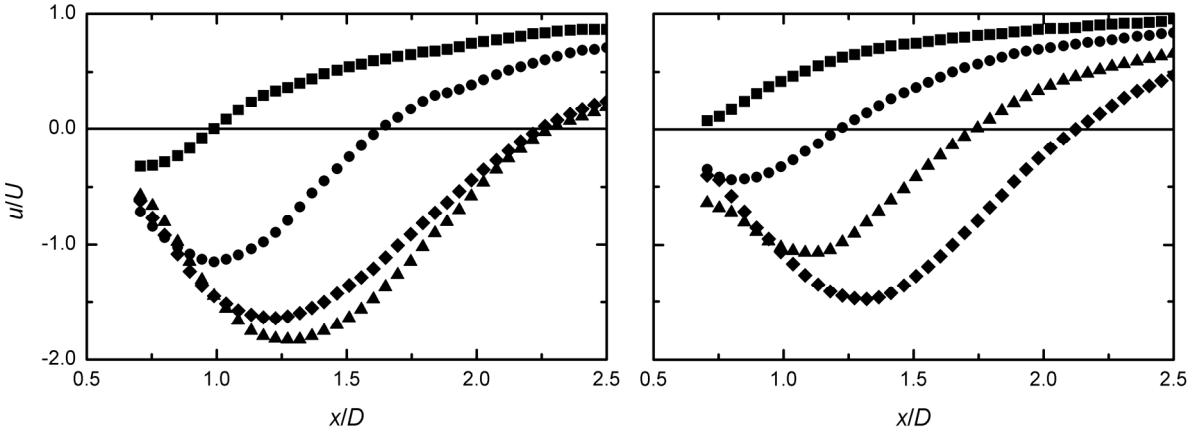

(a) Re = 200, $a^* = 10$ **(b) Re = 1000, $a^* = 3$**

Figure 6.19: The velocity along the wake centerline of an impulsively started diamond cylinder. ■, $t^* = 0.5$; ●, $t^* = 1$; ▲, $t^* = 2$; ▼, $t^* = 3$; ◆, $t^* = 4$.

CHAPTER SEVEN

COMPARISON OF THE RECIRCULATION ZONES

7.1 Introduction

In this chapter a comparison is made between the growth of the recirculation zone of the circular, square and diamond cylinders at various Reynolds numbers. From the discussions in Chapters 4, 5 and 6, it is clear that for all the geometries the recirculation zone grows with time and somewhat varies with Re. The recirculation zone growth can be quantified by looking at the behavior of the recirculation zone length, L_R/D, the location of the primary vortices both in the streamwise and cross-stream directions, a/D and b/D, respectively, as well as the strength of the vortices, Γ^*, and the maximum vorticity, ω^*_{max}, within the zone.

This comparison is categorized into three, based on the Re at which the experiments were done: Re = 200, 500 and 1000. For simplicity, only the highest acceleration parameter at each Reynolds number (which closely approximates a true impulsive motion) is used. In most cases, there is no difference in profiles between the data plotted against the time and those plotted against the distance moved from the start of the impulsive motion. Therefore, except for L_R, only the data plotted as a function of time are shown.

7.2 The Recirculation Zone at Re = 200

A comparison between the growth of the recirculation zone length with time at Re = 200 is shown in Figure 7.1(a). At any given point in time, the L_R for a diamond cylinder is higher than the L_R for both the square and circular cylinder. The measurements of L_R are made from the center of the cylinder which is why the lowest value for the diamond cylinder is 0.71 (the length from the center of the cylinder to the edge) while that of the square and circular cylinders is 0.5. In the plot of the data against the distance moved from the start of impulsive motion, Figure 7.1(b), it can be seen all the curves increase linearly with time but that of the diamond cylinder increases at a faster rate.

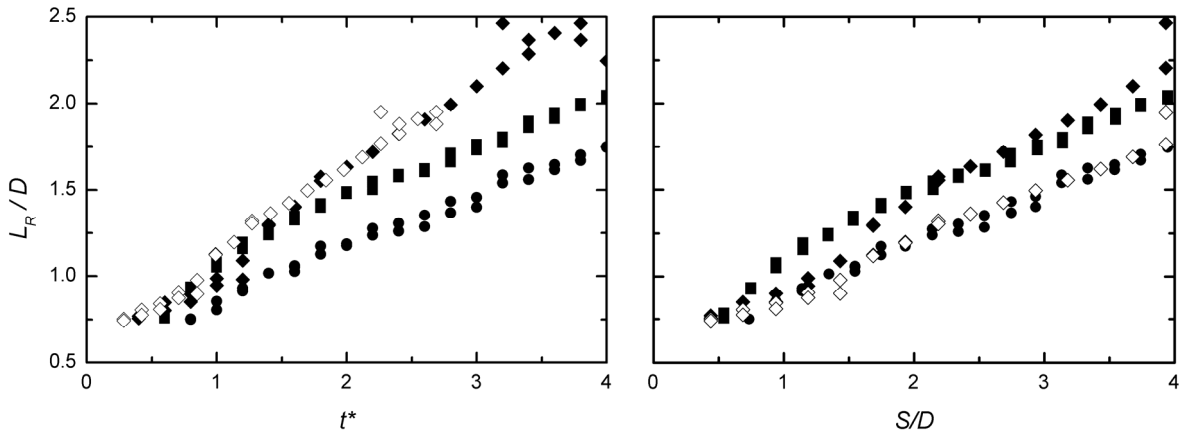

(a) (b)

Figure 7.1: The recirculation zone of three types of cylinder at Re = 200, a^* = 10, plotted as a function (a) time and (b) the distance moved from the start of motion; ●, circular cylinder; ■, square cylinder; ◆, diamond cylinder; ◊, diamond cylinder when non-dimensionalised using the width, W.

In Figure 7.2(a), the streamwise locations of the centers of the primary vortices are compared. The graph shows that the streamwise positions of the vortices, at any time, are almost the same for the square and the circular cylinders. The position of the vortices in the streamwise direction for an impulsively started diamond cylinder increases linearly with time

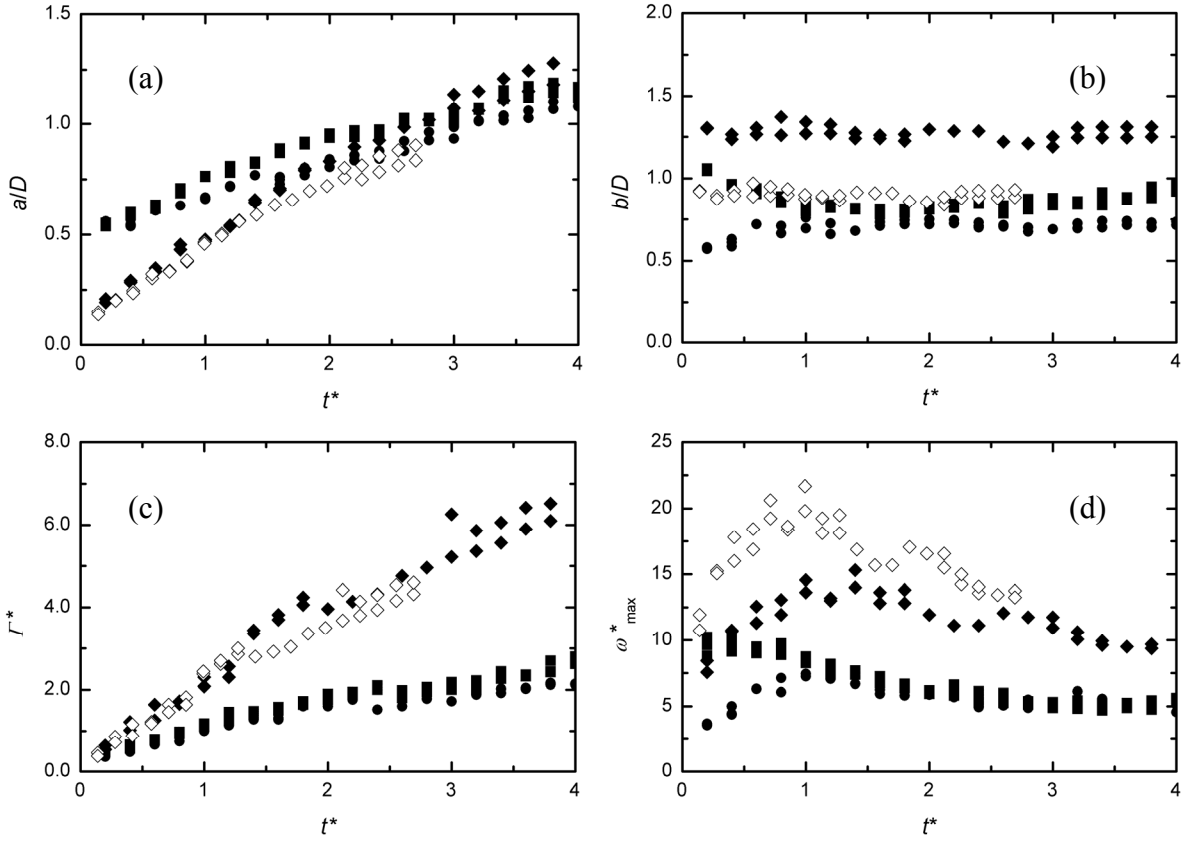

Figure 7.2: Impulsively started cylinders at Re = 200, *a = 10: (a) the streamwise location of the vortices, (b) the cross-stream spacing of the vortices, (c) the circulation and (d) the maximum vorticity; symbols as in Figure 7.1.**

for the entire test duration. Since the vortices are formed at the outer edges of the diamond cylinder, they are closer to the center of the cylinder at the start of the motion. This explains why, at the start of motion, a/D for a diamond cylinder is less than that of the square and circular cylinder. The plot of a/D against the distance moved from the start of the impulsive motion (not shown) takes a very similar profile with no additional unique features.

The cross-stream spacing of the vortices, b/D, Figure 7.2(b), is relatively independent of t^* as was shown in Sections 4.5, 5.5 and 6.5. The vortex spacing for the diamond cylinder, however, is higher than for both the circular and square cylinder. When the separation occurs at the fixed edges of the cylinder (diamond and square cylinder), the cross-stream spacing

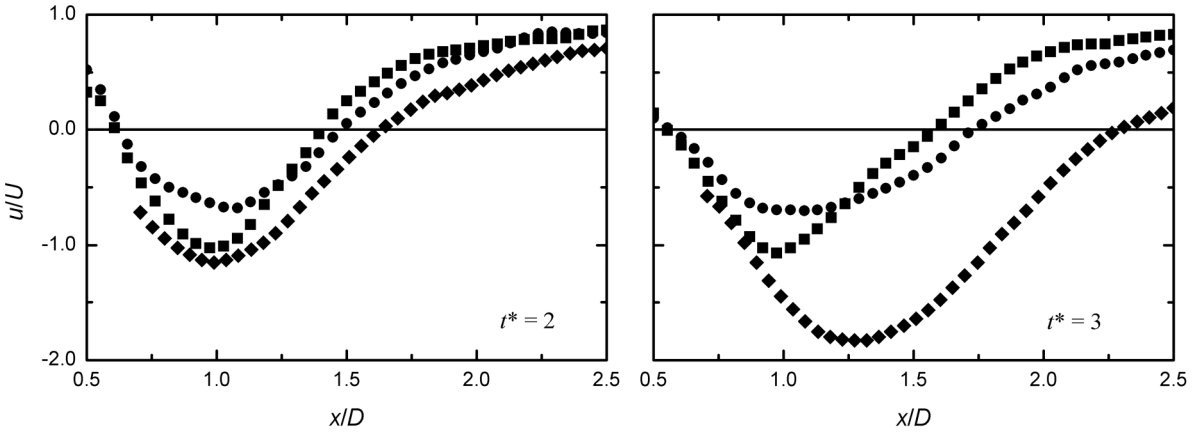

Figure 7.3: The velocity along the wake centerline of impulsively started cylinders at Re = 200, *a = 10. Symbols as in Figure 7.1**

slightly decreases, just after the start of the motion and eventually settles at a value 10% lower than the initial value.

A look at the strength of the primary vortices reveals that the circulation of all impulsively started cylinders increases linearly with time, Figure 7.2(c). The circulations of the square and circular cylinders are similar but are almost three times lower than those of the diamond cylinder. The high velocity of reversal flow in the wake of the diamond cylinder may be a contributing factor to the high circulation.

The maximum vorticity within the vortices of the impulsively started cylinders are comparatively shown in Figure 7.2(d). The maximum vorticity for the diamond cylinder is noticeably higher than those of square and circular cylinders, at any point during the motion. The profiles, however, follow a similar trend characterized by some 'acceleration-like' phase, then a peak and eventually settling at some constant steady value. These profiles are similar to impulsive-start motion profile with an overshoot (Figure 2.1). The extra vorticity forming the overshoot comes from the acceleration of the cylinder (Jeon and Gharib, 2004).

The length of the recirculation zone for the diamond, when plotted against the time, is independent on whether they are non-dimensionalised using one side of the diamond cylinder side, D, or using the width, W (length of the diagonal) provided the time is also non-dimensionalised using D or W respectively. This is seen from the collapse of the two curves onto a common curve, Figure 7.1(a). However, when plotted against the distance moved from the start of the motion, the L_R curve of the diamond cylinder non-dimensionlised using W collapses with the L_R curve of the circular cylinder. A similar observation is seen in a/D, (Figure 7.2(a)), b/D (Figure 7.2(b)) and circulation, (Figure 7.2(c)). The maximum vorticity, non-dimensionalised using W, (Figure 7.2(d)), is higher than those non-dimensionalised using D by a factor of $\sqrt{2}$.

The velocities along the wake centerline for the cylinders are compared in Figure 7.3. It can be seen that the velocities along the centerline of the diamond cylinder are much higher than those of the square and circular cylinder. It also has the highest negative value which may be attributed to the presence of high reversal flow. The circular cylinder has the lowest negative velocity.

7.3 The Recirculation Zone for Re = 500

The evolution of the recirculation zone length for impulsively started cylinders with time at Re = 500, Figure 7.4(a), shows that the L_R for the diamond cylinder increases much faster in time than that of the square and circular cylinders. While the L_R of the square and circular cylinders seems to approach some asymptotic value at $t^* = 3.5$, the L_R of the diamond cylinder does not, but instead increases steadily for the entire test duration. A similar behavior of the profiles is seen when the data are plotted against the distance moved from the start of the impulsive motion, Figure 7.4(b).

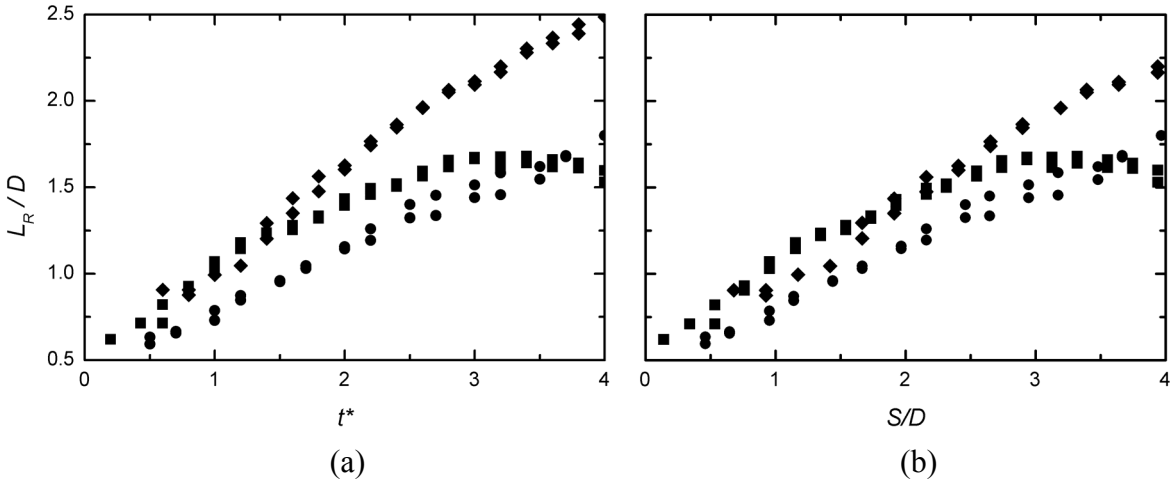

(a) (b)

Figure 7.4: The length of the recirculation zone, for the impulsively started cylinders at Re = 500, a^* = 10; Plotted (a) against time and (b) against the distanced moved from the start of motion. Symbols as Figure 7.1

The increase in the length of the recirculation zone is accompanied by the increase of the streamwise location of the primary vortices, Figure 7.5(a). The position of the primary vortices for the diamond cylinder increases steadily over the entire duration just like the L_R, while the streamwise location of the vortices seems to settle to an asymptotic value for the square and the circular cylinder at just about the same time as was seen in the L_R data. The corresponding cross-stream spacing of the primary vortices, Figure 7.5(b), shows that the cross-stream spacing of the primary vortices for the diamond cylinder is higher than that of the circular and square cylinders. At the start of the motion, the cross-stream spacing in the diamond and square cylinders is about the length between the points of separation (1 for square and $\sqrt{2}$ for the diamond cylinder), but as time advances the size of the vortex spacing drops slightly and settles at a steady value of about 10% less (like it did for Re = 200).

From the behavior of the L_R and a/D results, it seems the vortices at the back of the diamond cylinder are more stable and firmly attached to the cylinder and that is possibly why the data increase linearly with time for a longer duration. The reason for this stability may be

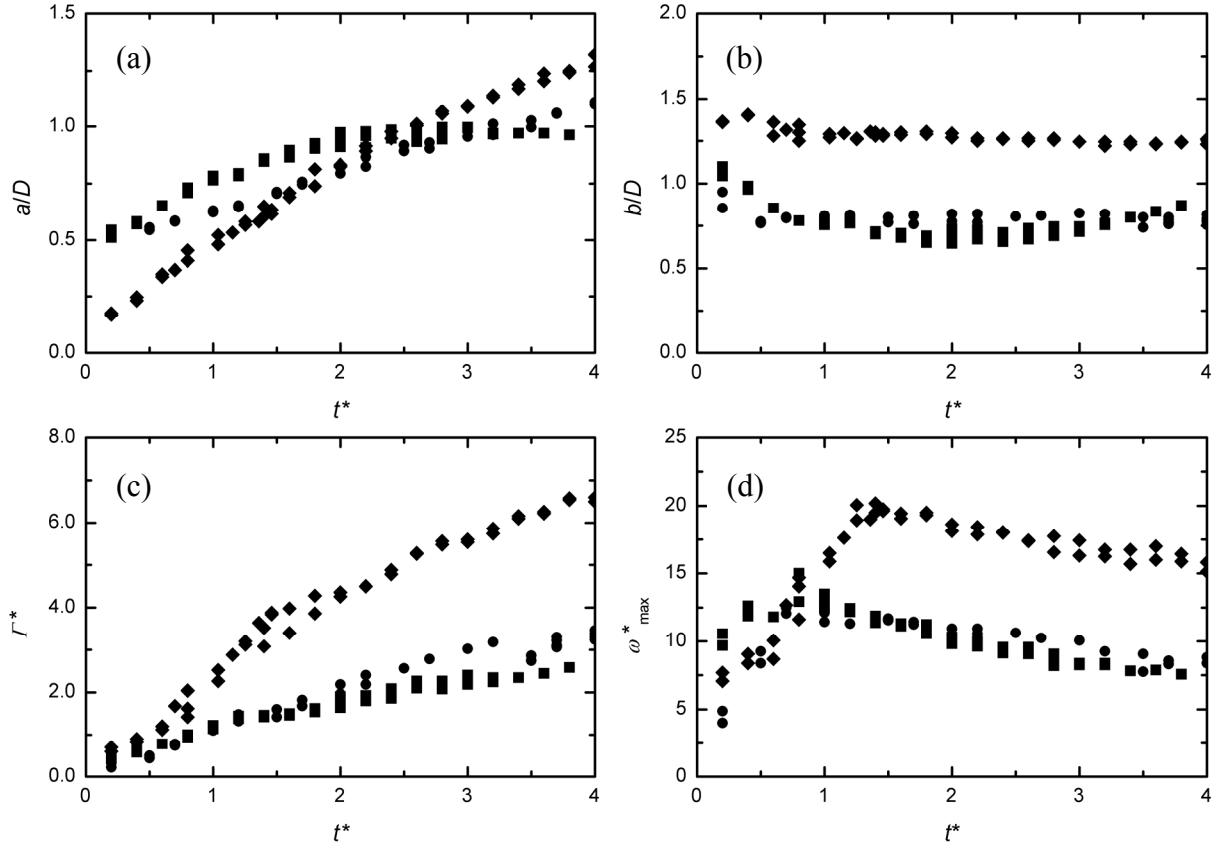

Figure 7.5: The growth of the recirculation zone features for impulsively started cylinders at Re = 500, $a^* = 10$: (a) the streamwise location of the primary vortices; (b) the corresponding cross-stream spacing; (c) the circulation of the primary vortex; (d) the maximum vorticity within the primary vortex. Symbols as in Figure 7.1.

due to the overall surface area of the cylinder where the vortices get attached. It can be noticed that the surface area per unit length for the diamond cylinder is twice as much as that of the square cylinder. From the steady values of b/D, the separation angle at surface of the circular cylinder may be determined to be equivalent to about 78^0, which gives a surface area of 1.366 per unit length. Therefore, the bigger the surface area, the longer is the L_R and a/D.

A comparison of the strength of the primary vortices, Figure 7.5(c), shows that the strength of the primary vortex behind a diamond cylinder is also higher than those behind the square and the circular cylinders. The circulation for all types of cylinders increases linearly

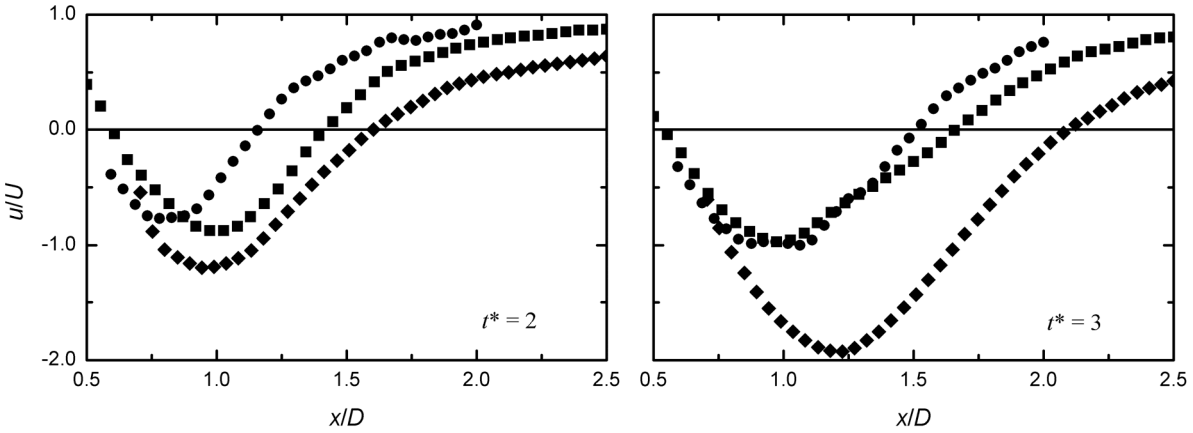

Figure 7.6: The velocities along the wake centerline of impulsively started cylinders at Re = 500, *a = 10. Symbols as in Figure 7.1.**

with time at different rates. This can also be attributed to the stability of the vortices, in addition to the high velocity of the reversal flow.

Figure 7.5(d) shows the maximum vorticity within the recirculation zone of impulsively started cylinder. Although the profiles are similar, the circular and the square cylinders reach their peak earlier than the diamond cylinder and begin to level off. The diamond cylinder on the other hand continues to rise, but once the peak has been reached, it also begins to level off. At the steady state condition (when the cylinder's acceleration phase has ended), the maximum vorticity of the square and circular cylinder are the same while that of the diamond cylinder is about twice as much.

The velocity along the wake centerline for the impulsively started cylinder is shown in Figure 7.6. The graphs show that there is high velocity associated with the diamond cylinder for all the *t**. High negative velocities means high reversal flows.

7.4 The Recirculation Zone at Re = 1000

The length of the recirculation zone for the impulsively started cylinders at Re = 1000, as a function of time, is shown in Figure 7.7(a). Comparing the increases for the

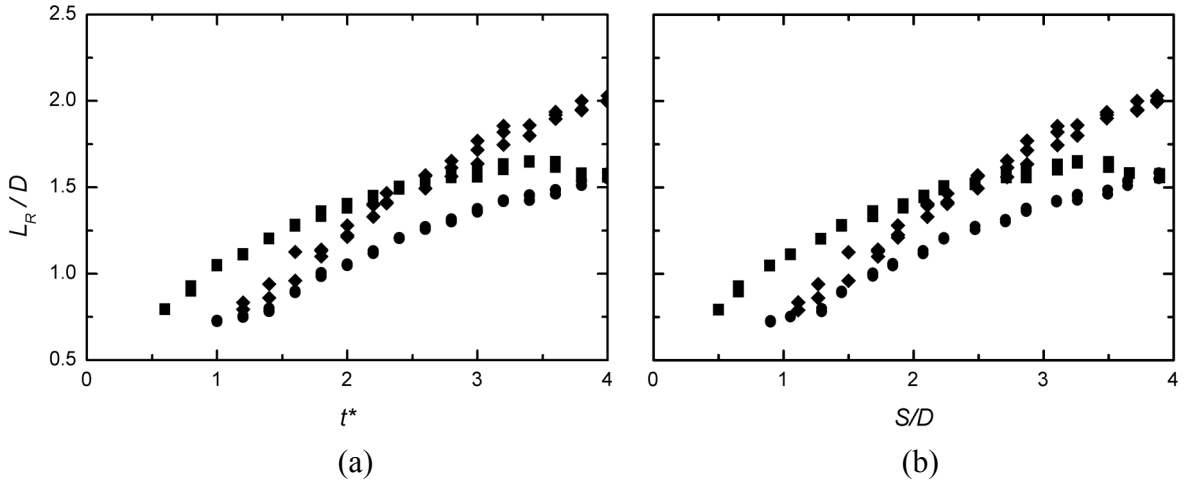

(a) (b)

Figure 7.7: The length of the recirculation zone, for the impulsively started cylinders at Re = 1000, $a^* = 5$, plotted (a) against time and (b) against the distanced moved from the start of motion. Symbols as Figure 7.1.

various cylinders, it can be seen that the diamond cylinder data increases at a faster rate. The square cylinder results are initially higher than both the diamond and circular cylinder but they do reach their steady value much earlier and begin to level off. Generally, the curve for the circular cylinder is relatively lower. The presentation of the results against the distance moved from the start of the impulsive motion, Figure 7.7(b), portrays a profile which is similar in shape to Figure 7.7(a).

The locations of the primary vortices in the streamwise direction are compared in Figure 7.8(a). It can be seen that the streamwise location of the primary vortices increases steadily for the diamond cylinder for the entire test duration. The square cylinder results, however, increase up to $t^* \approx 2.5$ and then begins to take some constant value. This asymptotic nature of the square cylinder graphs is similar to the one in L_R. The corresponding cross-stream spacing of the vortices is shown in Figure 7.8(b). Since the circular cylinder has a continuous curvature, the cross-stream spacing is slightly different at higher Re. It undergoes a slight increase from $b/D \approx 0.5$ to settle at $b/D \approx 0.7$ at $t^* = 1.5$ (at which time,

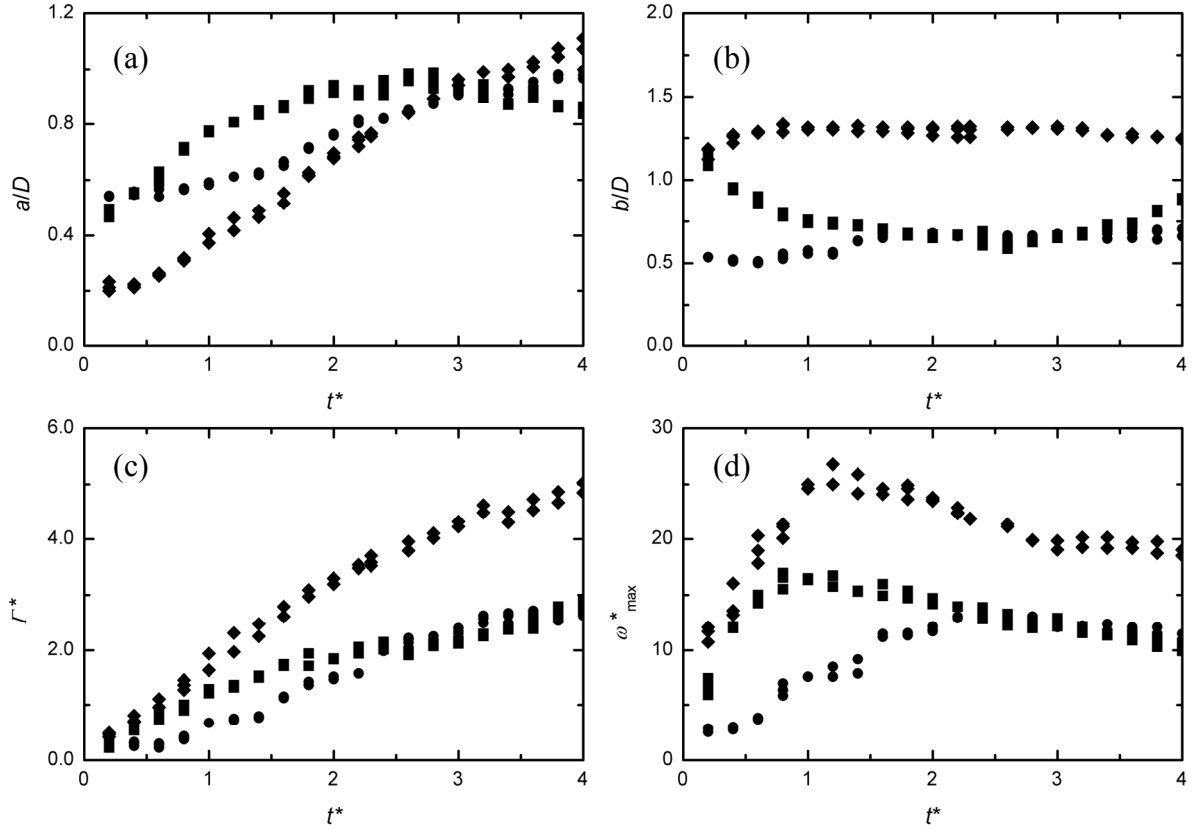

Figure 7.8: The growth of the recirculation zone features for impulsively started cylinders at Re = 1000, $a^* = 5$: (a) the streamwise location of the primary vortices; (b) the corresponding cross-stream spacing; (c) the circulation of the primary vortex; (d) the maximum vorticity within the primary vortex. Symbols as in Figure 7.1.

the cross-stream spacing will be equal to that of the square cylinder). The cross-stream spacing for the diamond cylinder is the highest.

The strengths of the primary vortices formed in the wake at different Re are compared in Figure 7.8(c). The circulation of the primary vortex behind the diamond cylinder is much higher than the circulation of the primary vortices formed behind both the square and diamond cylinder. For all the cylinders, the circulation increases with the time elapsed after the start of motion. There is a notable observation at $t^* = 2.5$, where the circulations of both the square and circular cylinder merge to form one common curve. A similar observation

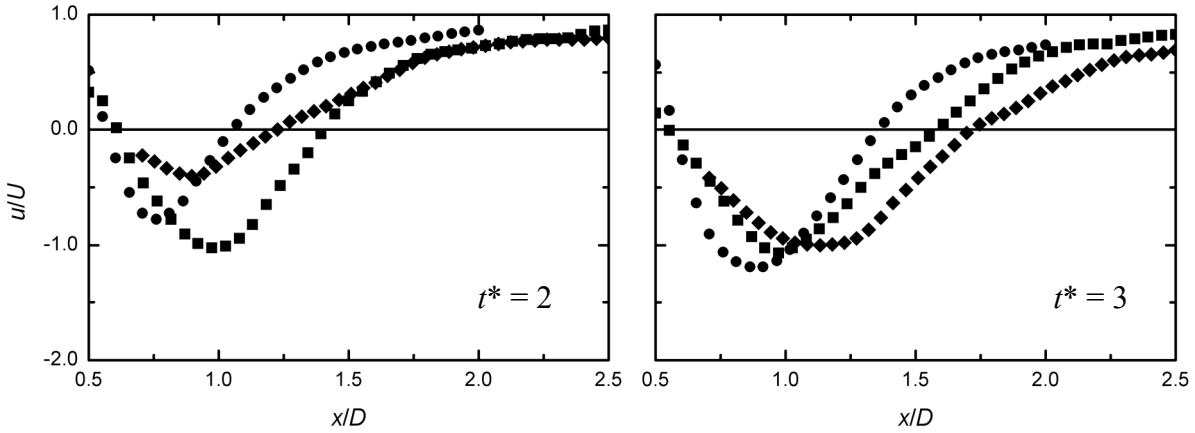

Figure 7.9: The velocities along the wake centerline of impulsively started cylinders at Re = 1000, $a^* = 5$. Symbols as in Figure 7.1.

occurs at the same time for the maximum vorticity (Figure 7.8(d)), and b/D (Figure 7.8(b)) at $t^* = 1.5$.

The velocities along the wake centerline of the impulsively started cylinders are shown in Figure 7.9. It can be seen that the velocity magnitude along the wake centerline for the diamond cylinder is much higher than the velocity along the wake centerline for the circular and square cylinder for $t^* < 3$. For $t^* = 3$, the velocity along the wake centerline for the square and diamond cylinder are almost the same except at $x/D < 0.5$.

CHAPTER EIGHT

CONCLUSIONS AND RECOMMENDATIONS

8.1 Conclusions

An extensive research of impulsively started flow around circular, square and diamond cylinders at Re = 200, 500 and 1000 has been done using the particle image velocimetry (PIV) technique. From the study, a motion can be said to be impulsively started if the acceleration parameter, $a^* \geq 3$. Above this a^*, the acceleration time (time to reach a constant velocity) of motion is very small, the motion corresponds to an almost instantaneous jump from rest to a steady velocity, and the data for various features of the recirculation zones collapse onto common curves.

The length of the recirculation zone, L_R, the streamwise location of the primary vortices, a/D, and the circulation, Γ^*, of the primary vortices, generally increase with time for all the geometries. The rate of increase may, however, be directly dependent on the Reynolds number, the acceleration parameter, and the type of cylinder. For a given Reynolds number, L_R/D, a/D and circulation, for all cylinders examined, increase with an increase in a^*, until $a^* \geq 3$, at which point there will be no more increase regardless of the increase in a^* (since the conditions corresponding to the impulsively started motion have been achieved). It was found that L_R/D, a/D and the circulation of the primary vortices for the impulsively started cylinders decrease with an increase in Re.

The length of recirculation zone, streamwise location and the circulation of the primary eddies in an impulsively started diamond-shaped cylinder are higher than for both the square and the circular cylinder for all the Re examined in this research. While the L_R/D, a/D and the circulation seem to approach some constant value for the circular and square cylinder, they increase linearly with time during the entire test duration (up to $t^* = 4$) for the diamond cylinder.

The cross-stream spacing of the primary vortices, on the other hand, is relatively independent of t^*, a^* and Re. The cross-stream spacing of the primary vortices is mainly determined by the location of the separation points on the surface of the cylinder; therefore, the values are varied for the different types of cylinders. The spacing for the circular cylinder is the lowest ($b/D \approx 0.7$) while that of the diamond cylinder is the highest ($b/D \approx 1.414$).

The maximum vorticity inside the primary vortices increases in time for all the Re examined and for different types of cylinders. The increase is influenced by the a^* but follows a profile characterized by some steady increase, then a peak and eventually settling at some constant value. The peak of the maximum vorticity profiles curves is attained shortly after the end of the acceleration phase of motion.

The growth of the recirculation zone is more dependent on the distance moved than the magnitude of initial acceleration. This is shown by the collapse of the recirculation zone features when plotted against the distance moved by the cylinder following the start of motion. This observation is common to all types of cylinders examined.

8.2 Recommendations

Although most of the research in the recent past has been focused on the impulsively started flow over circular cylinder, there has been little research work done for the

impulsively started flow over square and diamond cylinders. It is recommended that the experimental results obtained in this research should form a basis for further studies in this subject.

The time evolution of the forces accompanying the growth of the recirculation zone has not been examined in this research, yet there are some interesting profiles of the forces (e.g. pressure forces, drag forces) behind an impulsively started square cylinder and indeed other rectangular prisms, as was shown using numerical analysis by Lee (1998) and Lee *et al*. (1996). Therefore, an experimental study of how these forces develop is needed in order to validate the numerical data.

REFERENCES

Anagnostopoulos, E., Gerrard, J.H., 1976, A towing tank with minimal background motion, *Journal of Physics E: Scientific Instruments*, **9**, 951-954.

Bouard, R., Coutanceau, M., 1980, The early stage development of the wake behind an impulsively started cylinder for $40 < Re < 10^4$, *Journal of Fluid Mechanics*, **101**, 583-607.

Chang, C.-C., Chern, R.-L., 1991, A Numerical study of flow around an impulsively started circular cylinder by a deterministic vortex method, *Journal of Fluid Mechanics*, **233**, 243-263

Chu, C.-C., Liao Y.-Y., 1992, A quantitative study of the flow around an impulsively started circular cylinder, *Experiments in Fluids*, **13**, 137-146.

Coutanceau, M., Bouard, R., 1977a, Experimental determination of the main features of the viscous flow in the wake of a circular cylinder in uniform translation. Part 1. Steady flow. *Journal of Fluid Mechanics*, **79**, 231-256.

Coutanceau, M., Bouard, R. 1977b, Experimental determination of the main features of the viscous flow in the wake of a cicular cylinder in uniform translation. Part 2. Unsteady flow. *Journal of Fluid Mechanics*, **79**, 257- 272.

Coutanceau, M., Defaye, J., 1991, Circular cylinder wake configurations: A flow visualization survey, *Applied Mechanics Reviews*, **44**, 255-305.

Dupuis, A., Chatelain, P., Koumoutsakos, 2008, An immersed boundary-lattice-Boltzmann method for the simulation of the flow past an impulsively started cylinder, *Journal of Computational Physics*, **227**, 4486-4498.

Finaish, F., 1991, On vortex structures and processes over bluff bodies in impulsively flow, *Experiments in Fluids*, **11**, 262-267.

Gad-el-Hak, M., 1987, The water towing as an experimental facility, *Experiments in Fluids*, **5**, 289-297.

Honji, H., Taneda, S., 1969, Unsteady flow past a circular cylinder, *Journal of the Physical Society of Japan*, **27**, 1668-1677.

Huang, R.F., Yen, S.C., Huang, C.Y., Wu, J.Y., 1999, PIV Measurements on an impulsively started wing, *Journal of Flow Visualization & Image Processing*, **6**, 1-17.

Izumi, K., Kuwahara, K., 1983, Unsteady flow field, lift and drag measurements of impulsively satarted elliptic cylinder and circular-arc airfoil, AIAA 16th Fluid and Plasma Dynamics Conference, Danvers, Massachusetts. pp 1-15.

Jeon, D., Gharib, M., 2004, On the relationship between the Vortex formation process and cylinder wake vortex patterns, *Journal of Fluid Mechanics*, **519**, 161-181.

Koumoutsakos, P., Leonard, A., 1995, High-resolution simulations of the flow around an impulsively started cylinder using vortex methods, *Journal of Fluid Mechanics*, **296**, 1-38.

Lee, T.S., 1998, Early stages of an impulsively started unsteady flow past non-rectangular prisms, *Computers and Fluids*, **27,** 435-453.

Lee, T.S., Tan, R.S., Xu, X.P., 1996, Numerical study of the early stages of impulsively started unsteady laminar flow past a square cylinder, *International Journal of Numerical Methods for Heat and Fluid Flow*, **6**, 53-70.

Li, Y., Shock, R., Zhang, R., Chen, H., 2004 Numerical study of flow past an impulsively started cylinder by lattice-Boltzmann method, *Journal of Fluid Mechanics*, **519**, 273-300.

Lian, Q.-X., Huang, Z, 1989, Starting flow and structures of the starting vortex behind bluff bodies with sharp edges, *Experiments in Fluids,* **8**, 95-103.

Lin, J.C., Towfighi, J., Rockwell, D., 1995, Instantaneous structure of the near wake of a circular cylinder: on the effects of Reynolds number, *Journal of Fluids and Structures*, **9**, 409-418.

Markus, R., Christian, E. W., Steve, T. W., Jürgen, K., 2007, *Particle Image Velocimetr*y, A Practical Guide, Second Edition, Springer, New York.

Nagata, H., Funada, H., Kawai, K., Matsui, T., 1985a, Unsteady flows in the vortex region behind a circular cylinder started impulsively (1st report, feeding mechanism of vorticity and onset of turbulence), *Bulletin of the JSME*, **28** (245), 2599-2607.

Nagata, H., Funada, H., & Matsui, T., 1985b, Unsteady flows in the vortex region behind a circular cylinder started impulsively (2nd report, velocity fields and circulations). *Bulletin of the JSME*, **28**(245), 2608-2616.

Nagata, H., Kakehi, Y., Tsunekawa, M., Hasegawa, T., 1975, Unsteady flow past a circular cylinder started impulsively, *Bulletin of the JSME*, **18** (123), 992-1001.

Nagata, H., Minami, K., Murata, Y., 1979, Initial flow past an impulsively started circular cylinder, *Bulletin of the JSME*, **22** (166), 512-520.

Nagata, H., Nagase, I., Ito, K., 1989, Unsteady flows past a circular cylinder started impulsively in the Reynolds number range 500 < Re < 10,000. *JSME International Journal Series II*, **32**(4), 540-549.

Nair, M.T., Sengupta, T.K., 1996, Onset of asymmetry: Flow past circular and elliptic cylinders, *International Journal for Numerical Methods in Fluids,* **23,** 1327-1345.

Sanyasiraju, Y.V.S.S., Manjula, V., 2005, Flow past an impulsively started circular cylinder using a higher-order semicompact scheme, *Physical Review E*, **72**, 016709 (10 pages).

Sarpkaya, T., 1991, Nonimpulsively started flow about a circular cylinder, *AIAA Journal*, **29**, 1283-1289.

Sarpkaya, T., 1992, Brief reviews of some time dependent flows, *ASME Journal of Fluids Engineering*, **114**, 283-298.

Slaouti, A., Gerrard, J.H., 1981, An experimental investigation of the end effects on the wake of a circular cylinder towed through water at low Reynolds number, *Journal of Fluid Mechanics*, **112**, 297-314.

Smith, P.A., Stansby, P.K., 1988, Impulsively started flow around a circular cylinder by vortex method, *Journal of Fluid Mechanics*, **194**, 1-38.

Sumer, B.M., Fredsoe, J., 2006, *Hydrodynamics around cylindrical structures*, (Revised ed.) World Publishing Co. Pte. Ltd., Singapore

Sumner, D. Barth, J.E., Dansereau, O.J.P., Heseltine, J.L., Crane, M.G., 2005, X-Y towing tank for unsteady fluid mechanics experiments, Proceedings of the 20th Canadian Congress of Applied Mechanics (CANCAM 2005), Montreal, Canada, pp. 353-354.

Sumner, D., Price, S.J., Paidoussis, M.P., 1999, Tandem cylinders in impulsively started flow, *Journal of Fluids and Structures*, **13**, 955-965.

Ta Phuoc Loc, 1980, Numerical analysis of unsteady secondary vortices generated by an impulsively started circular cylinder. *Journal of Fluid Mechanics*, **100**, 111.

Ta Phuoc Loc, Bouard, R., 1985, Numerical solution of early stage of the unsteady viscous flow around a circular cylinder: A comparison with experimental visualization and measurements, *Journal of Fluid Mechanics*, **160**, 93-117.

Taneda, S., 1977, Visual study of unsteady separated flows around bodies, *Progress in Aerospace Sciences*, **17**, 287-348.

TSI, 2008, Insight 3G Data Acquisition, Analysis and Display Software Platform, Users Guide.

White, F.M., 1999, *Fluid Mechanics*, 4th Edition, McGraw-Hill, New York.

Williamson, C.H.K, 1996, Vortex dynamics in the cylinder wake, *Annual Review of Fluid Mechanics*, **28,** 477-539.

Wu, C.L., Chu, C.C., 1989, The flow around an impulsively started circular cylinder: a preliminary study. Proceedings of 13th Annual Conference on Mechanics, Taiwan, R.O.C., 727-735.

Zdravkovich, M.M., 1997, *Flow Around Circular Cylinders*, Vol. 1: Fundamentals, Oxford University Press, New York.